

Thermophysical modeling of main-belt asteroids from WISE thermal data

J. Hanuš^{a,*}, M. Delbo^{'b}, J. Ďurech^a, V. Alí-Lagoa^c

^a*Astronomical Institute, Faculty of Mathematics and Physics, Charles University, V Holešovičkách 2, 18000 Prague, Czech Republic*

^b*Université Côte d'Azur, CNRS-Lagrange, Observatoire de la Côte d'Azur, CS 34229 – F 06304 NICE Cedex 4, France*

^c*Max-Planck-Institut für extraterrestrische Physik, Giessenbachstraße, Postfach 1312, 85741 Garching, Germany*

Abstract

By means of a varied-shape thermophysical model of Hanuš et al. (2015, *Icarus*, Volume 256) that takes into account asteroid shape and pole uncertainties, we analyze the thermal infrared data acquired by the NASA's Wide-field Infrared Survey Explorer of about 300 asteroids with derived convex shape models. We utilize publicly available convex shape models and rotation states as input for the thermophysical modeling. For more than one hundred asteroids, the thermophysical modeling gives us an acceptable fit to the thermal infrared data allowing us to report their thermophysical properties such as size, thermal inertia, surface roughness or visible geometric albedo. This work more than doubles the number of asteroids with determined thermophysical properties, especially the thermal inertia. In the remaining cases, the shape model and pole orientation uncertainties, specific rotation or thermophysical properties, poor thermal infrared data or their coverage prevent the determination of reliable thermophysical properties. Finally, we present the main results of the statistical study of derived thermophysical parameters within the whole population of main-belt asteroids and within few asteroid families. Our sizes based on TPM are, in average, consistent with the radiometric sizes reported by Mainzer et al. (2016, *NASA PDS*, Volume 247). The thermal inertia increases with decreasing size, but a large range of thermal inertia values is observed within the similar size ranges between $D \sim 10\text{--}100$ km. We derived unexpectedly low thermal inertias ($< 20 \text{ J m}^{-2} \text{ s}^{-1/2} \text{ K}^{-1}$) for several asteroids with sizes $10 < D < 50$ km, indicating a very fine and mature regolith on these small bodies. The thermal inertia values seem to be consistent within several collisional families, however, the statistical sample is in all cases rather small. The fast rotators with rotation period $P \lesssim 4$ hours tend to have slightly larger thermal inertia values, so probably do not have a fine regolith on the surface. This could be explained, for example, by the loss of the fine regolith due to the centrifugal force, or by the ineffectiveness of the regolith production (e.g., by the thermal cracking mechanism of Delbo' et al. 2014, *Nature*, Issue 508).

Keywords: Asteroids, Asteroids, surfaces, Infrared observations, Photometry, Numeric

1. Introduction

The recent availability of thermal infrared data obtained by the NASA's Wide-field Infrared Survey Explorer (WISE, Wright et al. 2010) opens exciting possibilities of determining surface characteristics of thousands of minor bodies of our solar system (Mainzer et al. 2011a). This characterisation can be performed by the analysis of WISE data by thermophysical models (hereafter TPM, see Sect. 3). WISE observations changed asteroid thermophysical modeling from being limited by the availability and accuracy of thermal infrared data to being limited by the availability of the a priori information required by the TPMs, namely the spin and shape solutions (Koren et al. 2015). This is why early TPM analyses of WISE data focused on a small number of objects: of near-Earth asteroids (NEAs) (341843) 2008 EV5 (Alí-Lagoa et al. 2014) and (29075) 1950 DA (Rozitis et al. 2014), and four main-belt asteroids (MBAs), four NEAs and 1 Trojan (Hanus' et al. 2015).

The main object characteristics that one aims to determine are thermal inertia Γ , Bond albedo A (or geometric visible albedo p_V), surface roughness $\bar{\theta}$ and volume-equivalent diameter (i.e., the diameter of a sphere with the same volume as of the asteroid shape model). The shape can be elongated and in general quite different compared to a sphere. Surface roughness at a scale bigger than the typical diurnal heat propagation distance (few mm to few cm) causes a surface to emit thermal radiation in a non Lambertian way (Lagerros 1998; Rozitis and Green 2011; Delbo' et al. 2015). In particular, the absorbed solar flux is preferentially radiated back to the sun, a phenomenon that is called thermal infrared beaming. Thermal inertia is defined as a function of the density of the surface regolith ρ , thermal conductivity κ , and heat capacity C : $\Gamma = (\rho\kappa C)^{1/2}$, and measures the resistance of a material to temperature change, and thus controls the temperature distribution of the surface of an atmosphereless body. Non-zero thermal inertia breaks the symmetry of the temperature distribution on asteroids. So, Γ directly controls the strength of the Yarkovsky effect, which is the rate of change in the semi-major axis of the orbit of an asteroid (da/dt) due to the recoil force of the thermal photons (see, e.g., Bottke et al.

*Corresponding author. Tel: +420 221912572. Fax: +420 221912577.
Email address: hanus.home@gmail.com (J. Hanuš)

2006; Vokrouhlický et al. 2015).

In the case of asteroids, values between almost zero or below 10 to almost 1000 $\text{J m}^{-2} \text{s}^{-1/2} \text{K}^{-1}$ have been derived (see Table A.2). The lowest values are typical for very large asteroids ($D > 100$ km, Mueller 2012), large Trojans (Mueller et al. 2010; Horner et al. 2012) and large trans-Neptunian objects (TNOs) (Lellouch et al. 2013). These low thermal inertia values have been interpreted as due to very fine and mature regolith or even fluffy surfaces with extremely high porosities (e.g., Vernazza et al. 2012; Lellouch et al. 2013). Most $D > 100$ –200 km MBAs have a thermal inertia of the order of few tens of $\text{J m}^{-2} \text{s}^{-1/2} \text{K}^{-1}$. On the other hand, much smaller NEAs (sizes from several hundred meters to few kilometers) have thermal inertia values of the order of several hundreds (Delbo’ et al. 2015). However, there are almost no thermal inertia determinations for MBAs in a size range of 10–100 km. Our current study fills this gap.

The findings concerning different thermal inertia values between small and large asteroids were later confirmed by the work of Gundlach and Blum (2013): in particular, asteroids with sizes smaller than 100 km in diameter were found to be covered by relatively coarse regolith grains with typical particle sizes in the millimeter to centimeter regime, whereas large asteroids (with diameters bigger than 100 km) possess very fine regolith with grain sizes between 10 and 100 microns. Modeling by Rozitis et al. (2014) suggested a lunar-like thermal inertia characteristic of fine surface regolith on a 1-km NEA. Presence of cohesion forces could prevent the escape of the fine particles driven by the solar wind pressure and the centrifugal force from the surface. So, thermal inertia correlates with the regolith grain size (Gundlach and Blum 2013). Particularly, objects covered with a very fine regolith (for instance, grain sizes between 10 and 100 microns on asteroids larger than 100 km) have typical values of thermal inertia of the order of $10 \text{ J m}^{-2} \text{s}^{-1/2} \text{K}^{-1}$ (see the compilation in Table A.2 for several examples). On the other hand, coarse regolith grains with typical particle sizes of millimeters to centimeters implies thermal inertia values of several hundred $\text{J m}^{-2} \text{s}^{-1/2} \text{K}^{-1}$ (typical for NEAs).

The database of the WISE thermal infrared asteroid observations, with their unprecedented photometric accuracy (often better than 1%) not achievable by current ground-based telescopes and with no contamination by the Earth’s atmosphere, can be analyzed by means of a TPM in order to derive thermal inertias for several hundreds of asteroids with known shape models. Typically, shape models are based on radar imaging or on inversion of photometric lightcurves. The lightcurve-based shape models are stored in the public Database of Asteroid Models from Inversion Techniques (DAMIT¹, Ďurech et al. 2010).

Classically, a TPM is used with an a priori knowledge of the shape and the rotational state of the asteroid. However, the high precision of WISE data introduces a new challenge: as it was already noticed, the shape model plays a crucial role in the derivation of the asteroid physical parameters (Alí-Lagoa et al. 2014; Emery et al. 2014; Rozitis and Green 2014). This mo-

tivated our recent study (Hanuš et al. 2015), where we introduced a *varied shape* TPM scheme (VS-TPM) that takes into account asteroid shape and pole uncertainties, and where we demonstrated its reliability on nine asteroids. Here we apply the VS-TPM method to all main-belt asteroids with lightcurve-based shape models and sufficient amount of thermal infrared data in WISE filters W3 and W4 (see Sect. 2.1).

We describe the thermal infrared fluxes obtained by the WISE satellite in Sect. 2.1 and the shape models and the optical lightcurves used for their determination in Sect. 2.2. The VS-TPM is described in Sect. 3 and applied to three hundred asteroids in Sect. 4. In Sect. 5, we present the main findings of the statistical study of thermophysical parameters within the whole population of MBAs and within few asteroid families. We conclude our work in Sect. 6.

2. Data

2.1. Thermal infrared fluxes

We make use of the data acquired by the WISE satellite (Wright et al. 2010), in particular the results of the NEO-WISE project dedicated to the solar system bodies (see, e.g., Mainzer et al. 2011a). The thermal infrared data were downloaded from the WISE All-Sky Single Exposure L1b Working Database via the IRSA/IPAC archive² and processed in the same way as data used in our previous studies focused on asteroid (341843) 2008 EV₅ (Alí-Lagoa et al. 2014) and nine asteroids (Hanuš et al. 2015). Bellow, we briefly summarize our procedure, additional details can be found in papers mentioned above.

We consider only thermal data from filters W3 and W4 (isophotal wavelengths at 12 and 22 μm) from the fully cryogenic phase of the mission, because these data are thermal-emission dominated, whilst the fluxes in filters W1 and W2 (isophotal wavelength at 3.4 and 4.6 μm) usually at least partially consist of reflected sunlight for typical main-belt objects.

Our selection criteria are based on a combination of criteria from Mainzer et al. (2011b), Masiero et al. (2011), and Grav et al. (2012). We obtained the reported observation tracklets from the Minor Planet Center (MPC) and used them for a cone search radius of 1'' around the MPC ephemeris of the object when querying the IRSA/IPAC catalogs. We only consider data with artifact flags p, P, and 0, quality flags A, B, and C, and data with a magnitude error bars smaller than 0.25 mag. Moreover, we require the IRSA/IPAC modified Julian date to be within four seconds of the time specified by the MPC and that the data are not partially saturated. A positive match from the WISE Source Catalog within 6.5'' around the tracklet indicates that there is an inertial source at a distance smaller than the point-spread function width of the W1 band. We consider that these data are contaminated if the inertial source fluxes are greater than 5% of the asteroid flux and we remove them. We implement the correction to the red and blue calibrator discrepancy in W3 and W4 filters (Cutri et al. 2012).

¹<http://astro.troja.mff.cuni.cz/projects/asteroids3D>

²<http://irsa.ipac.caltech.edu/Missions/wise.html>

We selected only datasets where we had at least 5 points in both W3 and W4 filters. Similarly as in Hanuš et al. (2015), we increased the nominal error bars of the fluxes by factors 1.4 and 1.3 for the W3 and W4 data, respectively. To be more specific, we studied the consistency of the error bars within two WISE measurements of the same source in frames obtained 11 seconds apart from each other. Such double measurements were allowed due to a 10% field overlap between two subsequent frames. Because 11 seconds is not enough time for rotation to explain the differences in the observed fluxes, the uncertainties are clearly underestimated and thus we should consider them. To account for that, we decided to enlarge the uncertainties the way they roughly followed the normal distribution. Similar results were inferred by Nathan Myhrvold (Myhrvold 2017, and private communication). He analyzed all the double detections, while our subset contained about 400 of such detections.

We also utilized the thermal infrared fluxes obtained by the IRAS satellite (Tedesco et al. 2002) as well. These data in four different filters (I1, I2, I3, I4, isophotal wavelengths 12, 25, 60 and 100 μm) were downloaded from the The Supplemental IRAS Minor Planet Survey (SIMPS, Tedesco et al. 2004). We rejected fluxes in filter I4 due to their generally poor quality. The precision of the IRAS fluxes is usually about 10 times lower than of the WISE fluxes, which essentially means that the TPM fits will be governed by the WISE data.

For each asteroid, we downloaded the photometric data and shape solution from the DAMIT database. In several cases, we also obtained new lightcurve data from the Asteroid Lightcurve Data Exchange Format database (ALCDEF³; Warner et al. 2011). For those asteroids that have new lightcurve data compared to the DAMIT version, we generated revised spin state and shape solutions using the lightcurve inversion (Kaasalainen and Torppa 2001; Kaasalainen et al. 2001). All these represent our "nominal" shape models (~ 300). The references to the shape model publications are reported in Table A.3.

2.2. Shape models and disk-integrated photometry

A shape model is used as an *a priori* information in thermophysical modeling of the infrared fluxes of asteroids described in the previous section. Our sample mostly consists of shape models already published and available in the public DAMIT database (~ 300). All shape models from the DAMIT database were derived by the lightcurve inversion method of Kaasalainen and Torppa (2001) and Kaasalainen et al. (2001) and are usually represented by a convex polyhedron with ~ 1000 triangular facets. Sidereal rotation period, the pole orientation, the shape model as well as used lightcurves are all available in the DAMIT database.

The overall shape model quality, which is dependent on the amount, type and variety of the photometric data used for the model determination, differs within our sample. Only recently, a quality flag QF that reflects each shape model reliability was introduced in Hanuš et al. (2018). Such a measure, available for

each shape model, gives us an idea how well the shape model should represent the true shape of the asteroid (the high-quality shape models have $QF = 3$, while rather coarse shape models have $QF = 1$). Typical uncertainties in the pole orientation are $\sim 5\text{--}30$ degrees (e.g., Hanuš et al. 2011), where the lower values correspond to solutions based on large datasets of dense lightcurves ($QF = 3$), whilst the larger values are typical for solutions mostly based on sparse measurements from astrometric surveys ($QF = 1\text{--}1.5$). Often, the restricted geometry of observations due to asteroid's low inclination of its orbit does not allow us to break the symmetry of the inversion method (Kaasalainen and Lamberg 2006), so two pole solutions with similar ecliptic latitudes β and difference in ecliptic longitude λ of $\sim 180^\circ$ are typically available. This ill-posedness of the inversion methods is often called the pole ambiguity. The shape models within the ambiguous solutions are rather similar although differently oriented with respect to the observer.

All shape models are based on dense-in-time and/or sparse-in-time photometry. Generally, combined datasets are used for the shape modeling. The dense data are typically obtained during one night and well sample the rotation period. On the other hand, the sparse data contain a few hundred individual calibrated measurements during ~ 15 years and are obtained by several astrometric surveys. Sparse data sample various observing geometries, which helps to constrain the pole orientation despite their lower photometric quality.

For 12 asteroids, new photometric dense lightcurves became available since their shape models were published. Such data allowed us to better constrain their shape models, and consequently decrease the uncertainty in the pole orientation. We applied the lightcurve inversion method to the updated photometric datasets and derived shape models by following the same procedures as in Hanuš et al. (2011, 2016b). These revised shape models are then used in the TPM.

Moreover, for five asteroids, we derived their shape models for the first time. We present rotation states of these models and used photometry in Tables A.3 and A.4. We utilize these new models in the TPM as well.

3. Thermophysical modeling (VS-TPM)

In the classical TPM analysis a single shape model and spin solution per asteroid is used as an *a priori* and fixed information and model parameters (D , A , Γ , $\bar{\theta}$) are varied until best fit between the calculated and the observed thermal infrared fluxes is obtained. However, this approach does not take into account the uncertainty of the shape and spin state solution. Here we use the varied-shape TPM (VS-TPM) introduced by Hanuš et al. (2015). The VS-TPM consists of applying the classical TPM approach repeatedly using different (varied, bootstrapped) shape models of the same asteroids in order to map the uncertainty of the shape model and its rotation state on the values of the physical parameters. The varied shape models are generated by the lightcurve inversion method from bootstrapped photometric datasets. This implies that we need to possess the disk-integrated optical data that were used for the

³<http://alcdef.org>

shape model determination. These data were downloaded from the DAMIT database.

The VS-TPM scheme consists of three steps:

1. We bootstrap (Press et al. 1986) the original photometric data (i.e., those downloaded from DAMIT or the updated dataset) in such way that we keep the original number of dense lightcurves in the dataset. We independently bootstrap also the sparse data: we randomly choose individual measurements within each lightcurve until we get a sparse lightcurve with the original number of individual measurements.
2. We apply the lightcurve inversion method to each bootstrapped dataset and spin state solution and derive the shape model. We create 19 bootstrapped/varied shape models for each pole solution. We also add the nominal shape and spin pole solution, totaling to 20 varied shapes (and spin states) per object and per pole solution. Each shape model has its own spin solution that is usually consistent within few degrees within the corresponding varied shapes.
3. For each varied shape model and its rotational state, we perform the TPM analysis scheme the same way as for the nominal shape model (i.e., shape from the DAMIT). We run the VS-TPM for each pole solution individually.

The CPU requirements are rather high: a TPM analysis scheme (the most time-consuming procedure) for one particular bootstrapped/varied shape model runs on a single CPU for about a day. We usually have two pole solutions for each asteroid, which results then in 40 individual TPM runs. We applied VS-TPM to about 300 asteroids. Additional details concerning the VS-TPM can be found in Hanuš et al. (2015).

We use a thermophysical model implementation of Delbo' et al. (2007); Delbo' (2004) that is based on TPM developed by Lagerros (1996, 1997, 1998); Spencer et al. (1989); Spencer (1990); Emery et al. (1998). A TPM allows thermal infrared fluxes to be calculated at different wavelengths and at a number of epochs taking into account the shape of an asteroid, its spatial orientation, and a number of physical parameters such as the size of the body, the albedo A , the macroscopic surface roughness $\bar{\theta}$ (Hapke's mean surface slope), and the thermal inertia Γ . The values of the parameters are determined by minimizing the difference between the observed fluxes f_i and the modeled fluxes $s^2 F_i$, where we consider the scale factor s for the asteroid size, and i corresponds to individual observations. To find the optimal set of parameter values, we minimize the metric

$$\chi^2 = \sum \frac{(s^2 F_i - f_i)^2}{\sigma_i^2}, \quad (1)$$

where σ_i represent the errors of fluxes f_i .

The shape is represented either by a convex polyhedron with triangular facets (all models from the DAMIT database), or by a set of surfaces and normals (the so called Gaussian image). The latter representation is a direct output of the lightcurve inversion method (see Kaasalainen and Torppa 2001) and its use in the TPM allows us to save a significant amount of computational time. According to our tests, both representations produce similar fluxes and could be considered equivalent. The shape model has usually a meaningless value of the initial size, and the parameter s , adjusted in the TPM fit to the data, is a factor that either scales linearly all vectors of the vertices of the polyhedron, or quadratically all the surfaces of the Gaussian image. The representation by the polyhedron gives us the *volume equivalent diameter* D_V , while the representation by the Gaussian image leads to the *surface equivalent diameter* D_S (i.e. the diameter of a sphere with the same surface as the shape model scaled in size). However, we always transform D_S to D_V and present this quantity throughout this work. We use convex shape models so we do not need to take into account topographic shadowing effects and the heating due to the light reflected and emitted by facets on other facets.

The usage of a convex shape model is motivated by the scarcity of available shape models with local surface features (based on radar measurements or spacecraft imaging). The ground-truth shape models and in-situ measurements of several asteroids that have been visited by spacecrafts offer a possible validation of the methods based on Earth-based measurements and convex shape models. For instance, O'Rourke et al. (2012) used a concave shape model of main-belt asteroid (21) Lutetia based on Rosetta fly-by data (Carry et al. 2010) as an input for a TPM and derived consistent (though more constrained) thermophysical properties as Mueller et al. (2006) with a convex shape model of Torppa et al. (2003) as an input. Moreover, Rozitis and Green (2014) showed a good consistency between TPM results obtained for lightcurve- and radar-based shape models of NEA (1620) Geographos. Similar consistency was also confirmed between the TPM results for near-Earth asteroid (101955) Bennu (Müller et al. 2012; Emery et al. 2014). Furthermore, Rozitis et al. (2013) claim that large concavities are not always resulting in large self-heating effects for NEAs, it depends on the observational geometry and the aspects of the body being sampled in the disc-integrated data. Then, for MBAs, because they are colder and hence self-heating effects are much weaker ($\text{flux} \propto T^4$), we do not expect that neglecting this effect should have any measurable systematic impact on the sample of derived thermal inertias. It could, however, affect particular cases but this will have to wait for more ground-truth knowledge of MBAs with significant concavities to make a more quantitative argument. Therefore, we expect that the typical concavities as observed by the few spacecraft missions do not significantly affect the TPM results. We note that the largest asteroids usually lack the low-scale surface features, whilst the presence of concavities and their size increase with decreasing size (with some peculiar exceptions such as some asteroids rotating close to the disruption limit that are rather spherical).

Table 1: Ten different values of surface roughness used in the TPM. The table gives the opening angle γ_c , the crater areal density ρ_c , the Hapke’s mean surface slope $\bar{\theta}$, and our designation.

γ_c	ρ_c	$\bar{\theta}$	Designation
0	0.0	0.0	No roughness
30	0.3	3.9	Low roughness
40	0.7	12.6	Medium roughness
41	0.9	16.5	Medium roughness
50	0.5	12.0	Medium roughness
60	0.9	26.7	High roughness
70	0.7	27.3	High roughness
90	0.5	38.8	High roughness
90	0.7	50.1	Extreme roughness
90	0.9	58.7	Extreme roughness

The effect of roughness on the thermal infrared flux is accounted for by adding a spherical-section crater to each surface element of the shape, in which shadowing of crater facets on other facets and mutual heating are taken into account. The crater with an opening angle γ_c and the crater areal density with respect to the flat part of the surface element ρ_c can be varied from 0 to 90° and from 0 to 1, respectively, to cover different strength of the roughness. We calculate the TPM scheme for a set of ten roughness models, whose parameters are given in Table 1. The correspondence between the Hapke’s mean surface slope $\bar{\theta}$ and the adopted values of γ_c and ρ_c is also given in Table 1. We compute $\bar{\theta}$ following the definition of Hapke (1984):

$$\tan \bar{\theta} = \frac{2}{\pi} \int_0^{\pi/2} \tan \theta a(\theta) d\theta \quad (2)$$

where $a(\theta)$ is a function describing the distribution of the tilts θ in the crater and in the flat surface element to which the crater belongs, weighted by the fractional area covered by the crater compared to that of the flat surface. In Eq. (2), θ is the angle of a given facet from horizontal, and $a(\theta)$ is the distribution of surface slopes (see also Emery et al. 1998). The mean surface slope does not depend on the illumination, but it is an intrinsic property of the surface.

Instead of explicitly calculating the heat diffusion within craters (Delbo’ and Tanga 2009), the analytical approximation of Lagerros (1998) is used. The Lagerros crater approximation is applicable if the thermal infrared fluxes were obtained at lower phase angles ($\lesssim 30 - 40^\circ$), which is the case of the WISE data of most MBAs. According to our tests, the differences in the fluxes produced by these two models are usually smaller than 1%.

We apply the color correction to model fluxes the same way as in Alí-Lagoa et al. (2014); Hanuš et al. (2015).

We run the TPM model for different values of the thermal inertia $\Gamma \in (0, 2500) \text{ J m}^{-2} \text{ s}^{-1/2} \text{ K}^{-1}$. For each value of the surface roughness, we run the TPM for the thermal inertia $\Gamma = 2500 \text{ J m}^{-2} \text{ s}^{-1/2} \text{ K}^{-1}$ and the Bond albedo $A = 0.08$, and

get the first size estimate D . Before each following TPM run (while keeping the same surface roughness), we first compute the new value of the Bond albedo A from the equation (see, e.g., Harris and Lagerros 2002)

$$D(\text{km}) = \frac{1329}{\sqrt{p_V}} 10^{-0.2H}, \quad (3)$$

where we use diameter D determined in the previous TPM run, and where the visible geometric albedo p_V can be expressed via $A = q p_V$, where $q = 0.290 + 0.684G$ is the phase integral (Bowell et al. 1989). We utilize the values of absolute magnitudes H and slopes G from the Asteroid absolute magnitude and slope catalog⁴ (AAMS, Muinonen et al. 2010; Oszkiewicz et al. 2011). We then run the TPM model with decreasing values of Γ until $\Gamma = 0$. Following each step, we always recompute the A value. The same procedure is performed for ten different values of the surface roughness.

We set emissivity to $\epsilon = 0.9$ as this is appropriate for objects with surfaces that emit a substantial portion of their thermal-infrared radiation shortwards of $8 \mu\text{m}$ (Lim et al. 2005).

We do not account for the uncertainty in the H and G values. According to our tests (TPM with different H values), a change of ± 0.5 mag in H is compensated by the change of the Bond albedo A (or p_V). However, the size remains similar (see Eq. 3). Moreover, the thermal inertia is not sensitive on H either.

Due to the uncertainty in the rotation period, we have the typical uncertainty in the rotation phase of the asteroid of about 10° . Therefore, we treat the initial rotation phase ϕ_0 as a free parameter of the model to be adjusted by the best fitting procedure. We run the TPM scheme with different ϕ_0 values from the expected interval (usually $\pm 10^\circ$) given by the uncertainty in the rotation period with a step of 2° .

After scanning the parameter space of thermal inertia, surface roughness, initial rotational phase and Bond albedo, we find the solution with the lowest χ^2 value.

To determine the uncertainties of thermal inertia Γ , diameter D and Bond albedo A for a TPM solution with a single shape model (i.e., the model from DAMIT), we utilize the standard statistical tools based on χ^2 values. This approach for the uncertainty determination described, for example, in Press et al. (1986) has been commonly used (see, e.g., Alí-Lagoa et al. 2014; Emery et al. 2014; Hanuš et al. 2015). First, we find all solutions within the 1σ confidence interval, i.e., solutions with $\chi^2 < (\chi_{\min}^2 + \sqrt{2\nu})$, where we consider $\sqrt{2\nu} \sim \sigma$ and ν is the effective number of degrees of freedom. The range of possible solutions gives us then the upper and lower bounds of the derived parameter uncertainties. However, this approach gives reliable uncertainties if the χ^2 values of the best-fitting solutions are comparable to the number of degrees of freedom (i.e., if the

⁴<http://wiki.helsinki.fi/display/PSR/Asteroid+absolute+magnitude+and+slope>

reduced $\chi^2 \sim 1$), which is often not the case. Unfortunately, the contribution of the uncertainty of the shape model and the rotation state to the uncertainties of derived thermophysical properties is completely ignored here.

To overcome the difficulties with the unrealistic uncertainties when the χ^2 values are high, we estimate the uncertainties of the searched parameters by an empirical approach: we accept all solutions with $\chi^2 < (\chi_{\min}^2 + \chi_{\min}^2 \sqrt{2\nu})$. This follows the procedure applied in Hanuš et al. (2015).

We prefer to use reduced chi-square values $\chi_{\text{red}}^2 = \chi^2/\nu$, which are more illustrative than the “non-reduced” χ^2 .

To estimate the uncertainties of derived thermophysical properties (Γ , D or A) based on the VS-TPM, we use an empirical method. We only consider the best-fitting solution for each varied shape. We find the smallest range within 14 solutions (corresponds to $\sim 68\%$ of the total number of 20). For example, each varied shape gives us a thermal inertia value. We sort these values and find the lowest range given by 14 thermal inertia values and compute the mean value. This usually rejects the most extreme values of Γ . Values of the thermophysical parameters with their uncertainties estimated by this method are included in Table A.3.

4. Results and discussion

4.1. VS-TPM of three hundred asteroids

We applied the VS-TPM to ~ 280 asteroids with shape models and sufficient amount of thermal infrared data from WISE. We obtained five qualitative VS-TPM results, which are illustrated in Fig. 1:

- a) TPM solutions for all/most varied shapes are similar, they have reasonably low χ_{red}^2 values and a prominent minimum in Γ (Fig. 1a).
- b) TPM solutions for all/most varied shapes are similar, they have reasonably low χ_{red}^2 values, however, without a prominent minimum in Γ . Thermophysical properties cannot be constrained (Fig. 1b).
- c) TPM solutions for all/most varied shapes exhibit similar trends (i.e., a qualitatively similar shape of the minimum) with a prominent minimum in Γ , but the range in the χ_{red}^2 is large (~ 5 – 10). Hence, the quality of the TPM fits depends on the varied shapes. However, the thermophysical parameters are consistent and well constrained across the varied shapes solutions (Fig. 1c).
- d) TPM solutions for varied shapes are different, which suggests that the shape model uncertainty is important. Reliable thermophysical properties cannot be derived (Fig. 1d).
- e) All TPM solutions have large χ_{red}^2 values, so the thermophysical properties are not reliable (Fig. 1e).

Reliable thermophysical properties can be obtained in cases a) and c). Therefore, we only present these results in Table A.3). These cases represent ~ 120 out of the initial ~ 280 asteroids, for which we applied the VS-TPM. Most of the remaining cases fall to the b) (~ 50) and d) (~ 100) categories and only a few to the e) category.

Case b) usually happens if the thermal infrared dataset is rather small and/or with large uncertainties, the rotation period is too long ($\gtrsim 15$ h) or the geometry of observation is close to pole-on.

The category d) represents asteroids, for which the TPM fits are dependent on the varied shapes, so on the uncertainty in the shape model. Future shape model refinement by additional optical photometry would be necessary for obtaining a useful TPM solution.

The category e) correspond to cases likely affected by systematic effects. These could include incorrect rotation state (e.g., rotation period) or the shape, or incorrect fluxes (e.g., there could be a substantial offset of an individual flux measurement or we made an error in the data processing). As an example, we show asteroid (830) Petropolitana in Fig. 1e. The shape model presented in Hanuš et al. (2016b) is likely wrong, because the shape and spin state solution was searched near the rotation period of ~ 39 hours available at the CdR&CdL⁵ database. However, the true period seems to be much longer (~ 169 h, personal communication with Dagmara Oszkiewicz and recent unpublished observations of Brian Skiff). We replaced the incorrect solution in DAMIT by the revised one and repeated the VS-TPM scheme. We obtained a significantly better fit to the thermal infrared data, however, the minimum in Γ is rather broad, so thermal inertia cannot be constrained (Fig. 1f).

In our figures of Γ vs. χ_{red}^2 (see Fig. 1 and figures in the Appendix), we show the TPM solution with a nominal shape model as an input and for all (19) the varied shapes.

The standard uncertainty values based on the χ^2 statistics are reliable only for a sub-sample of our studied asteroids. For the remaining asteroids, the χ_{red}^2 values are higher than ~ 1 (see column 15 in Table A.3). We utilized here the semi-empirical approach for the uncertainty estimation described in Sect. 3.

The χ_{red}^2 values of ~ 2 – 5 for the best-fitting set of parameters indicate that we are not fitting the thermal fluxes by our model very well. However, if the fit has a prominent minimum in Γ and if the solution is consistent within the varied shapes, we consider such solution as reliable. The rather worse fit to the thermal data could be explained by two main reasons: (i) The tabulated uncertainties of the WISE data may not correspond to the 1σ standard errors. We already increased the error bars based on the comparison of measurements taken in consecutive exposures (see discussion in Hanuš et al. 2015, Fig. 8), but there could be other biases that remain unaccounted for. Moreover, possible systematic errors in the WISE fluxes could be present, however, we do not have control on them other than that clear outliers could be identified. (ii) Model uncertainties (convex shape, pole orientation, systematics of the TPM) dominate over the flux uncertainties.

⁵http://obswww.unige.ch/~behrend/page_cou.html

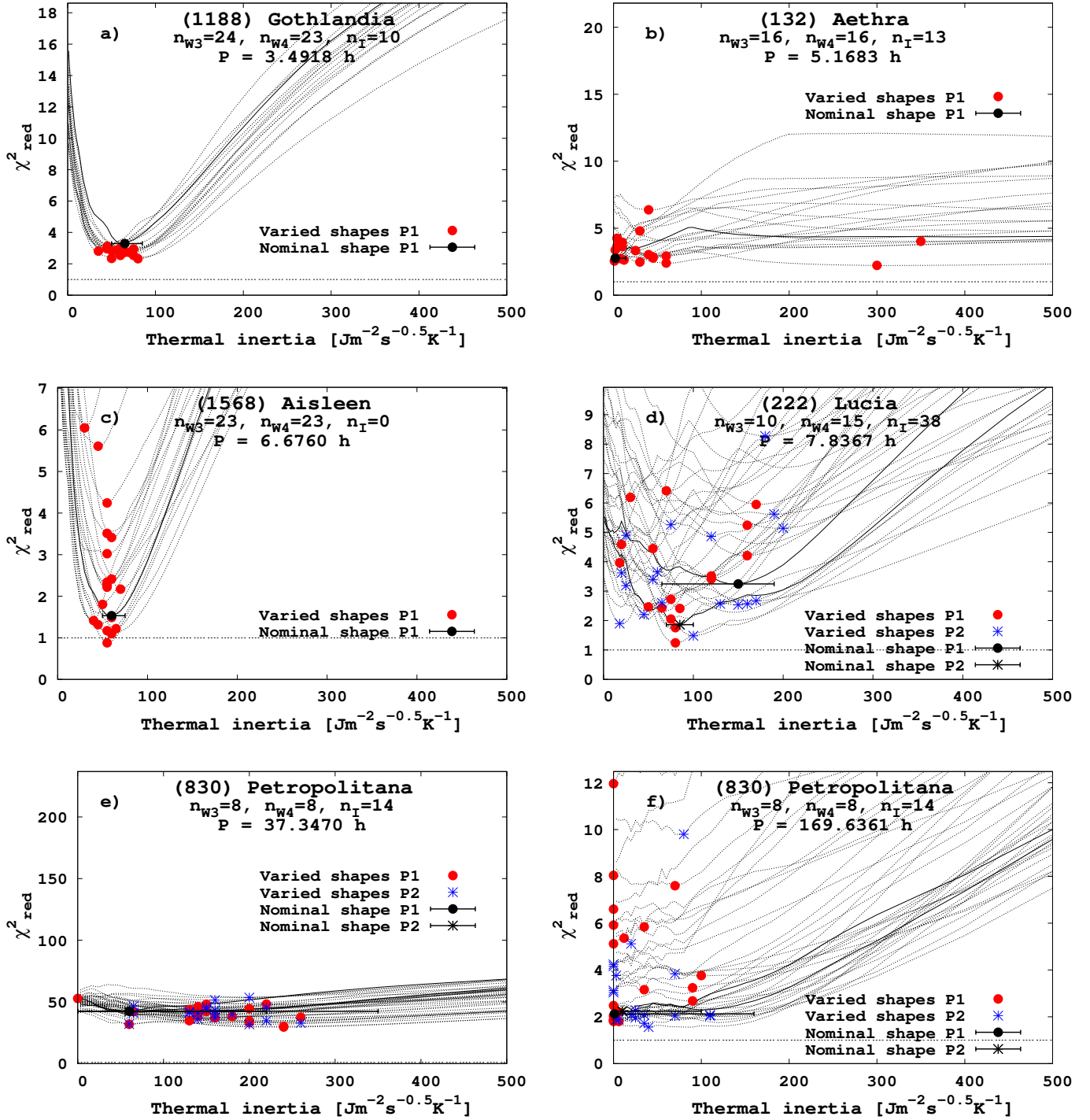


Figure 1: Typical VS-TPM fits in the thermal inertia parameter space. We illustrate here five (a-e) qualitative results discussed in the text. Each plot also contains the number of thermal infrared measurements in WISE W3 and W4 filters and in all IRAS filters, and the rotation period. Case f) corresponds to the corrected/ revised shape and spin solution of asteroid (830) Petropolitana. P1 and P2 corresponds to ambiguous pole solutions.

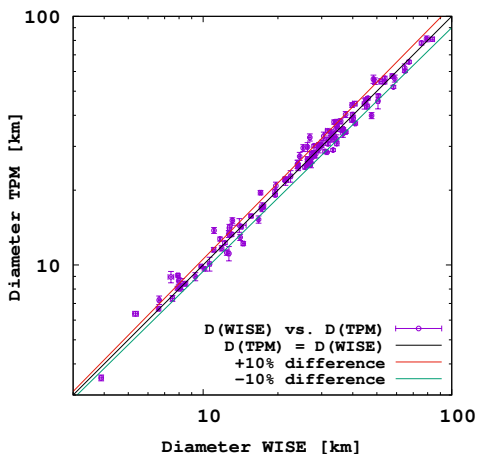


Figure 2: Comparison between our sizes derived by the VS-TPM and radiometric sizes based on NEATM from Mainzer et al. (2016). Both methods use the same thermal infrared datasets.

For most asteroids, the VS-TPM can produce a better fit than the classical TPM with the published shape model. All varied shape models, although different in the goodness of thermal IR data fit, are indistinguishable in terms of reproducing the visible photometry. On the other hand, our method is not a true optimization, it rather maps the uncertainties in the shape and the pole orientation and their influence on the TPM results.

Selecting 14 out of 20 varied-shape solutions for the estimation of fitted parameters and their uncertainties allowed us to reject potential unrealistic solutions that could originate from specific (peculiar) bootstrapped photometric datasets.

Another intriguing result is the fact that we obtained TPM fits with a large range of χ_{red}^2 values for a number of studied asteroids, however, with similar appearance of the minimum in Γ (Fig. 1c). This suggests a substantially different quality of the fits within the varied shape models on one side, and a stable TPM solution in Γ on the other side. Some of the shape models produce χ_{red}^2 values larger by a factor up to 5–10 than the best fitting varied shape model. We illustrate such TPM fits for asteroid (1568) Aisleen in Fig. 1c. It is clear that the shape model (together with the pole orientation) is an important limiting factor for the quality of the fit, and so for a number of varied shapes we do not fit the thermal data well. On the other hand, we suspect that the quality of the TPM fit could be improved in the future when more realistic shape models will become available. The results of investigation of the stability of the TPM solution with respect to the shape model variations raise the confidence that for most asteroids presented in this study, the thermophysical solution is stable, and so derived thermophysical properties are realistic.

5. Interpretation of derived thermophysical properties

5.1. Sizes

We compared in Fig. 2 our diameters computed by the VS-TPM with the radiometric diameters reported by Mainzer et al.

(2016). Both diameters are based on the WISE thermal infrared data, so their differences of even 10% has to originate in the different models utilized (i.e., of the TPM and NEATM). It is obvious that the spherical shape model used in the NEATM is a crude approximation, especially for elongated objects, because their projected sizes strongly depends on the geometry of the observation. If we study the asteroid populations from a global perspective, where we do not need accurate values for individual objects, the radiometric sizes still represent the best choice. Indeed, utilizing a large statistical sample (e.g., for the size frequency distributions of different populations used for the comparisons to the results of numerical models) averages the role of the non-spherical shape, and so these size samples are reliable (the reliability of the sizes based on NEATM model and thermal data is discussed by Usui et al. 2014). The size comparison in Fig. 2 indicates that our sizes are consistent with the radiometric sizes of Mainzer et al. (2016).

Our VS-TPM results only represent asteroids with sizes between 5 and 100 km. For larger asteroids, WISE data are usually affected by saturation, and for smaller asteroids, we do not have sets of lightcurves good enough to successfully obtain the shape models. It may be possible to correct for partial saturation, but we chose not to do it, because it has not been characterized for asteroids in particular, which would complicate the TPM interpretation. To increase our statistical sample on asteroids with larger and smaller sizes, we searched the literature for reported values of thermal inertia, size, and albedo determined by other authors (mostly by different TPM implementations) and present them together with the references in Table A.2.

5.2. Thermal inertia values

We investigate the relationship between asteroid diameters and thermal inertias for all asteroids in our sample (~120 our determinations and 60 previously published values), but also for subgroups with respect to the albedo, taxonomy class, family membership or sidereal rotational period. It is not straightforward to compare thermal inertia values obtained at different heliocentric distances r_{hel} , because Γ is a function of the temperature T , hence r_{hel} (see, e.g., Keihm 1984; Mueller et al. 2010; Delbo' et al. 2015)

$$\Gamma \propto T^{3/2} \propto r_{\text{hel}}^{-3/4}. \quad (4)$$

We normalized the resulting thermal inertia values of all asteroids to $r_{\text{hel}} = 1$ au. We note that this model assumes that all the observations are obtained at similar r_{hel} . However, for some asteroids, observations at two distinct epochs, thus r_{hel} , are available. We provide the average value of r_{hel} in Table A.3, which introduces only a small inaccuracy, because the differences in r_{hel} between the two epochs are usually rather small. Most of the asteroids in our sample are from the main belt and were observed by WISE at typical heliocentric distances of $r_{\text{hel}} \sim 2 - 3.5$ au, which implies only a small correction of the thermal inertia. In the following, we use the corrected thermal inertia values, while Table A.3 provides the original values of Γ together with the heliocentric distance r_{hel} .

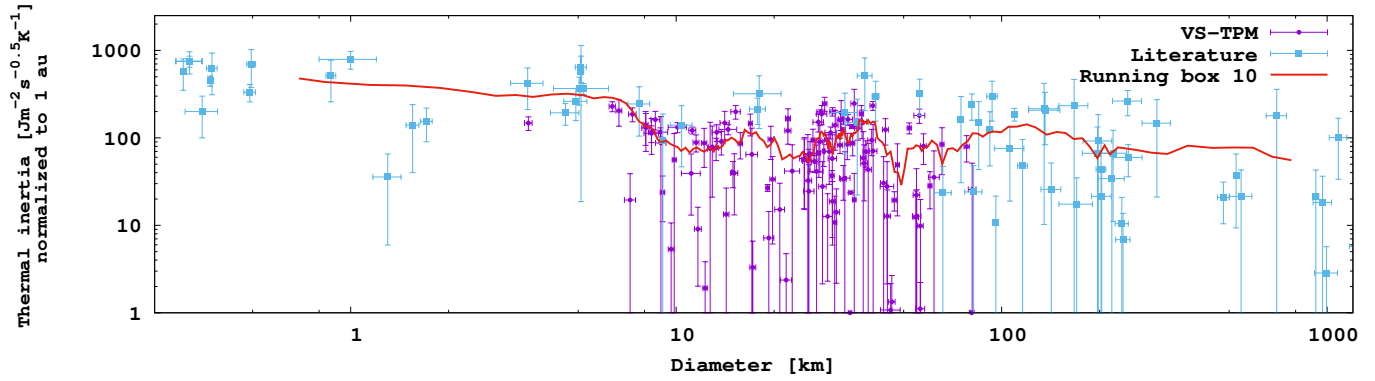


Figure 3: Dependence of the thermal inertia Γ on asteroid diameter D . We included our estimates (circles) and adopted literature values (squares).

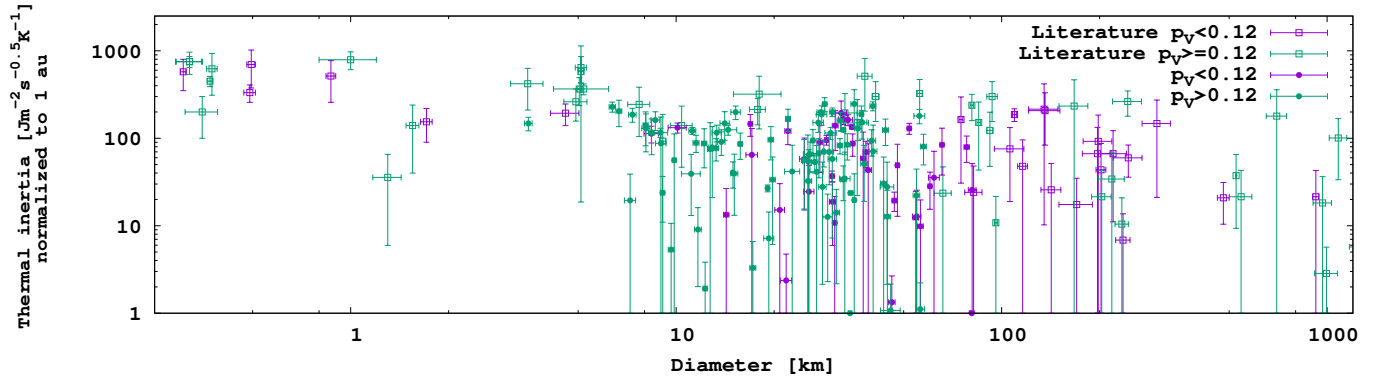


Figure 4: Dependence of the thermal inertia Γ on asteroid diameter D for the low ($p_V < 0.12$) and high ($p_V > 0.12$) albedo objects. We included our estimates (circles) and adopted literature values (squares).

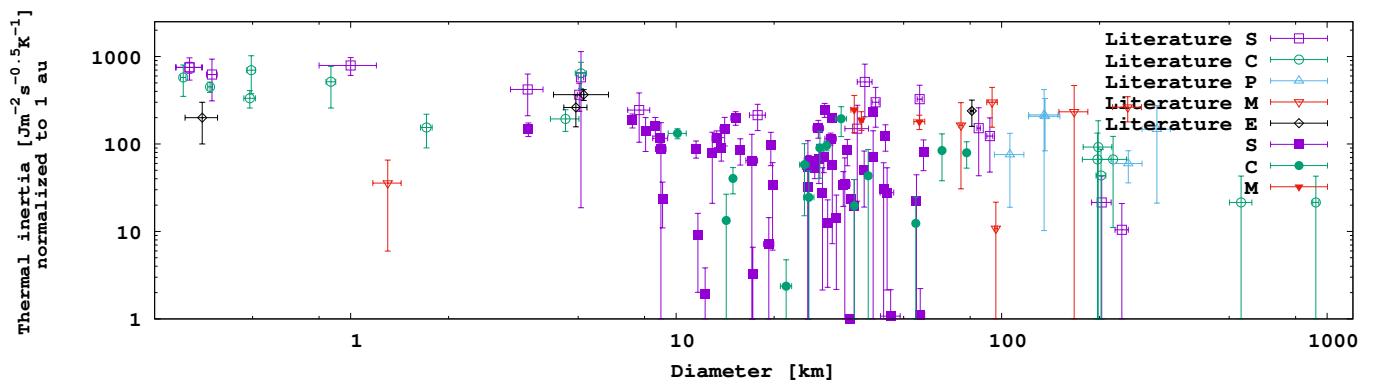


Figure 5: Dependence of the thermal inertia Γ on asteroid diameter D for asteroids from S- and C-complexes, and P, M, and E types. We included our estimates and adopted literature values.

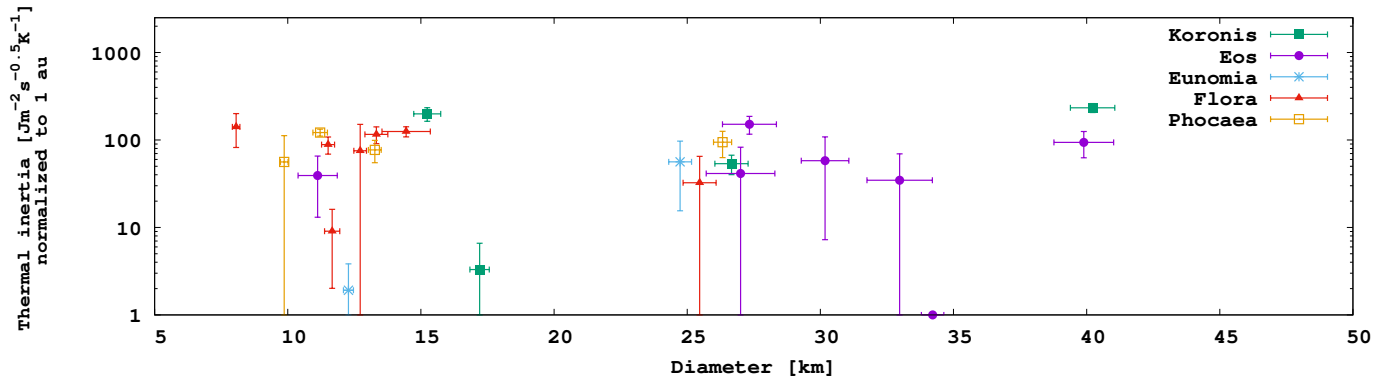


Figure 6: Dependence of the thermal inertia Γ on asteroid diameter D for members of five collisional families – Flora, Koronis, Eos, Eunomia and Phocaea.

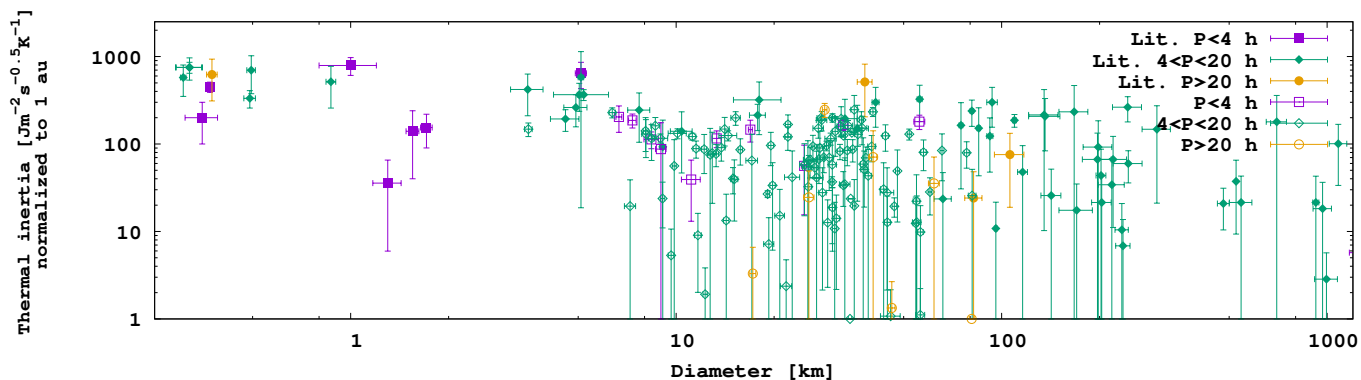


Figure 7: Dependence of the thermal inertia Γ on asteroid diameter D for the fast ($P < 4$ h), intermediate ($4 < P < 20$ h), and slow ($P > 20$ h) rotators. We also included the literature values.

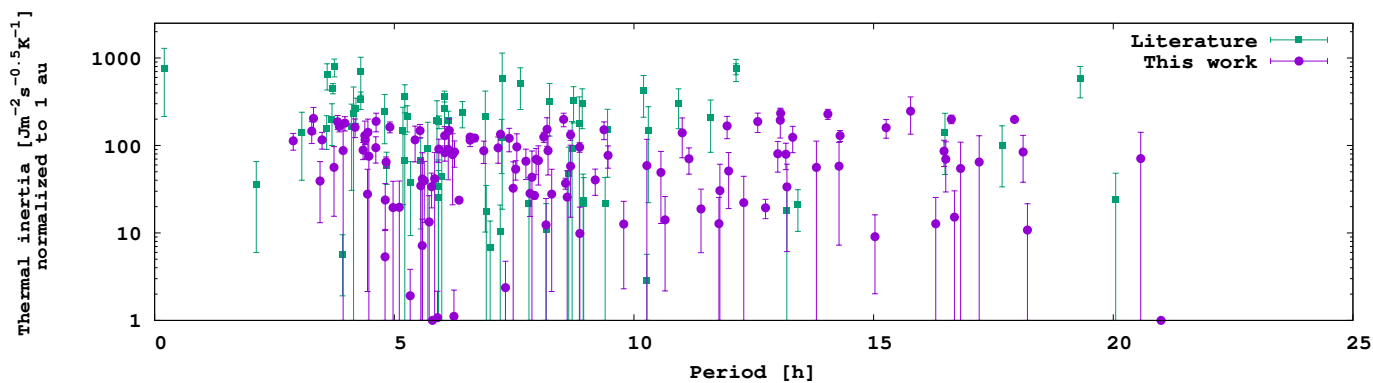


Figure 8: Dependence of the thermal inertia Γ on asteroid rotation period P . We also included the literature values.

In Fig. 3, we compare the D vs. Γ dependence of our whole sample. We also show the running box in Γ of ten values to illustrate potential trend with size. Values of Γ for most of our asteroids are between 0 and $200 \text{ J m}^{-2} \text{ s}^{-1/2} \text{ K}^{-1}$ and have large uncertainties. Considering all the Γ values available, the trend of the increasing thermal inertia with decreasing size suggested in Delbo' et al. (2007) seems evident: the largest objects with $D > 500 \text{ km}$ have $\Gamma \lesssim 20 \text{ J m}^{-2} \text{ s}^{-1/2} \text{ K}^{-1}$, typical thermal inertia is then growing with decreasing size, is $\sim 100 \text{ J m}^{-2} \text{ s}^{-1/2} \text{ K}^{-1}$ for objects between 10 and 100 km, and is reaching its maximum of several hundreds for kilometer-sized objects. It is also possible that in the size range between 5 and 100 km, covered by our new thermal inertia determinations, Γ does not exhibit a significant trend in D vs. Γ . This would indicate a sudden increase of Γ values for sizes $< 10 \text{ km}$. The dispersion of the thermal inertia within similar size ranges is rather high, which could imply various grain sizes of the surface regolith. However, this conclusion is not very robust because of the large error bars affecting the values of the thermal inertia.

The Γ values obtained from the literature seem to be, in general, larger than values derived here. This is mostly because both sources sample different populations. The adopted thermal inertia values correspond either to NEAs ($D < 5 \text{ km}$) or to large asteroids ($D > 100 \text{ km}$) and TNOs. For NEAs, we expect higher Γ values than in our sample due to the Γ vs. size inverse dependence. For TNOs, we suspect that the simple dependence following Eq. (4) might not be a reliable approximation, because their surface temperature is significantly lower than for main-belt asteroids. For D in the 5–100 km range, the few literature values of Γ tend to be larger than our values. However, the literature values of Γ have rather large uncertainties and we also suffer by the low number statistics. Moreover, the adopted Γ values in the size range of 5–100 km were mostly derived based on the IRAS thermal measurements (Delbo' and Tanga 2009) that usually have uncertainties $> 10\%$. Another possible reason is that the Gamma values from the literature are not based on VS-TPM. So, the classical TPM uses one of the shapes (the nominal), which might not be the best one to interpret the thermal IR data. Therefore, we have some doubts about their reliability.

There is a group of objects with diameters $< 80 \text{ km}$ with very low ($\Gamma < 20 \text{ J m}^{-2} \text{ s}^{-1/2} \text{ K}^{-1}$) thermal inertias that is observed for the first time. These objects should be covered by a layer of fine and mature regolith. Such fine regolith is a product of thermal disintegration and/or micrometeorite bombardment of larger rocks (Delbo' et al. 2014). In both cases, the asteroid in the size range of several tens of kilometers needs millions of years to build up a fine regolith layer and this timescale is comparable or even larger than the collisional lifetime. In this sense, asteroids with low Γ could be those who were lucky enough to avoid recent collisional event that would remove the fine-grained material from the surface (i.e., essentially increase Γ).

In Fig. 4, we plot the D vs. Γ dependence for the low ($p_V < 0.12$) and high ($p_V > 0.12$) albedo objects. We chose the value of $p_V = 0.12$, because it corresponds to the border between S-complex (high albedo) and C-complex (low albedo) taxonomy class asteroids (see also the Supp. Materials of

Delbo' et al. 2017). The only obvious correlation in this plot is the selection effect of the lightcurve inversion method – the majority of photometric data for smaller objects ($D \lesssim 20 \text{ km}$) is strongly biased towards the inner main belt and objects with higher albedo. We note that mid- and larger sized low-albedo objects are less likely to be in our sample because they saturate.

By using the SMASS II (Bus and Binzel 2002) and the Tholen (Tholen 1984, 1989) taxonomy, we assigned the taxonomic classification (if available) to the asteroids in our sample. For the purpose of our study, we distinguished S- and C-complexes (we included S, Q, Sa, Sq, Sr, Sk, Sl into the S-complex and B, C, Cb, Ch, Cg, Cgh into the C-complex) and split the X-complex into P, M, and E types according to their albedos ($p_V < 0.10$ for P, $0.10 < p_V < 0.30$ for M, and $p_V > 0.30$ for E types). For few asteroids with unknown taxonomy classification, we adopted the taxonomic assignment from DeMeo and Carry (2013), which is based on the colors from the Sloan Digital Sky Survey. However, this approach is not always reliable for individual objects, so we also checked in these cases the values of the geometric visible albedo p_V . In Fig. 5, we plot the D vs. Γ dependence with respect to the most represented taxonomic types (S- and C-complexes, P, M, and E types). Thermal inertia values from the literature for M-types already seem, in average, larger than for S- and C-types. Our few additional solutions further supports this behavior. Moreover, E-types seem to have, in average, larger Γ values as well, although the statistical sample is rather small and dominated by small ($D < 10 \text{ km}$) objects.

We have five asteroid families that are represented in our sample by at least two members – Flora, Koronis, Eos, Eunomia and Phocaea. Most of the convex shape models of asteroids that belong to these asteroid families were already studied by Hanuš et al. (2013a), from where we also adopted the membership revision, which is an essential procedure. Indeed, the initial family membership assignment is adopted from Nesvorný et al. (2015), who used the hierarchical clustering method (HCM, see e.g., Zappalà et al. 1990, 1994). However, such family lists are contaminated by interlopers and the membership of each individual object should be carefully checked, for example, by considering the taxonomic type, the albedo or the color. In Fig. 6, we plot the D vs. Γ dependence for asteroids that belong to these five asteroid families, where we excluded interlopers reported in Hanuš et al. (2013a). Thermal inertia values within these asteroid families (e.g., Flora, Eos, Eunomia) are rather consistent, we only have few values of thermal inertia $< 20 \text{ J m}^{-2} \text{ s}^{-1/2} \text{ K}^{-1}$, which could suggest different regolith grain size on the surface even for objects of common origin (i.e., same age and composition as is usually expected for family members). Alternatively, these objects could not be real members of the family or derived Γ values are wrong. The small Γ values of some family members could be an important link to non-catastrophic collisions that could refresh the surface and to the processes that could create the regolith (Delbo' et al. 2014). Noticeable differences in thermal inertia values are present in the Koronis family. Two asteroids have thermal inertia values $\sim 100 \text{ J m}^{-2} \text{ s}^{-1/2} \text{ K}^{-1}$, while the other two $\sim 0\text{--}20 \text{ J m}^{-2} \text{ s}^{-1/2} \text{ K}^{-1}$. We suspect that some of the asteroids

are not true members of the Koronis family. Specifically, asteroids (167) Urda and (311) Claudia are borderline cases based on their positions in the proper semi-major axis vs. size plot (Hanuš et al. 2013a), and asteroid (1742) Schaifers has quite a low albedo (0.11) compared to the typical albedos of the Koronis family members (average value is 0.22, the range is about ± 0.1). In this sense, asteroid (1618) Dawn represents the only truly reliable member of the Koronis family. Asteroid (311) Claudia has a consistent thermal inertia value to that of asteroid Dawn, which might support its membership in the Koronis family.

We show the VS-TPM fits in the thermal inertia parameter space for individual asteroids from Eos, Flora, Koronis and Phocaea collisional families in Figs. B.9, B.10, B.11 and B.12. Thermal inertia values are rather consistent within the individual families, however, some minor differences are noticeable. Unfortunately, improvements in the thermal inertia determinations (i.e., lowering the uncertainties) and/or enlargement of the statistical sample are necessary.

For fast rotating asteroids, it could be difficult to retain the very fine regolith grains on their surface because of the centrifugal force, and thus higher thermal inertias could be preferred. Another mechanism to consider is the thermal fatigue – fast rotators should not experience large temperature differences during the day and night, and so the thermal cracking mechanism of Delbo’ et al. (2014) should not be that efficient as for intermediate rotators. To investigate the potential fingerprints of these scenarios, we show the D vs. Γ dependence for the fast ($P < 4$ h, objects close to the disruption limit), intermediate ($4 < P < 20$ h, objects with a common rotation), and slow ($P > 20$ h) rotators in Fig. 7 and the dependence of the thermal inertia Γ on asteroid rotation period P in Fig. 8. There are only two out of 17 fast rotating asteroids, which ranges of Γ cover low values ($< 40 \text{ J m}^{-2} \text{ s}^{-1/2} \text{ K}^{-1}$). On the other hand, values of $\Gamma > 40 \text{ J m}^{-2} \text{ s}^{-1/2} \text{ K}^{-1}$ are still possible for these objects. Therefore, all these fast rotating asteroids could have higher thermal inertias. Unfortunately, our Γ values are not constrained to a necessary resolution to draw a more reliable conclusions. So, the D vs. Γ dependence in Fig. 7 does not show any significant correlation.

6. Conclusions

We performed thermophysical modeling of three hundred asteroids using the VS-TPM analysis, which produced acceptable fits (i.e., a reasonable minimum in the thermal inertia) to the thermal data for 122 asteroids. We report their thermophysical properties such as size, thermal inertia, surface roughness and geometric visible albedo (Table A.3). This work increased the number of asteroids with determined thermophysical properties, especially thermal inertias by about a factor of three. We attempted VS-TPM for ~ 280 asteroids in total, but for ~ 150 of these bodies, the shape model and pole orientation uncertainties, specific rotation or thermophysical properties, poor thermal infrared data or their coverage prevented the determination of reliable thermophysical properties.

Derived sizes and geometric visible albedos are usually well constrained and have their uncertainties smaller than 10% and

30%, respectively. Moreover, our sizes (and albedos) are consistent with the radiometric sizes based on the NEATM from Mainzer et al. (2016) as is illustrated in Fig. 2. Both sizes are based on the same thermal infrared dataset. On the other hand, the values of thermal inertia are significantly less constrained, which makes their interpretation difficult. Although some insight into the physical properties of main-belt asteroids can be made, unfortunately, improvements in the thermal inertia determinations (i.e., lowering the uncertainties) are still desired. This could be driven mostly by improvements in the shape models by utilizing additional photometric data for the shape modeling or by improvements of the TPM model, where, for instance, both optical and thermal infrared data could be utilized (CITPM, Ďurech et al. 2017). Also, new space-based thermal infrared measurements such as those obtained by the WISE satellite would greatly help.

There is no doubt that the shape model and pole orientation uncertainty plays an important role for the thermophysical modeling and is the main reason for the low number of well constrained solutions and the large uncertainties of thermal inertia values. Specifically, the VS-TPM shows, in many cases, strong dependence of the thermophysical fit on the individual varied shape models. Often, the χ^2 values of fits with some varied shape models are extremely large, so these solutions cannot be even accepted, but other varied shape models (of the same asteroid) fit the thermal infrared data reasonably well. Also, we have cases with inconsistent TPM fits with similar χ^2 values within the varied shapes.

The VS-TPM allowed us to remove the pole ambiguity for seven asteroids. In all these cases, the TPM fits within the varied shapes that corresponded to the same original pole solution were clearly better than for the second (ambiguous) pole solution. We label these asteroids in Table A.3.

We confirmed the correlation between the size and the thermal inertia proposed by Delbo’ et al. (2007), however, the range of the thermal inertia for similar sizes is large and usually varies between zero and few hundreds (in the size range of 10–100 km). In general, larger objects have lower thermal inertia values.

Surprisingly, we derived very low ($< 20 \text{ J m}^{-2} \text{ s}^{-1/2} \text{ K}^{-1}$) thermal inertias for several asteroids (~ 10) with various sizes. Asteroids with such properties that suggest a mature regolith on the surface are reported for the first time. We note that the uncertainties of thermal inertias for most of these asteroids are rather large and cover values even up to $100 \text{ J m}^{-2} \text{ s}^{-1/2} \text{ K}^{-1}$. Further confirmation of the low Γ values by utilizing additional optical and/or thermal infrared data is desired. Thermal inertia values within several asteroid families are rather consistent with no obvious trends. However, we still have only few members in each studied family, which makes any interpretation difficult due to the low number statistics.

The fast rotators with $P \lesssim 4$ hours seem to have slightly larger thermal inertia values, so do not likely have a fine regolith on the surface. This could be explained, for example, by the loss of the fine regolith due to the centrifugal force, or by the ineffectiveness of the regolith production (e.g., by the thermal cracking mechanism of Delbo’ et al. 2014).

Our current work represents a characterization effort to provide a context to whatever we learn about individual objects from missions and extensive studies of single objects. We provide thermal inertias for a set of MBAs in a size range that had almost no previous information. Still, this work shows that increasing the number of known thermal inertia values by a factor of three to ~200 is not enough to push forward our understanding of the physical properties of asteroids. Therefore, we likely need dedicated studies (e.g., collisional families) that spend a few years on lightcurve observations, and maybe more missions such as the WISE satellite. The Near-Earth Object Camera (NEOCam, Mainzer et al. 2015) could be the next major driver for the new knowledge concerning the thermophysical properties of asteroids.

Regarding future improvements on the TPM, it should happen based on studying the very few targets with ground-truth knowledge of physical properties and rich (thermal) data sets (e.g., Rozitis 2017). Or maybe with thermal infrared data from spacecraft missions (OSIRIS-REx data, Lauretta et al. 2015).

Acknowledgements

The computations have been done on the “Mesocentre” computers, hosted by the Observatoire de la Côte d’Azur.

JH was supported by the grant 17-00774S of the Czech Science Foundation and JD by the grant 15-04816S of the Czech Science Foundation.

VAL and MD acknowledge support from the NEOShield-2 project, which has received funding from the European Unions Horizon 2020 research and innovation programme under grant agreement no. 640351.

VAL: The research leading to these results has received funding from the European Unions Horizon 2020 Research and Innovation Programme, under Grant Agreement no 687378.

This publication uses data products from NEOWISE, a project of the Jet Propulsion Laboratory/California Institute of Technology, funded by the Planetary Science Division of the NASA. We made use of the NASA/IPAC Infrared Science Archive, which is operated by the Jet Propulsion Laboratory, California Institute of Technology, under contract with the NASA.

References

Alf-Lagoa, V., Lionni, L., Delbo', M., Gundlach, B., Blum, J., Licandro, J., 2014. Thermophysical properties of near-Earth asteroid (341843) 2008 EV₅ from WISE data. *Astronomy and Astrophysics* 561, A45. 1310. 6715.

Bottke, J.W.F., Vokrouhlický, D., Rubincam, D.P., Nesvorný, D., 2006. The Yarkovsky and Yorp Effects: Implications for Asteroid Dynamics. *Annual Review of Earth and Planetary Sciences* 34, 157–191.

Bowell, E., Hapke, B., Domingue, D., Lumme, K., Peltoniemi, J., Harris, A.W., 1989. Application of photometric models to asteroids, in: Binzel, R.P., Gehrels, T., Matthews, M.S. (Eds.), *Asteroids II*, University of Arizona Press. pp. 524–556.

Brinsfield, J.W., 2009. Asteroid Lightcurve Analysis at the Via Capote Observatory: 2009 1st Quarter. *Minor Planet Bulletin* 36, 127–128.

Bus, S.J., Binzel, R.P., 2002. Phase II of the Small Main-Belt Asteroid Spectroscopic Survey: A Feature-Based Taxonomy. *Icarus* 158, 146–177.

Carry, B., Merline, W.J., Kaasalainen, M., Conrad, A., Drummond, J.D., Dumas, C., Kueppers, M., OSIRIS Instrument Team, 2010. The KOALA Shape Modeling Technique Validated at (21) Lutetia by ESA Rosetta Mission, in: AAS/Division for Planetary Sciences Meeting Abstracts #42, p. 1050.

Cruikshank, D.P., Stansberry, J.A., Emery, J.P., Fernández, Y.R., Werner, M.W., Trilling, D.E., Rieke, G.H., 2005. The High-Albedo Kuiper Belt Object (55565) 2002 AW₁₉₇. *Astrophysical Journal, Letters* 624, L53–L56.

Cutri, R.M., Wright, E.L., Conrow, T., Bauer, J., Benford, D., Brandenburg, H., Dailey, J., Eisenhardt, P.R.M., Evans, T., Fajardo-Acosta, S., Fowler, J., Gelino, C., Grillmair, C., Harbut, M., Hoffman, D., Jarrett, T., Kirkpatrick, J.D., Leisawitz, D., Liu, W., Mainzer, A., Marsh, K., Masci, F., McCallon, H., Padgett, D., Ressler, M.E., Royer, D., Skrutskie, M.F., Stanford, S.A., Wyatt, P.L., Tholen, D., Tsai, C.W., Wachter, S., Wheelock, S.L., Yan, L., Alles, R., Beck, R., Grav, T., Masiero, J., McCollum, B., McGehee, P., Papin, M., Wittman, M., 2012. Explanatory Supplement to the WISE All-Sky Data Release Products. Technical Report.

Delbo', M., 2004. The nature of near-earth asteroids from the study of their thermal infrared emission. PhD thesis - Freie Universitaet Berlin, 1–210.

Delbo', M., dell'Oro, A., Harris, A.W., Mottola, S., Mueller, M., 2007. Thermal inertia of near-Earth asteroids and implications for the magnitude of the Yarkovsky effect. *Icarus* 190, 236–249. 0704. 1915.

Delbo', M., Libourel, G., Wilkerson, J., Murdoch, N., Michel, P., Ramesh, K.T., Ganino, C., Verati, C., Marchi, S., 2014. Thermal fatigue as the origin of regolith on small asteroids. *Nature* 508, 233–236.

Delbo', M., Mueller, M., Emery, J., Rozitis, B., Capria, M.T., 2015. Asteroid thermophysical modeling, in: Michel, P., DeMeo, F.E., Bottke, W.F. (Eds.), *Asteroids IV*, The University of Arizona Press. pp. 107–128.

Delbo', M., Tanga, P., 2009. Thermal inertia of main belt asteroids smaller than 100 km from IRAS data. *Planetary and Space Science* 57, 259–265. 0808. 0869.

Delbo', M., Walsh, K., Bolin, B., Avdellidou, C., Morbidelli, A., 2017. Identification of a primordial asteroid family constrains the original planetesimal population. *Science* 357, 1026–1029.

DeMeo, F.E., Carry, B., 2013. The taxonomic distribution of asteroids from multi-filter all-sky photometric surveys. *Icarus* 226, 723–741. 1307. 2424.

Đurech, J., Delbo', M., Carry, B., Hanuš, J., Alf-Lagoa, V., 2017. Asteroid shapes and thermal properties from combined optical and mid-infrared photometry inversion. *Astronomy and Astrophysics* 604, A27. 1706. 01232.

Đurech, J., Kaasalainen, M., Herald, D., Dunham, D., Timerson, B., Hanuš, J., Frappa, E., Talbot, J., Hayamizu, T., Warner, B.D., Pilcher, F., Galád, A., 2011. Combining asteroid models derived by lightcurve inversion with asteroidal occultation silhouettes. *Icarus* 214, 652–670. 1104. 4227.

Đurech, J., Scheirich, P., Kaasalainen, M., Grav, T., Jedicke, R., Denneau, L., 2007. Physical models of asteroids from sparse photometric data, in: G. B. Valsecchi, D. Vokrouhlický, & A. Milani (Ed.), *IAU Symposium*, pp. 191–200.

Đurech, J., Sidorin, V., Kaasalainen, M., 2010. DAMIT: a database of asteroid models. *Astronomy and Astrophysics* 513, A46.

Đurech, J., Vokrouhlický, D., Pravec, P., Hanuš, J., Farnocchia, D., Krugly, Y.N., Inasaridze, R.Y., Ayyazian, V.R., Fatka, P., Chiorny, V.G., Gaftonyuk, N., Galád, A., Groom, R., Hornoch, K., Kučáková, H., Kušnirák, P., Lehký, M., Kvaratskhelia, O.I., Masi, G., Molotov, I.E., Oey, J., Pollock, J.T., Shevchenko, V.G., Vraštil, J., Warner, B.D., 2018. YORP and Yarkovsky effects in asteroids (1685) Toro, (2100) Ra-Shalom, (3103) Eger, and (161989) Cacus. *Astronomy and Astrophysics* 609, A86. 1711. 05987.

Dykhuis, M.J., Molnar, L.A., Gates, C.J., Gonzales, J.A., Huffman, J.J., Maat, A.R., Maat, S.L., Marks, M.I., Massey-Plantinga, A.R., McReynolds, N.D., Schut, J.A., Stoep, J.P., Stutzman, A.J., Thomas, B.C., Vander Tuig, G.W., Vriesema, J.W., Greenberg, R., 2016. Efficient spin sense determination of Flora-region asteroids via the epoch method. *Icarus* 267, 174–203.

Emery, J.P., Fernández, Y.R., Kelley, M.S.P., Warden (née Crane), K.T., Hergenrother, C., Lauretta, D.S., Drake, M.J., Campins, H., Ziffer, J., 2014. Thermal infrared observations and thermophysical characterization of OSIRIS-REx target asteroid (101955) Bennu. *Icarus* 234, 17–35.

Emery, J.P., Sprague, A.L., Witteborn, F.C., Colwell, J.E., Kozlowski, R.W.H., Wooden, D.H., 1998. Mercury: Thermal Modeling and Mid-infrared (5–12 μm) Observations. *Icarus* 136, 104–123.

Fernández, Y.R., Jewitt, D.C., Sheppard, S.S., 2002. Thermal Properties of Centaurs Asbolus and Chiron. *Astronomical Journal* 123, 1050–1055. astro-ph/0111395.

Fernández, Y.R., Sheppard, S.S., Jewitt, D.C., 2003. The Albedo Distribution

- of Jovian Trojan Asteroids. *Astronomical Journal* 126, 1563–1574.
- Fornasier, S., Lellouch, E., Müller, T., Santos-Sanz, P., Panuzzo, P., Kiss, C., Lim, T., Mommert, M., Bockelée-Morvan, D., Vilenius, E., Stansberry, J., Tozzi, G.P., Mottola, S., Delsanti, A., Crovisier, J., Duffard, R., Henry, F., Lacerda, P., Barucci, A., Gicquel, A., 2013. TNOs are Cool: A survey of the trans-Neptunian region. VIII. Combined Herschel PACS and SPIRE observations of nine bright targets at 70–500 μm . *Astronomy and Astrophysics* 555, A15. 1305.0449.
- Grav, T., Mainzer, A.K., Bauer, J., Masiero, J., Spahr, T., McMillan, R.S., Walker, R., Cutri, R., Wright, E., Eisenhardt, P.R., Blauvelt, E., DeBaun, E., Elsbury, D., Gautier, T., Gomillion, S., Hand, E., Wilkins, A., 2012. WISE/NEOWISE Observations of the Hilda Population: Preliminary Results. *Astrophysical Journal* 744, 197. 1110.0283.
- Groussin, O., Lamy, P., Jorda, L., 2004. Properties of the nuclei of Centaurs Chiron and Chariklo. *Astronomy and Astrophysics* 413, 1163–1175.
- Gundlach, B., Blum, J., 2013. A new method to determine the grain size of planetary regolith. *Icarus* 223, 479–492. 1212.3108.
- Hanuš, J., Brož, M., Ďurech, J., Warner, B.D., Brinsfield, J., Durkee, R., Higgins, D., Koff, R.A., Oey, J., Pilcher, F., Stephens, R., Strabla, L.P., Ullisse, Q., Girelli, R., 2013a. An anisotropic distribution of spin vectors in asteroid families. *Astronomy and Astrophysics* 559, A134. 1309.4296.
- Hanuš, J., Delbo', M., Alí-Lagoa, V., Bolin, B., Jedicke, R., Ďurech, J., Cibulková, H., Pravec, P., Kušnirák, P., Behrend, R., Marchis, F., Antonini, P., Arnold, L., Audejean, M., Bachschmidt, M., Bernasconi, L., Brunetto, L., Casulli, S., Dymock, R., Esseiva, N., Esteban, M., Gerteis, O., de Groot, H., Gully, H., Hamanowa, H., Hamanowa, H., Krafft, P., Lehký, M., Manzini, F., Michelet, J., Morelle, E., Oey, J., Pilcher, F., Reigier, F., Roy, R., Salom, P.A., Warner, B.D., 2018. Spin states of asteroids in the Eos collisional family. *Icarus* 299, 84–96. 1707.05507.
- Hanuš, J., Delbo', M., Ďurech, J., Alí-Lagoa, V., 2015. Thermophysical modeling of asteroids from WISE thermal infrared data - Significance of the shape model and the pole orientation uncertainties. *Icarus* 256, 101–116. 1504.04199.
- Hanuš, J., Delbo', M., Vokrouhlický, D., Pravec, P., Emery, J.P., Alí-Lagoa, V., Bolin, B., Devogèle, M., Dyvig, R., Galád, A., Jedicke, R., Kornoš, L., Kušnirák, P., Licandro, J., Reddy, V., Rivet, J.P., Világi, J., Warner, B.D., 2016a. Near-Earth asteroid (3200) Phaethon: Characterization of its orbit, spin state, and thermophysical parameters. *Astronomy and Astrophysics* 592, A34. 1605.05205.
- Hanuš, J., Ďurech, J., Brož, M., Marciniak, A., Warner, B.D., Pilcher, F., Stephens, R., Behrend, R., Carry, B., Čapek, D., Antonini, P., Audejean, M., Augustesen, K., Barbotin, E., Baudouin, P., Bayol, A., Bernasconi, L., Borczyk, W., Bosch, J.G., Brochard, E., Brunetto, L., Casulli, S., Cazenave, A., Charbonnel, S., Christophe, B., Colas, F., Coloma, J., Conjat, M., Cooney, W., Correira, H., Cotrez, V., Coupier, A., Crippa, R., Cristofanelli, M., Dalmas, C., Danavaro, C., Demeautis, C., Droege, T., Durkee, R., Esseiva, N., Esteban, M., Fagas, M., Farroni, G., Fauvaud, M., Fauvaud, S., Del Frio, F., Garcia, L., Geier, S., Godon, C., Grangeon, K., Hamanowa, H., Hamanowa, H., Heck, N., Hellmich, S., Higgins, D., Hirsch, R., Husarik, M., Itkonen, T., Jade, O., Kamiński, K., Kankiewicz, P., Klotz, A., Koff, R.A., Kryszczyńska, A., Kwiatkowski, T., Lafont, A., Leroy, A., Lecacheux, J., Leonie, Y., Leyrat, C., Manzini, F., Martin, A., Masi, G., Matter, D., Michałowski, J., Michałowski, M.J., Michałowski, T., Michelet, J., Michelsen, R., Morelle, E., Mottola, S., Naves, R., Nomen, J., Oey, J., Ogloza, W., Oksanen, A., Oszkiewicz, D., Pääkkönen, P., Paiella, M., Pallares, H., Paulo, J., Pavic, M., Payet, B., Polińska, M., Polishook, D., Poncy, R., Revaz, Y., Rinner, C., Rocca, M., Roche, A., Romeuf, D., Roy, R., Saguin, H., Salom, P.A., Sanchez, S., Santacana, G., Santana-Ros, T., Sareyan, J.P., Sobkowiak, K., Sposetti, S., Starkey, D., Stoss, R., Strajnic, J., Teng, J.P., Trégon, B., Vagnozzi, A., Velichko, F.P., Waelchli, N., Wagerz, K., Wücher, H., 2013b. Asteroids' physical models from combined dense and sparse photometry and scaling of the YORP effect by the observed obliquity distribution. *Astronomy and Astrophysics* 551, A67. 1301.6943.
- Hanuš, J., Ďurech, J., Brož, M., Warner, B.D., Pilcher, F., Stephens, R., Oey, J., Bernasconi, L., Casulli, S., Behrend, R., Polishook, D., Henych, T., Lehký, M., Yoshida, F., Ito, T., 2011. A study of asteroid pole-latitude distribution based on an extended set of shape models derived by the lightcurve inversion method. *Astronomy and Astrophysics* 530, A134. 1104.4114.
- Hanuš, J., Ďurech, J., Oszkiewicz, D.A., Behrend, R., Carry, B., Delbo, M., Adam, O., Afonina, V., Anquetin, R., Antonini, P., Arnold, L., Audejean, M., Aurard, P., Bachschmidt, M., Baduel, B., Barbotin, E., Barroy, P., Baudouin, P., Berard, L., Berger, N., Bernasconi, L., Bosch, J.G., Bouley, S., Bozhinova, I., Brinsfield, J., Brunetto, L., Canaud, G., Caron, J., Carrier, F., Casalnuovo, G., Casulli, S., Cerda, M., Chalamet, L., Charbonnel, S., Chinaglia, B., Cikota, A., Colas, F., Coliac, J.F., Collet, A., Coloma, J., Conjat, M., Conseil, E., Costa, R., Crippa, R., Cristofanelli, M., Damerdjji, Y., Debackère, A., Decock, A., Déhais, Q., Déléage, T., Delmelle, S., Demeautis, C., Drózd, M., Dubos, G., Dulcamara, T., Dumont, M., Durkee, R., Dymock, R., Escalante del Valle, A., Esseiva, N., Esseiva, R., Esteban, M., Faucher, T., Fauerbach, M., Fauvaud, M., Fauvaud, S., Forné, E., Fournel, C., Fradet, D., Garlitz, J., Gerteis, O., Gillier, C., Gillon, M., Giraud, R., Godard, J.P., Goncalves, R., Hamanowa, H., Hamanowa, H., Hay, K., Hellmich, S., Heterier, S., Higgins, D., Hirsch, R., Hodosan, G., Hren, M., Hygate, A., Innocent, N., Jacquinet, H., Jawahar, S., Jehin, E., Jerosimic, L., Klotz, A., Koff, W., Korlevic, P., Kosturkiewicz, E., Krafft, P., Krugly, Y., Kugel, F., Labrevoir, O., Lecacheux, J., Lehký, M., Leroy, A., Lesquerbault, B., Lopez-Gonzales, M.J., Lutz, M., Mallecot, B., Manfroid, J., Manzini, F., Marciniak, A., Martin, A., Modave, B., Montaigut, R., Montier, J., Morelle, E., Morton, B., Mottola, S., Naves, R., Nomen, J., Oey, J., Ogloza, W., Paiella, M., Pallares, H., Peyrot, A., Pilcher, F., Pirenne, J.F., Piron, P., Polińska, M., Polotto, M., Poncy, R., Previt, J.P., Reigier, F., Renauld, D., Ricci, D., Richard, F., Rinner, C., Risoldi, V., Robilliard, D., Romeuf, D., Rousseau, G., Roy, R., Ruthroff, J., Salom, P.A., Salvador, L., Sanchez, S., Santana-Ros, T., Scholz, A., Séné, G., Skiff, B., Sobkowiak, K., Sogorb, P., Soldán, F., Spiridakis, A., Splanska, E., Sposetti, S., Starkey, D., Stephens, R., Stiepen, A., Stoss, R., Strajnic, J., Teng, J.P., Tumolo, G., Vagnozzi, A., Vanoutryve, B., Vugnon, J.M., Warner, B.D., Waucomont, M., Wertz, O., Winiarski, M., Wolf, M., 2016b. New and updated convex shape models of asteroids based on optical data from a large collaboration network. *Astronomy and Astrophysics* 586, A108. 1510.07422.
- Hapke, B., 1984. Bidirectional reflectance spectroscopy. III - Correction for macroscopic roughness. *Icarus* 59, 41–59.
- Harris, A.W., Lagerros, J.S.V., 2002. Asteroids in the Thermal Infrared. *Asteroids III*, 205–218.
- Higgins, D.J., 2005. Lightcurve periods for 1701 Okavango, 689 Zita, 981 Martina and (14653) 1998 YV11. *Minor Planet Bulletin* 32, 13–14.
- Horner, J., Müller, T.G., Lykawka, P.S., 2012. (1173) Anchises - thermophysical and dynamical studies of a dynamically unstable Jovian Trojan. *Monthly Notices of the Royal Astronomical Society* 423, 2587–2596. 1204.1388.
- Kaasalainen, M., Lamberg, L., 2006. Inverse problems of generalized projection operators. *Inverse Problems* 22, 749–769.
- Kaasalainen, M., Torppa, J., 2001. Optimization Methods for Asteroid Lightcurve Inversion. I. Shape Determination. *Icarus* 153, 24–36.
- Kaasalainen, M., Torppa, J., Muinonen, K., 2001. Optimization Methods for Asteroid Lightcurve Inversion. II. The Complete Inverse Problem. *Icarus* 153, 37–51.
- Keihm, S.J., 1984. Interpretation of the lunar microwave brightness temperature spectrum - Feasibility of orbital heat flow mapping. *Icarus* 60, 568–589.
- Koren, S.C., Wright, E.L., Mainzer, A., 2015. Characterizing asteroids multiply-observed at infrared wavelengths. *Icarus* 258, 82–91. 1506.04751.
- Lagerros, J.S.V., 1996. Thermal physics of asteroids. I. Effects of shape, heat conduction and beaming. *Astronomy and Astrophysics* 310, 1011–1020.
- Lagerros, J.S.V., 1997. Thermal physics of asteroids. III. Irregular shapes and albedo variegations. *Astronomy and Astrophysics* 325, 1226–1236.
- Lagerros, J.S.V., 1998. Thermal physics of asteroids. IV. Thermal infrared beaming. *Astronomy and Astrophysics* 332, 1123–1132.
- Lamy, P.L., Jorda, L., Fornasier, S., Groussin, O., Barucci, M.A., Carvano, J., Dotto, E., Fulchignoni, M., Toth, I., 2008. Asteroid 2867 Steins. III. Spitzer Space Telescope observations, size determination, and thermal properties. *Astronomy and Astrophysics* 487, 1187–1193.
- Larson, S., Beshore, E., Hill, R., Christensen, E., McLean, D., Kolar, S., McNaught, R., Garradd, G., 2003. The CSS and SSS NEO surveys, in: *AAS/Division for Planetary Sciences Meeting Abstracts #35*, p. 982.
- Lauretta, D.S., Bartels, A.E., Barucci, M.A., Bierhaus, E.B., Binzel, R.P., Botke, W.F., Campins, H., Chesley, S.R., Clark, B.C., Clark, B.E., Cloutis, E.A., Connolly, H.C., Crombie, M.K., Delbó, M., Dworkin, J.P., Emery, J.P., Glavin, D.P., Hamilton, V.E., Hergenrother, C.W., Johnson, C.L., Keller, L.P., Michel, P., Nolan, M.C., Sandford, S.A., Scheeres, D.J., Simon, A.A., Sutter, B.M., Vokrouhlický, D., Walsh, K.J., 2015. The OSIRIS-REX target asteroid (101955) Bennu: Constraints on its physical, geological, and dynamical nature from astronomical observations. *Meteoritics and Planetary*

- Science 50, 834–849.
- Lellouch, E., Santos-Sanz, P., Lacerda, P., Mommert, M., Duffard, R., Ortiz, J.L., Müller, T.G., Fornasier, S., Stansberry, J., Kiss, C., Vilnius, E., Mueller, M., Peixinho, N., Moreno, R., Groussin, O., Delsanti, A., Harris, A.W., 2013. "TNOs are Cool": A survey of the trans-Neptunian region. IX. Thermal properties of Kuiper belt objects and Centaurs from combined Herschel and Spitzer observations. *Astronomy and Astrophysics* 557, A60.
- Leyrat, C., Barucci, A., Mueller, T., O'Rourke, L., Valtchanov, I., Fornasier, S., 2012. Thermal properties of (4) Vesta derived from Herschel measurements. *Astronomy and Astrophysics* 539, A154.
- Leyrat, C., Coradini, A., Erard, S., Capaccioni, F., Capria, M.T., Drossart, P., de Sanctis, M.C., Tosi, F., Virtis Team, 2011. Thermal properties of the asteroid (2867) Steins as observed by VIRTIS/Rosetta. *Astronomy and Astrophysics* 531, A168.
- Lim, L.F., Emery, J.P., Moskovitz, N.A., 2011. Mineralogy and thermal properties of V-type Asteroid 956 Elisa: Evidence for diogenitic material from the Spitzer IRS (5–35 μm) spectrum. *Icarus* 213, 510–523.
- Lim, L.F., McConnochie, T.H., Bell, J.F., Hayward, T.L., 2005. Thermal infrared (8–13 μm) spectra of 29 asteroids: the Cornell Mid-Infrared Asteroid Spectroscopy (MIDAS) Survey. *Icarus* 173, 385–408.
- Mainzer, A., Bauer, J., Grav, T., Masiero, J., Cutri, R.M., Dailey, J., Eisenhardt, P., McMillan, R.S., Wright, E., Walker, R., Jedicke, R., Spahr, T., Tholen, D., Alles, R., Beck, R., Brandenburg, H., Conrow, T., Evans, T., Fowler, J., Jarrett, T., Marsh, K., Masci, F., McCallon, H., Wheelock, S., Wittman, M., Wyatt, P., DeBaun, E., Elliott, G., Elsbury, D., Gautier, I.T., Gomillion, S., Leisawitz, D., Maleszewski, C., Micheli, M., Wilkins, A., 2011a. Preliminary Results from NEOWISE: An Enhancement to the Wide-field Infrared Survey Explorer for Solar System Science. *Astrophysical Journal* 731, 53. 1102.1996.
- Mainzer, A., Grav, T., Bauer, J., Conrow, T., Cutri, R.M., Dailey, J., Fowler, J., Giorgini, J., Jarrett, T., Masiero, J., Spahr, T., Statler, T., Wright, E.L., 2015. Survey Simulations of a New Near-Earth Asteroid Detection System. *Astronomical Journal* 149, 172. 1501.01063.
- Mainzer, A., Grav, T., Masiero, J., Bauer, J., Wright, E., Cutri, R.M., McMillan, R.S., Cohen, M., Ressler, M., Eisenhardt, P., 2011b. Thermal Model Calibration for Minor Planets Observed with Wide-field Infrared Survey Explorer/NEOWISE. *Astrophysical Journal* 736, 100.
- Mainzer, A.K., Bauer, J.M., Cutri, R.M., Grav, T., Kramer, E.A., Masiero, J.R., Nugent, C.R., Sonnett, S.M., Stevenson, R.A., Wright, E.L., 2016. NEOWISE Diameters and Albedos V1.0. NASA Planetary Data System 247.
- Marchis, F., Enriquez, J.E., Emery, J.P., Mueller, M., Baek, M., Pollock, J., Assafin, M., Vieira Martins, R., Berthier, J., Vachier, F., Cruikshank, D.P., Lim, L.F., Reichart, D.E., Ivarsen, K.M., Haislip, J.B., LaCluyze, A.P., 2012. Multiple asteroid systems: Dimensions and thermal properties from Spitzer Space Telescope and ground-based observations. *Icarus* 221, 1130–1161.
- Marciniak, A., Bartczak, P., Santana-Ros, T., Michałowski, T., Antonini, P., Behrend, R., Bembrick, C., Bernasconi, L., Borczyk, W., Colas, F., Coloma, J., Crippa, R., Esseiva, N., Fagas, M., Fauvaud, M., Fauvaud, S., Ferreira, D.D.M., Hein Bertelsen, R.P., Higgins, D., Hirsch, R., Kąjawa, J.J.E., Kamiński, K., Kryszczyńska, A., Kwiatkowski, T., Manzini, F., Michałowski, J., Michałowski, M.J., Paschke, A., Polińska, M., Poncy, R., Roy, R., Santacana, G., Sobkowiak, K., Stasik, M., Starczewski, S., Velichko, F., Wucher, H., Zafar, T., 2012. Photometry and models of selected main belt asteroids. IX. Introducing interactive service for asteroid models (ISAM). *Astronomy and Astrophysics* 545, A131.
- Marciniak, A., Michałowski, T., Hirsch, R., Behrend, R., Bernasconi, L., Descamps, P., Colas, F., Sobkowiak, K., Kamiński, K., Kryszczyńska, A., Kwiatkowski, T., Polińska, M., Rudawska, R., Fauvaud, S., Santacana, G., Bruno, A., Fauvaud, M., Teng-Chuen-Yu, J.P., Peyrot, A., 2009. Photometry and models of selected main belt asteroids. VII. 350 Ornamenta, 771 Libera, and 984 Gretia. *Astronomy and Astrophysics* 508, 1503–1507.
- Marciniak, A., Michałowski, T., Kaasalainen, M., Kryszczyńska, A., Kwiatkowski, T., Hirsch, R., Kamiński, K., Fagas, M., Polińska, M., Velichko, F.P., Michałowski, M.J., Snodgrass, C., Behrend, R., Bernasconi, L., 2008. Photometry and models of selected main belt asteroids. V. 73 Klytia, 377 Campania, and 378 Holmia. *Astronomy and Astrophysics* 478, 559–565.
- Masiero, J.R., Mainzer, A.K., Grav, T., Bauer, J.M., Cutri, R.M., Dailey, J., Eisenhardt, P.R.M., McMillan, R.S., Spahr, T.B., Skrutskie, M.F., Tholen, D., Walker, R.G., Wright, E.L., DeBaun, E., Elsbury, D., Gautier, I.T., Gomillion, S., Wilkins, A., 2011. Main Belt Asteroids with WISE/NEOWISE. I. Preliminary Albedos and Diameters. *Astrophysical Journal* 741, 68. 1109.4096.
- Matter, A., Delbo', M., Carry, B., Ligi, S., 2013. Evidence of a metal-rich surface for the Asteroid (16) Psyche from interferometric observations in the thermal infrared. *Icarus* 226, 419–427. 1306.2455.
- Matter, A., Delbo', M., Ligi, S., Crouzet, N., Tanga, P., 2011. Determination of physical properties of the Asteroid (41) Daphne from interferometric observations in the thermal infrared. *Icarus* 215, 47–56. 1108.2616.
- Mueller, M., 2012. Surface Properties of Asteroids from Mid-Infrared Observations and Thermophysical Modeling. ArXiv e-prints 1208.3993.
- Mueller, M., Harris, A.W., Bus, S.J., Hora, J.L., Kassis, M., Adams, J.D., 2006. The size and albedo of Rosetta fly-by target 21 Lutetia from new IRTF measurements and thermal modeling. *Astronomy and Astrophysics* 447, 1153–1158.
- Mueller, M., Marchis, F., Emery, J.P., Harris, A.W., Mottola, S., Hestroffer, D., Berthier, J., di Martino, M., 2010. Eclipsing binary Trojan asteroid Patroclus: Thermal inertia from Spitzer observations. *Icarus* 205, 505–515. 0908.4198.
- Mueller, T.G., Lagerros, J.S.V., 1998. Asteroids as far-infrared photometric standards for ISOPHOT. *Astronomy and Astrophysics* 338, 340–352.
- Muinenen, K., Belskaya, I.N., Cellino, A., Delbo', M., Lévasseur-Regourd, A.C., Penttilä, A., Tedesco, E.F., 2010. A three-parameter magnitude phase function for asteroids. *Icarus* 209, 542–555.
- Müller, T.G., Hasegawa, S., Usui, F., 2014a. (25143) Itokawa: The power of radiometric techniques for the interpretation of remote thermal observations in the light of the Hayabusa rendezvous results*. Publications of the Astronomical Society of Japan 66, 52. 1404.5842.
- Müller, T.G., Kiss, C., Scheirich, P., Pravec, P., O'Rourke, L., Vilnius, E., Altieri, B., 2014b. Thermal infrared observations of asteroid (99942) Apophis with Herschel. *Astronomy and Astrophysics* 566, A22. 1404.5847.
- Müller, T.G., Miyata, T., Kiss, C., Gurwell, M.A., Hasegawa, S., Vilnius, E., Sako, S., Kamizuka, T., Nakamura, T., Asano, K., Uchiyama, M., Konishi, M., Yoneda, M., Ootsubo, T., Usui, F., Yoshii, Y., Kidger, M., Altieri, B., Lorente, R., Pál, A., O'Rourke, L., Metcalfe, L., 2013. Physical properties of asteroid 308635 (2005 YU₅₅) derived from multi-instrument infrared observations during a very close Earth approach. *Astronomy and Astrophysics* 558, A97. 1307.7517.
- Müller, T.G., O'Rourke, L., Barucci, A.M., Pál, A., Kiss, C., Zeidler, P., Altieri, B., González-García, B.M., Küppers, M., 2012. Physical properties of OSIRIS-REX target asteroid (101955) 1999 RQ₃₆. Derived from Herschel, VLT/VISIR, and Spitzer observations. *Astronomy and Astrophysics* 548, A36. 1210.5370.
- Müller, T.G., Āurech, J., Ishiguro, M., Mueller, M., Kröhler, T., Yang, H., Kim, M.J., O'Rourke, L., Usui, F., Kiss, C., Altieri, B., Carry, B., Choi, Y.J., Delbo, M., Emery, J.P., Greiner, J., Hasegawa, S., Hora, J.L., Knust, F., Kuroda, D., Osip, D., Rau, A., Rivkin, A., Schady, P., Thomas-Osip, J., Trilling, D., Urakawa, S., Vilnius, E., Weissman, P., Zeidler, P., 2017. Hayabusa-2 mission target asteroid 162173 Ryugu (1999 JU₃): Searching for the object's spin-axis orientation. *Astronomy and Astrophysics* 599, A103. 1611.05625.
- Myhrvold, N., 2017. An empirical examination of WISE/NEOWISE asteroid analysis and results, in: AAS/Division for Planetary Sciences Meeting Abstracts, p. 117.06.
- Nesvorný, D., Brož, M., Carruba, V., 2015. Identification and Dynamical Properties of Asteroid Families. pp. 297–321.
- Oey, J., 2016. Lightcurve Analysis of Asteroids from Blue Mountains Observatory in 2014. *Minor Planet Bulletin* 43, 45–51.
- O'Rourke, L., Müller, T., Valtchanov, I., Altieri, B., González-García, B.M., Bhattacharya, B., Jorda, L., Carry, B., Küppers, M., Groussin, O., Altwegg, K., Barucci, M.A., Bockelee-Morvan, D., Crovisier, J., Dotto, E., Garcia-Lario, P., Kidger, M., Llorente, A., Lorente, R., Marston, A.P., Sanchez Portal, M., Schulz, R., Sierra, M., Teyssier, D., Vavrek, R., 2012. Thermal and shape properties of asteroid (21) Lutetia from Herschel observations around the Rosetta flyby. *Planetary and Space Science* 66, 192–199.
- Oszkiewicz, D.A., Muinenen, K., Bowell, E., Trilling, D., Penttilä, A., Pieniluoma, T., Wasserman, L.H., Enga, M.T., 2011. Online multi-parameter phase-curve fitting and application to a large corpus of asteroid photometric data. *Journal of Quantitative Spectroscopy & Radiative Transfer* 112, 1919–1929.
- Owings, L.E., 2009. Lightcurves for 155 Scylla and 2358 Bahner. *Minor Planet Bulletin* 36, 51–52.

- Pál, A., Kiss, C., Müller, T.G., Santos-Sanz, P., Vilenius, E., Szalai, N., Mommert, M., Lellouch, E., Rengel, M., Hartogh, P., Protopapa, S., Stansberry, J., Ortiz, J.L., Duffard, R., Thirouin, A., Henry, F., Delsanti, A., 2012. "TNOs are Cool": A survey of the trans-Neptunian region. VII. Size and surface characteristics of (90377) Sedna and 2010 EK₁₃₉. *Astronomy and Astrophysics* 541, L6. 1204.0899.
- Pilcher, F., 2014. Rotation Period Determinations for 24 Themis, 65 Cybele 108 Hecuba, 530 Turandot, and 749 Malzovia. *Minor Planet Bulletin* 41, 250–252.
- Pilcher, F., Jardine, D., 2009. Period Determinations for 31 Euphrosyne, 35 Leukothea 56 Melete, 137 Meliboea, 155 Scylla, and 264 Libussa. *Minor Planet Bulletin* 36, 52–54.
- Press, W.H., Flannery, B.P., Teukolsky, S.A., 1986. Numerical recipes. The art of scientific computing. Cambridge: University Press, 1986.
- Rozitis, B., 2017. The surface roughness of (433) Eros as measured by thermal-infrared beaming. *Monthly Notices of the Royal Astronomical Society* 464, 915–923.
- Rozitis, B., Duddy, S.R., Green, S.F., Lowry, S.C., 2013. A thermophysical analysis of the (1862) Apollo Yarkovsky and YORP effects. *Astronomy and Astrophysics* 555, A20.
- Rozitis, B., Green, S.F., 2011. Directional characteristics of thermal-infrared beaming from atmosphereless planetary surfaces - a new thermophysical model. *Monthly Notices of the Royal Astronomical Society* 415, 2042–2062.
- Rozitis, B., Green, S.F., 2014. Physical characterisation of near-Earth asteroid (1620) Geographos. Reconciling radar and thermal-infrared observations. *Astronomy and Astrophysics* 568, A43. 1407.2127.
- Rozitis, B., MacLennan, E., Emery, J.P., 2014. Cohesive forces prevent the rotational breakup of rubble-pile asteroid (29075) 1950 da. *Nature* 512, 174–176.
- Spencer, J.R., 1990. A rough-surface thermophysical model for airless planets. *Icarus* 83, 27–38.
- Spencer, J.R., Lebofsky, L.A., Sykes, M.V., 1989. Systematic biases in radiometric diameter determinations. *Icarus* 78, 337–354.
- Stephens, R.D., 2014a. Asteroids Observed from CS3: 2013 October–December. *Minor Planet Bulletin* 41, 92–95.
- Stephens, R.D., 2014b. Asteroids Observed from CS3: 2014 January - March. *Minor Planet Bulletin* 41, 171–175.
- Tedesco, E.F., Noah, P.V., Noah, M., Price, S.D., 2002. The Supplemental IRAS Minor Planet Survey. *Astronomical Journal* 123, 1056–1085.
- Tedesco, E.F., Noah, P.V., Noah, M., Price, S.D., 2004. IRAS Minor Planet Survey V6.0. NASA Planetary Data System 12.
- Tholen, D.J., 1984. Asteroid taxonomy from cluster analysis of Photometry. Ph.D. thesis. Arizona Univ., Tucson.
- Tholen, D.J., 1989. Asteroid taxonomic classifications, in: Binzel, R.P., Gehrels, T., Matthews, M.S. (Eds.), *Asteroids II*, University of Arizona Press. pp. 1139–1150.
- Torppa, J., Kaasalainen, M., Michałowski, T., Kwiatkowski, T., Kryszczyńska, A., Denchev, P., Kowalski, R., 2003. Shapes and rotational properties of thirty asteroids from photometric data. *Icarus* 164, 346–383.
- Usui, F., Hasegawa, S., Ishiguro, M., Müller, T.G., Ootsubo, T., 2014. A comparative study of infrared asteroid surveys: IRAS, AKARI, and WISE. *Publications of the Astronomical Society of Japan* 66, 56. 1403.7854.
- Vernazza, P., Delbo', M., King, P.L., Izawa, M.R.M., Olofsson, J., Lamy, P., Cipriani, F., Binzel, R.P., Marchis, F., Merin, B., Tamanai, A., 2012. High surface porosity as the origin of emissivity features in asteroid spectra. *Icarus* 221, 1162–1172.
- Vokrouhlický, D., Bottke, W.F., Chesley, S.R., Scheeres, D.J., Statler, T.S., 2015. The Yarkovsky and YORP Effects. pp. 509–531.
- Warner, B.D., 2009. Asteroid Lightcurve Analysis at the Palmer Divide Observatory: 2008 December - 2009 March. *Minor Planet Bulletin* 36, 109–116.
- Warner, B.D., 2010. Asteroid Lightcurve Analysis at the Palmer Divide Observatory: 2010 March - June. *Minor Planet Bulletin* 37, 161–165.
- Warner, B.D., 2011. Upon Further Review: V. An Examination of Previous Lightcurve Analysis from the Palmer Divide Observatory. *Minor Planet Bulletin* 38, 63–65.
- Warner, B.D., 2012. Asteroid Lightcurve Analysis at the Palmer Divide Observatory: 2011 September - December. *Minor Planet Bulletin* 39, 69–80.
- Warner, B.D., 2014. Asteroid Lightcurve Analysis at CS3-Palmer Divide Station: 2013 June- September. *Minor Planet Bulletin* 41, 27–32.
- Warner, B.D., 2015. Asteroid Lightcurve Analysis at CS3-Palmer Divide Station: 2015 March-June. *Minor Planet Bulletin* 42, 267–276.
- Warner, B.D., Stephens, R.D., Harris, A.W., 2011. Save the Lightcurves. *Minor Planet Bulletin* 38, 172–174.
- Weidenschilling, S.J., Chapman, C.R., Davis, D.R., Greenberg, R., Levy, D.H., 1990. Photometric geodesy of main-belt asteroids. III - Additional lightcurves. *Icarus* 86, 402–447.
- Wolters, S.D., Rozitis, B., Duddy, S.R., Lowry, S.C., Green, S.F., Snodgrass, C., Hainaut, O.R., Weissman, P., 2011. Physical characterization of low delta-V asteroid (175706) 1996 FG3. *Monthly Notices of the Royal Astronomical Society* 418, 1246–1257.
- Wright, E.L., Eisenhardt, P.R.M., Mainzer, A.K., Ressler, M.E., Cutri, R.M., Jarrett, T., Kirkpatrick, J.D., Padgett, D., McMillan, R.S., Skrutskie, M., Stanford, S.A., Cohen, M., Walker, R.G., Mather, J.C., Leisawitz, D., Gautier, I.T.N., McLean, I., Benford, D., Lonsdale, C.J., Blain, A., Mendez, B., Irace, W.R., Duval, V., Liu, F., Royer, D., Heinrichsen, I., Howard, J., Shannon, M., Kendall, M., Walsh, A.L., Larsen, M., Cardon, J.G., Schick, S., Schwalm, M., Abid, M., Fabinsky, B., Naes, L., Tsai, C.W., 2010. The Wide-field Infrared Survey Explorer (WISE): Mission Description and Initial On-orbit Performance. *Astronomical Journal* 140, 1868–1881. 1008.0031.
- Zappalà, V., Cellino, A., Farinella, P., Knežević, Z., 1990. Asteroid families. I - Identification by hierarchical clustering and reliability assessment. *Astronomical Journal* 100, 2030–2046.
- Zappalà, V., Cellino, A., Farinella, P., Milani, A., 1994. Asteroid families. 2: Extension to unnumbered multiopposition asteroids. *Astronomical Journal* 107, 772–801.

Appendix A. Tables

Table A.2: Compilation of previously published values of thermophysical properties (size D , thermal inertia Γ , geometric visible albedo p_V), taxonomical class, heliocentric distance r_h of the object when the thermal infrared data used for the thermal inertia determination were obtained, rotation period P , and references to the publications. The taxonomical classes are either adopted directly from the publications, or based on the SMASS II (Bus and Binzel 2002) or the Tholen (Tholen 1984, 1989) taxonomy.

Asteroid	D [km]	Γ [J m ⁻² s ^{-1/2} K ⁻¹]	p_V	Tax	r_h [au]	P [h]	Reference
1 Ceres	923±20	10±10	0.113±0.005	C	2.8	8.95	Mueller and Lagerros (1998)
2 Pallas	544±43	10±10	0.14±0.02	B	2.8	7.81	Mueller and Lagerros (1998)
3 Juno	234±11	5±5	0.24±0.03	S	2.7	7.21	Mueller and Lagerros (1998)
4 Vesta	525±1	20±15	0.34±0.01	V	2.3	5.34	Leyrat et al. (2012)
16 Psyche	244±25	125±40	0.12±0.02	M	2.7	4.20	Matter et al. (2013)
21 Lutetia	96±1	5±5	0.20±0.01	M	2.8	8.17	O'Rourke et al. (2012)
22 Kalliope	167±17	125±125	0.17±0.03	M	2.3	4.15	Marchis et al. (2012)
32 Pomona	85±1	70±50	0.23±0.01	S	2.8	9.45	Delbo' and Tanga (2009)
41 Daphne	202±7	25±25	0.064±0.007	Ch	2.1	5.99	Matter et al. (2011)
44 Nysa	81±1	120±40	0.41±0.01	E	2.5	6.42	Delbo' and Tanga (2009)
45 Eugenia	198±20	45±45	0.046±0.01	C	2.6	5.70	Marchis et al. (2012)
87 Sylvia	300±30	70±60	0.030±0.007	P	2.7	5.18	Marchis et al. (2012)
107 Camilla	245±25	25±10	0.043±0.009	P	3.2	4.84	Marchis et al. (2012)
110 Lydia	94±4	135±65	0.15±0.01	M	2.9	10.93	Delbo' and Tanga (2009)
115 Thyra	92±2	62±38	0.21±0.01	S	2.5	7.24	Delbo' and Tanga (2009)
121 Hermione	220±22	30±25	0.043±0.009	Ch	2.9	5.55	Marchis et al. (2012)
130 Elektra	197±20	30±30	0.064±0.013	Ch	2.9	5.22	Marchis et al. (2012)
277 Elvira	38±2	250±150	0.15±0.02	S	2.6	29.69	Delbo' and Tanga (2009)
283 Emma	135±14	105±100	0.032±0.007	P	2.6	6.90	Marchis et al. (2012)
306 Unitas	56±1	180±80	0.145±0.005	S	2.2	8.74	Delbo' and Tanga (2009)
382 Dodona	75±1	80±65	0.100±0.005	M	2.6	4.11	Delbo' and Tanga (2009)
433 Eros	18±1	150±50	0.29±0.02	S	1.6	5.27	Mueller (2012)
532 Herculina	203±14	10±10	0.20±0.04	S	2.8	9.40	Mueller and Lagerros (1998)
617 Patroclus	106±11	20±15	0.045±0.009	P	5.9	102.80	Mueller et al. (2010)
624 Hektor	170±20	5±5	0.063±0.012	D	5.3	6.92	Hanuš et al. (2015)
694 Ekard	110±2	120±20	0.031±0.005	S	1.8	5.93	Delbo' and Tanga (2009)
720 Bohlinia	41±1	135±65	0.135±0.005	S	2.9	8.92	Delbo' and Tanga (2009)
771 Libera	33±3	90±60	0.14±0.03	X	2.8	5.89	Hanuš et al. (2015)
956 Elisa	10.4±0.8	90±60	0.14±0.02	S	1.8	16.49	Lim et al. (2011)
1036 Ganymed	36±3	54±46	0.26±0.04	S	3.9	10.30	Hanuš et al. (2015)
1173 Anchises	136±15	62±37	0.027±0.006	P	5.0	11.60	Homer et al. (2012)
1472 Muonio	9.1±0.2	44±45	0.24±0.07	S	2.7	8.71	Hanuš et al. (2015)
1580 Betulia	4.6±0.5	180±50	0.077±0.015	C	1.1	6.13	Mueller (2012)
1620 Geographos	5.0±0.1	340±120	0.168±0.017	S	1.1	5.22	Rozitis and Green (2014)
1627 Ivar	7.7±0.6	140±80	0.258±0.017	S	2.1	4.80	Hanuš et al. (2015)
1685 Toro	3.5±0.4	260±130	0.26±0.05	Sv	1.9	10.20	Đurech et al. (2018)
1862 Apollo	1.55±0.07	140±100	0.20±0.02	Q	1.0	3.07	Rozitis et al. (2013)
1980 Tezcatlipoca	5.1±0.1	310±300	0.25±0.10	Sl	2.3	7.25	Hanuš et al. (2015)
2060 Chiron	142±10	4±4	0.11±0.02	B/Cb	12.0	5.92	Groussin et al. (2004)
2060 Chiron	218±20	5±5	0.16±0.03	B/Cb	13.0	5.92	Fornasier et al. (2013)
2363 Cebriones	82±5	7±7	0.060±0.008	D	5.2	20.05	Fernández et al. (2003)
2606 Odesa	18±3	125±75	0.12±0.05	X	3.5	8.24	Hanuš et al. (2015)
2867 Steins	4.9±0.4	150±60	0.27±0.04	E	2.1	6.05	Lamy et al. (2008)
2867 Steins	5.2±1.0	210±30	0.22±0.10	E	2.1	6.05	Leyrat et al. (2011)
3063 Makhaon	116±4	15±15	0.048±0.004	D	4.7	8.64	Fernández et al. (2003)
3200 Phaethon	5.1±0.2	600±200	0.122±0.008	B	1.1	3.60	Hanuš et al. (2016a)
8405 Asbolus	66±4	5±5	0.12±0.03	S	7.9	8.94	Fernández et al. (2002)
10199 Chariklo	236±12	1±1	0.07±0.01	D	13.0	7.00	Groussin et al. (2004)
25143 Itokawa	0.32±0.03	700±100	0.19±0.07	S	1.1	12.13	Mueller (2012)
25143 Itokawa	0.32±0.03	700±200	0.29±0.02	S	1.1	12.13	Müller et al. (2014a)
29075 1950_DA	1.30±0.13	24±20	0.20±0.05	M	1.7	2.12	Rozitis et al. (2014)
33342 1998_WT ₂₄	0.35±0.04	200±100	0.56±0.20	E	1.0	3.70	Mueller (2012)
50000 Quaoar	1082±67	6±4	0.12±0.02	S	43.0	17.68	Fornasier et al. (2013)
54509 YORP	0.09±0.01	700±500	0.20±0.02	S	1.1	0.20	Mueller (2012)
55565 2002_AW ₁₉₇	700±50	10±10	0.17±0.03	S	47.0	8.86	Cruikshank et al. (2005)
90377 Sedna	995±80	0.1±0.1	0.32±0.06	S	87.0	10.27	Pál et al. (2012)
90482 Orcus	968±63	1±1	0.23±0.03	S	48.0	13.19	Fornasier et al. (2013)
99942 Apophis	0.38±0.01	600±300	0.30±0.06	Sq	1.1	30.56	Müller et al. (2014b)
101955 Bennu	0.49±0.01	650±300	0.045±0.013	B	1.1	4.30	Müller et al. (2012)
101955 Bennu	0.49±0.02	310±70	0.046±0.005	B	1.1	4.30	Emery et al. (2014)
136108 Haumea	1240±70	0.3±0.2	0.80±0.10	S	51.0	3.92	Lellouch et al. (2013)
161989 Cacus	1.00±0.20	650±150	0.20±0.05	S	1.3	3.75	Đurech et al. (2018)
162173 Ryugu	0.865±0.015	225±75	0.047±0.003	C	1.4	7.63	Müller et al. (2017)
175706 1996_FG ₃	1.7±0.1	120±50	0.046±0.014	C	1.4	3.59	Wolters et al. (2011)
208996 2003_AZ ₈₄	480±20	1.2±0.6	0.11±0.02	S	45.0	13.42	Lellouch et al. (2013)
308635 2005_YU ₅₅	0.31±0.01	575±225	0.065±0.010	C	1.0	19.31	Müller et al. (2013)
341843 2008_EV ₅	0.37±0.01	450±60	0.13±0.05	C	1.0	3.72	Alf-Lagoa et al. (2014)

Table A.3: Thermophysical characteristics of asteroids derived by the VS-TPM. We provide the asteroid number and name, the ecliptic coordinates λ and β of the pole solutions, the sidereal rotational period P , the reference to the shape model, quality flag of the shape model QF , the number of IRAS N_1 , WISE in filters W3 N_{W3} and W4 N_{W4} thermal IR measurements, volume equivalent diameter D , thermal inertia Γ in $\text{J m}^{-2} \text{s}^{-1/2} \text{K}^{-1}$ units, visual geometric albedo p_V , Hapke's mean surface slope $\bar{\theta}$, reduced chi-square of the best fit χ_{red}^2 , heliocentric distance r_{hel} of the thermal infrared observations, absolute magnitude H and slope G (AAMS, Muinonen et al. 2010; Oszkiewicz et al. 2011), taxonomical class, and membership to a collisional family. For the taxonomy, we show the Tholen (T1, Tholen 1984, 1989) and SMASS II (T2, Bus and Binzel 2002) classes.

Asteroid	λ [deg]	β [deg]	P [h]	Reference	QF	N_1	N_{W3}	N_{W4}	D [km]	D_{WISE} [km]	Γ [SI]	p_V	$\bar{\theta}$	χ_{red}^2	r_{hel} [au]	H [mag]	G	T1	T2	Family
73 Klytia	266	68	8.28307	Hanuš et al. (2011)	3	24	9	13	44.1±2.1	44.6±0.9	13±12	0.20±0.02	26.7	1.1	2.8	9.1	0.40	S		
	44	83	8.28307	Hanuš et al. (2011)	3	24	9	13	45.4±1.3	44.6±0.9	15±14	0.18±0.02	12.0	1.3	2.8					
82 Alkmene	164	-28	13.0008	Hanuš et al. (2011)	2	12	10	10	58.6±1.2	57.6±0.7	32±12	0.25±0.03	38.8	1.9	3.3	8.2	0.23	S	Sq	
	349	-33	13.0008	Hanuš et al. (2011)	2	12	10	10	57.9±1.3	57.6±0.7	29±15	0.25±0.03	38.8	2.3	3.3					
99 Dike	233	49	18.1191	Hanuš et al. (2016b)	3	3	7	8	66.5±0.9	67.4±0.4	35±19	0.07±0.03	55.4	2.2	3.2	9.3	0.11	C	Xk	
125 Liberatrix	95	68	3.96820	Đurech et al. (2007)	3	12	14	14	51.1±2.1	48.4±0.5	80±15	0.18±0.02	38.8	2.1	2.9	8.8	0.26	M	X	
	280	74	3.96820	Đurech et al. (2007)	3	12	14	14	50.1±1.3	48.4±0.5	60±15	0.19±0.02	26.7	1.6	2.9					
152 Atala	347	47	6.24472	Hanuš et al. (2011)	1.5		6	14	57.5±1.8	59.0±0.5	0±0	0.22±0.02	16.1	2.0	2.9	8.3	0.39	I	S	
155 Scylla	346	41	7.95878	Revised	2	2	19	19	39.0±0.8	39.6±0.2	30±10	0.05±0.03	48.4	3.2	3.1	10.9	0.09	XFC		
	190	65	7.95878	Pole rejected	2	2	19	19	37.5±1.1	39.6±0.2	20±10	0.05±0.03	26.7	4.4	3.1					
167 Urda	107	-69	13.0613	Đurech et al. (2011)	3	6	21	21	40.8±0.8	39.9±0.3	107±12	0.22±0.02	55.4	6.9	2.8	9.1	0.28	S	Sk	Koronis
	249	-68	13.0613	Đurech et al. (2011)	3	6	21	21	41.5±0.8	39.9±0.3	115±5	0.21±0.03	55.4	5.5	2.8					
188 Menippe	32	48	11.9765	Hanuš et al. (2011)	1.5	21	13	13	35.3±0.9	35.8±0.4	21±13	0.28±0.06	16.1	3.9	3.2	9.2	0.14	S	S	
	198	25	11.9765	Hanuš et al. (2011)	1.5	21	13	13	36.0±1.1	35.8±0.4	13±7	0.27±0.05	16.1	3.8	3.2					
193 Ambrosia	141	-11	6.58167	Hanuš et al. (2013b)	3		8	8	30.8±1.2	26.3±0.2	47±7	0.22±0.04	48.4	2.0	3.3	9.6	0.33		Sk	
	328	-17	6.58167	Hanuš et al. (2013b)	3		8	8	30.1±0.8	26.3±0.2	52±17	0.23±0.02	55.4	1.4	3.3					
220 Stephania	26	-50	18.2087	Hanuš et al. (2013b)	2	6	12	12	29.8±0.5	31.7±0.2	5±5	0.07±0.02	12.0	1.9	2.8	11.1	0.20	XC		
	223	-62	18.2088	Hanuš et al. (2013b)	2	6	12	12	29.8±0.6	31.7±0.2	2±2	0.07±0.02	16.1	1.0	2.8					
226 Weringia	284	-14	11.1485	Hanuš et al. (2016b)	3	7	7	7	28.7±0.2	31.5±0.3	30±10	0.23±0.02	26.7	1.8	3.1	9.8	0.25		S	
263 Dresda	98	53	16.8139	Hanuš et al. (2016b)	3	4	13	12	23.7±1.0	24.0±0.2	25±25	0.23±0.03	3.9	5.5	2.8	10.2	0.27		S	
	272	61	16.8138	Hanuš et al. (2016b)	3	4	13	12	24.0±0.7	24.0±0.2	27±17	0.23±0.05	12.0	7.2	2.8					
272 Antonia	293	-90	3.85480	Hanuš et al. (2013b)	2	9	12	12	30.5±1.1	26.9±0.3	75±10	0.10±0.03	48.4	3.0	2.9	10.5	0.16		X	Hoffmeister
274 Philagoria	328	-71	17.9410	Hanuš et al. (2016b)	2	12	4	4	28.0±0.8	27.3±0.4	95±5	0.24±0.03	55.4	1.1	2.7	9.8	0.17			
	154	-65	17.9410	Hanuš et al. (2016b)	2	12	4	4	28.9±0.9	27.3±0.4	90±10	0.23±0.03	55.4	1.1	2.7					
281 Lucretia	128	-49	4.34971	Hanuš et al. (2013b)	2.5	7	8	8	11.3±0.2	11.0±0.1	45±10	0.24±0.03	27.3	1.2	2.5	11.8	0.32	SU	S	Flora
	309	-61	4.34971	Hanuš et al. (2013b)	2.5	7	8	8	11.1±0.1	11.0±0.1	50±10	0.25±0.03	26.7	1.4	2.5					
290 Bruna	286	-80	13.8055	Hanuš et al. (2013b)	2		26	24	9.8±0.1	9.8±0.1	30±30	0.26±0.02	16.1	2.5	2.3	12.0	0.40			Phocaea
	37	-74	13.8056	Hanuš et al. (2013b)	2		26	24	9.9±0.3	9.8±0.1	12±12	0.26±0.04	12.6	2.3	2.3					
311 Claudia	214	43	7.53138	Hanuš et al. (2011)	3	2	14	14	26.5±0.6	26.3±0.4	24±6	0.24±0.03	16.1	3.8	2.9	9.9	0.25	S		Koronis
	30	40	7.53138	Hanuš et al. (2011)	3	2	14	14	25.8±0.8	26.3±0.4	9±9	0.26±0.02	12.6	3.6	2.9					
340 Eduarda	188	-43	8.00613	Hanuš et al. (2011)	1.5	9	10	10	27.3±0.3	28.0±0.5	30±14	0.24±0.04	26.7	2.2	2.9	9.8	0.27	S		
	18	-47	8.00613	Hanuš et al. (2011)	1.5	9	10	10	27.2±0.4	28.0±0.5	20±20	0.24±0.03	26.7	2.6	2.9					
351 Yrsa	20	-70	13.3120	Hanuš et al. (2013b)	1.5	11	11	11	42.6±0.9	39.7±0.4	52±17	0.23±0.03	38.8	3.8	3.2	9.0	0.22	S		
	193	-41	13.3120	Hanuš et al. (2013b)	1.5	11	11	11	42.3±1.6	39.7±0.4	47±17	0.24±0.03	38.8	2.2	3.2					
352 Gisela	24	-21	7.48008	Hanuš et al. (2013b)	2	6	16	16	24.8±0.6	26.7±0.8	17±17	0.22±0.03	48.4	5.8	2.3	10.2	0.30	S	Sl	Flora
	206	-28	7.48008	Hanuš et al. (2013b)	2	6	16	16	24.3±0.4	26.7±0.8	5±5	0.23±0.03	26.7	8.3	2.3					
355 Gabriella	159	88	4.82899	Marciniak et al. (2012)	3	14	24	24	24.8±0.8	24.0±0.3	35±5	0.23±0.04	26.7	4.4	2.3	10.1	0.29		S	
	341	83	4.82899	Marciniak et al. (2012)	3	14	24	24	24.2±0.7	24.0±0.3	35±5	0.23±0.02	26.7	4.8	2.3					
378 Holmia	130	60	4.44043	Marciniak et al. (2008)	3	7	13	14	28.7±0.7	27.8±0.4	13±12	0.24±0.03	26.7	4.2	2.8	9.8	0.26	S	S	
	286	76	4.44043	Marciniak et al. (2008)	3	7	13	14	29.0±0.6	27.8±0.4	13±12	0.24±0.02	12.6	3.9	2.8					
390 Alma	53	-50	3.74117	Hanuš et al. (2013b)	2	16	14	14	24.3±0.4	25.7±0.2	29±21	0.24±0.03	26.7	3.0	2.4	10.1	0.27	DT		Eunomia
	275	-76	3.74117	Hanuš et al. (2013b)	2	16	14	14	25.3±0.6	25.7±0.2	42±7	0.23±0.04	48.4	4.3	2.4					
394 Arduina	195	-61	16.6217	Hanuš et al. (2016b)	2	5	10	10	30.6±0.6	30.0±0.3	90±10	0.24±0.03	55.4	1.8	2.9	9.6	0.25	S	S	
	55	-79	16.6217	Hanuš et al. (2016b)	2	5	10	10	31.1±1.2	30.0±0.3	77±22	0.23±0.02	55.4	2.0	2.9					
400 Ducrosa	328	56	6.86788	Hanuš et al. (2011)	1.5	12	11	10	34.1±0.5	36.0±0.4	35±10	0.10±0.03	38.8	1.8	3.4	10.4	0.17			
	158	62	6.86789	Hanuš et al. (2011)	1.5	12	11	10	35.2±1.1	36.0±0.4	42±12	0.09±0.03	16.1	1.6	3.4					
413 Edburga	202	-44	15.7715	Hanuš et al. (2011)	1.5	12	26	27	34.6±0.8	34.2±0.2	110±50	0.13±0.02	16.1	6.9	2.9	9.9	0.30	M	X	
430 Hybris	19	-68	7.21655	This work	1	15	9	9	32.9±0.5	31.7±0.7	52±2	0.07±0.03	48.4	1.7	3.5	10.8	0.05			
	188	-79	7.21655	This work	1	15	9	9	33.4±0.8	31.7±0.7	57±7	0.07±0.03	55.4	2.8	3.5					
482 Petrina	280	61	11.79214	Hanuš et al. (2016b)	3	6	12	12	44.2±1.0	45.8±0.3	12±12	0.18±0.02	27.3	1.8	3.3	9.1	0.58	S		
	94	23	11.79210	Hanuš et al. (2016b)	3	6	12	12	44.2±0.6	45.8±0.3	1±1	0.19±0.02	38.8	4.0	3.3					
484 Pittsburghia	70	46	10.64977	Hanuš et al. (2011)	1.5	2	11	11	29.2±0.7	30.1±0.2	6±5	0.20±0.03	16.1	4.7	2.8	9.8	0.39		S	

Table A.3: continued.

Asteroid	λ [deg]	β [deg]	P [h]	Reference	QF	N_1	N_{W3}	N_{W4}	D [km]	D_{WISE} [km]	Γ [SI]	p_V	$\bar{\theta}$	χ^2_{red}	r_{hel} [au]	H [mag]	G	T1	T2	Family				
497 Iva	121	-21	4.62085	Hanuš et al. (2016b)	2		10	10	37.2±0.6	40.9±0.3	72±17	0.14±0.03	12.6	0.9	3.6	9.8	0.15	M						
303	-32	4.62085		Hanuš et al. (2016b)	2		10	10	37.6±0.7	40.9±0.3	67±22	0.14±0.03	16.1	0.8	3.6									
509 Iolanda	248	54	12.2909	Hanuš et al. (2013b)	2	12	20	20	55.7±1.3	51.9±0.7	9±9	0.21±0.02	26.7	5.4	3.3	8.5	0.38	S	S					
90	24	12.2909		Hanuš et al. (2013b)	2	12	20	20	55.2±1.4	51.9±0.7	8±8	0.20±0.02	16.1	5.0	3.3									
512 Taurinensis	324	45	5.58203	Hanuš et al. (2013b)	2	5	13	13	18.0±0.7		4±4	0.23±0.02	12.6	3.0	2.2	10.7	0.31	S	S					
520 Franziska	282	-79	16.5045	Hanuš et al. (2016b)	2	8	8	6	28.9±0.9	25.3±0.2	28±16	0.12±0.02	12.0	1.7	3.3	10.5	0.25	CGU						
114	-45	16.5045		Hanuš et al. (2016b)	2	8	8	6	27.5±1.0	25.3±0.2	38±32	0.12±0.03	55.4	2.0	3.3									
537 Pauly	31	32	16.2961	Hanuš et al. (2016b)	2	8	6	6	41.4±0.9	40.7±0.8	5±5	0.28±0.02	26.7	1.1	3.5	8.8	0.40	DU:						
211	50	16.2961		Hanuš et al. (2016b)	2	8	6	6	42.4±1.0	40.7±0.8	8±8	0.27±0.03	26.7	1.2	3.5									
544 Jetta	21	-71	7.74528	Hanuš et al. (2011)	1.5	9	13	13	26.5±1.2	27.2±0.2	29±11	0.22±0.03	16.1	2.7	3.0	10.0	0.25							
267	-89	7.74528		Hanuš et al. (2011)	1.5	9	13	13	27.5±1.3	27.2±0.2	27±17	0.20±0.02	16.1	2.1	3.0									
550 Senta	63	-40	20.5726	Hanuš et al. (2013a)	1.5	9	23	24	38.2±1.1	37.4±0.2	30±30	0.22±0.02	16.1	3.4	3.1	9.3	0.31	S						
257	-56	20.5727		Hanuš et al. (2013a)	1.5	9	23	24	37.3±0.7	37.4±0.2	22±22	0.23±0.03	26.7	3.2	3.1									
562 Salome	54	55	6.35032	Pole rejected	3	7	22	19	33.9±0.6	32.7±0.1	10±0	0.16±0.02	27.3	5.0	3.2	9.9	0.19	S						
267	43	6.35032		Hanuš et al. (2018)	3	7	22	19	33.4±0.8	32.7±0.1	0±0	0.16±0.02	16.1	2.1	3.2									
573 Recha	76	-26	7.16585	Hanuš et al. (2018)	2	17	12	12	40.1±1.1	47.6±0.5	45±15	0.17±0.02	55.4	2.3	2.7	9.3	0.20			Eos				
590 Tomyris	274	-29	5.55248	Hanuš et al. (2018)	2	10	13	13	31.9±1.2	30.6±0.2	15±15	0.15±0.03	27.3	7.0	3.1	10.0	0.25			Eos				
113	-35	5.55248		Hanuš et al. (2018)	2	10	13	13	32.3±1.2	30.6±0.2	22±22	0.15±0.02	16.1	6.2	3.1									
631 Philippina	183	-2	5.90220	Hanuš et al. (2011)	2	12		20	46.6±3.2	50.5±0.8	0±0	0.24±0.03	48.4	1.1	2.8	8.7	0.35	S	S					
644 Cosima	278	-30	7.55709	Hanuš et al. (2016b)	2.5	2	9	9	19.5±0.4	17.0±0.2	42±17	0.20±0.03	26.7	1.7	3.0	10.8	0.32	S						
99	-29	7.55709		Hanuš et al. (2016b)	2.5	2	9	9	19.3±0.5	17.0±0.2	50±20	0.21±0.03	26.7	1.8	3.0									
669 Kypria	30	39	14.2789	Hanuš et al. (2013b)	1.5	5	12	10	29.8±0.9	29.2±0.4	24±21	0.20±0.04	55.4	3.7	3.2	9.8	0.12	S		Eos				
190	49	14.2789		Hanuš et al. (2013b)	1.5	5	12	10	31.1±1.3	29.2±0.4	45±10	0.19±0.03	48.4	2.8	3.2									
687 Tinette	271	17	7.39710	Hanuš et al. (2016b)	1.5		8	8	22.2±0.5	21.5±0.5	50±15	0.08±0.03	26.7	2.3	3.2	11.5	0.17	X	X					
100	43	7.39710		Hanuš et al. (2016b)	1.5		8	8	21.4±0.7	21.5±0.5	50±15	0.09±0.03	26.7	2.5	3.2									
731 Sorga	83	42	8.18632	Hanuš et al. (2013b)	2	10	13	13	36.9±1.3	34.6±0.4	62±22	0.17±0.02	26.7	2.2	3.3	9.6	0.31	CD	Xe					
274	21	8.18632		Hanuš et al. (2013b)	2	10	13	13	37.4±1.4	34.6±0.4	90±30	0.16±0.02	26.7	2.3	3.3									
749 Malzovia	242	61	5.92748	Revised	2		8	8	12.8±0.4	11.1±0.1	50±15	0.22±0.03	26.7	0.9	2.2	11.5	0.21	S	S					
50	58	5.92748		Revised	2		8	8	13.9±0.5	11.1±0.1	70±30	0.20±0.02	26.7	1.8	2.2									
756 Lilliana	200	31	7.83250	Hanuš et al. (2016b)	3	15	7	7	60.0±0.8	64.8±0.5	11±5	0.06±0.03	26.7	1.5	3.5	9.7	0.06							
53	36	7.83252		Hanuš et al. (2016b)	3	15	7	7	61.8±1.7	64.8±0.5	8±8	0.06±0.03	26.7	1.8	3.5									
757 Portlandia	263	-68	6.58112	Hanuš et al. (2016b)	2	9	11	11	33.1±0.5	32.9±0.2	62±2	0.16±0.03	55.4	3.0	2.5	9.9	0.16	XF	Xk					
89	-55	6.58112		Hanuš et al. (2016b)	2	9	11	11	32.8±0.5	32.9±0.2	52±7	0.16±0.03	48.4	3.7	2.5									
784 Pickeringia	282	35	13.16998	Hanuš et al. (2016b)	1.5	6	9	8	80.0±1.4	75.6±0.3	30±10	0.05±0.03	16.1	1.4	3.7	9.2	0.13			C				
103	67	13.16997		Hanuš et al. (2016b)	1.5	6	9	8	77.5±1.9	75.6±0.3	47±17	0.05±0.03	16.1	2.7	3.7									
787 Moskva	331	59	6.05581	Hanuš et al. (2013b)	3	15	16	15	31.3±0.6	32.0±0.8	37±7	0.20±0.02	27.3	1.7	2.9	9.8	0.37			Maria				
126	27	6.05580		Hanuš et al. (2013b)	3	15	16	15	29.9±0.3	32.0±0.8	10±8	0.22±0.02	12.0	2.3	2.9									
789 Lena	121	56	5.84234	Revised	1		11	9	20.8±1.2	22.5±0.3	20±20	0.12±0.03	16.1	6.4	2.7	11.1	0.19		X					
287	77	5.84234		Revised	1		11	9	22.3±0.4	22.5±0.3	47±7	0.11±0.02	12.0	6.0	2.7									
802 Epyaxa	179	-87	4.39012	Revised	2.5		6	6	7.2±0.5	7.4±0.2	62±7	0.27±0.04	48.4	0.1	2.3	12.6	0.24							
808 Merxia	26	54	30.6297	Hanuš et al. (2011)	1.5	12	13	13	28.6±0.5	30.9±0.2	110±20	0.23±0.02	55.4	1.6	2.9	9.7	0.28		Sq		Merxia			
192	57	30.6297		Hanuš et al. (2011)	1.5	12	13	13	29.3±0.5	30.9±0.2	115±25	0.23±0.02	55.4	1.4	2.9									
810 Atossa	12	67	4.38547	Hanuš et al. (2011)	1		11	11	8.0±0.2	8.1±0.1	65±30	0.24±0.05	48.4	0.9	2.5	12.5	0.29							
188	69	4.38547		Hanuš et al. (2011)	1		11	11	8.1±0.3	8.1±0.1	70±25	0.24±0.05	26.7	1.0	2.5									
816 Juliana	124	-8	10.56272	Hanuš et al. (2013b)	2	24	7	13	48.0±0.7	50.7±0.2	23±17	0.06±0.03	55.4	1.9	2.8	10.2	0.09							
303	9	10.56277		Hanuš et al. (2013b)	2	24	7	13	49.5±0.6	50.7±0.2	3±3	0.05±0.03	38.8	1.9	2.8									
852 Wladilena	181	-48	4.61330	Hanuš et al. (2013b)	3	3	11	11	26.3±0.3	26.5±0.2	45±15	0.21±0.02	48.4	1.3	2.7	10.1	0.39					Phocaea		
46	-53	4.61330		Pole rejected	3	3	11	11	26.7±0.2	26.5±0.2	57±22	0.20±0.02	26.7	2.7	2.7									
857 Glasenappia	227	48	8.20757	Hanuš et al. (2013b)	2	10	30	30	12.0±0.2	14.5±0.2	47±22	0.30±0.02	26.7	2.5	2.3	11.3	0.25	MU						
38	34	8.20756		Hanuš et al. (2013b)	2	10	30	30	11.7±0.2	14.5±0.2	28±27	0.31±0.02	26.7	3.0	2.3									
867 Kovacia	200	-44	8.67807	Hanuš et al. (2013b)	1	2	7	7	25.0±0.8	24.1±0.4	23±17	0.07±0.03	27.3	1.3	3.4	11.3	0.13					Hygiea		
38	-50	8.67807		Hanuš et al. (2013b)	1	2	7	7	24.1±1.1	24.1±0.4	12±12	0.08±0.03	16.1	1.7	3.4									
873 Mechthild	51	-61	11.0064	Hanuš et al. (2016b)	2	4	8	8	31.3±0.6	34.5±0.1	67±32	0.05±0.03	55.4	2.2	2.6	11.2	0.14	PC						
249	-51	11.0064		Hanuš et al. (2016b)	2	4	8	8	32.4±0.4	34.5±0.1	17±17	0.05±0.03	55.4	1.6	2.6									
874 Rotraut	201	-41	14.3007	Hanuš et al. (2013b)	1.5	15	11	11	52.1±0.8	58.3±0.2	52±7	0.07±0.03	55.4	2.7	3.3	9.9	0.14							
2	-36	14.3007		Hanuš et al. (2013b)	1.5	15	11	11	51.2±0.6	58.3±0.2	45±10	0.07±0.03	26.7	2.2	3.3									
890 Waltraut	30	69	12.58309	Hanuš et al. (2018)	3	5	8	8	28.9±1.0	28.4±0.2	80±20	0.13±0.02	55.4	1.8	3.1	10.4	0.20	CTGU:						
122	72	12.58309		Pole rejected	3	5	8	8	29.4±1.2	28.4±0.2	100±20	0.12±0.04	55.4	4.0	3.1									
900 Rosalinde	276	70	16.6868	Hanuš et al. (2013b)	1.5	4	13	13	20.5±0.7	19.6±0.1	7±7	0.10±0.02	3.9	3.2	2.8	11.5	0.19							
90	39	16.6868		Hanuš et al. (2013b)	1.5	4	13	13	20.4±0.6	19.6±0.1	7±6	0.10±0.02	12.6	1.7	2.8									
915 Cosette	350	56	4.46974	Hanuš et al. (2011)	1.5		17	17	12.3±0.2	11.7±0.1	37±37	0.24±0.02	3.9	1.7	2.5	11.6	0.34					Flora		

Table A.3: continued.

Asteroid	λ [deg]	β [deg]	P [h]	Reference	QF	N_1	N_{W3}	N_{W4}	D [km]	D_{WISE} [km]	Γ [SI]	p_V	$\bar{\theta}$	χ^2_{red}	r_{hel} [au]	H [mag]	G	T1	T2	Family
1704 Wachmann	118	-60	13.19179	This work	1.5	1	16	17	20.5±1.1	19.5±0.1	35±35	0.24±0.03	55.4	5.8	2.6					
	267	41	3.31391	Hanuš et al. (2013b)	1		14	14	6.6±0.1	6.6±0.1	120±40	0.24±0.04	26.7	1.2	2.0	12.9	0.30			
	90	40	3.31391	Hanuš et al. (2013b)	1		14	14	6.6±0.1	6.6±0.1	100±40	0.23±0.02	27.3	1.5	2.0					
1723 Klemola	252	-35	6.25610	Hanuš et al. (2018)	3	12	23	19	31.8±0.7	33.4±0.2	37±12	0.15±0.02	48.4	2.7	3.0	10.0	0.26	S		
	80	-58	6.25610	Hanuš et al. (2018)	3	12	23	19	31.4±0.5	33.4±0.2	32±7	0.15±0.02	26.7	2.2	3.0					
1738 Oosterhoff	13	-68	4.44896	Revised	1		9	9	7.9±0.1	7.9±0.1	77±32	0.27±0.05	26.7	1.2	2.2	12.4	0.24		S	Flora
	176	-64	4.44896	Revised	1		9	9	8.0±0.2	7.9±0.1	55±15	0.26±0.07	48.4	1.9	2.2					
1742 Schaifers	198	57	8.53270	Hanuš et al. (2011)	1.5	4	12	12	15.1±0.5	16.7±0.1	85±15	0.24±0.04	26.7	2.4	3.1	11.1	0.18			Koronis
	46	55	8.53271	Hanuš et al. (2011)	1.5	4	12	12	15.5±0.3	16.7±0.1	97±12	0.23±0.06	48.4	2.2	3.1					
1789 Dobrovolsky	318	30	4.81110	Hanuš et al. (2016b)	1.5	7	7	7	8.7±0.1	7.9±0.1	13±7	0.29±0.04	0.0	1.7	2.2	12.2	0.23			
	137	34	4.81110	Hanuš et al. (2016b)	1.5	7	7	7	8.6±0.2	7.9±0.1	16±4	0.28±0.04	0.0	2.7	2.2					
1820 Lohmann	263	64	14.0449	Hanuš et al. (2016b)	2		5	10	6.0±0.1	5.3±0.1	115±15	0.25±0.04	27.3	0.5	2.5	13.1	0.16			
	69	54	14.0449	Hanuš et al. (2016b)	2		5	10	6.1±0.3	5.3±0.1	120±20	0.23±0.04	26.7	0.5	2.5					
1837 Osita	305	-65	3.81880	Revised	1.5	10	9	9	7.2±0.2	7.5±0.1	110±20	0.24±0.02	38.8	1.0	2.0	12.8	0.21			
	126	-63	3.81880	Revised	1.5	10	9	9	6.6±0.2	7.5±0.1	112±17	0.26±0.03	55.4	1.0	2.0					
1902 Shaposhnikov	326	37	20.9959	Hanuš et al. (2016b)	3	6	8	7	77.6±1.4	83.4±1.7	0±0	0.05±0.02	27.3	6.5	4.8	9.2	0.20	X		
	144	78	20.9958	Hanuš et al. (2016b)	3	6	8	7	79.7±2.9	83.4±1.7	0±0	0.04±0.02	26.7	5.9	4.8					
1930 Lucifer	32	17	13.05361	Hanuš et al. (2011)	2	16	13	13	31.6±1.2	34.4±0.2	80±30	0.07±0.02	55.4	3.2	3.3	10.9	0.25		Cgh	
	211	-19	13.05360	Hanuš et al. (2011)	2	16	13	13	29.0±0.6	34.4±0.2	50±15	0.08±0.02	55.4	3.6	3.3					
1987 Kaplan	352	-52	9.45950	Revised	2		9	9	13.0±0.2	13.0±0.2	35±10	0.24±0.02	27.3	0.8	2.9	11.5	0.26			Phocaea
2617 Jiangxi	239	75	11.77295	Hanuš et al. (2013b)	1	8	8	14	52.2±1.7	49.1±0.3	6±6	0.04±0.03	38.8	5.8	2.7	10.4	0.17			
	-1	55	11.77298	Hanuš et al. (2013b)	1	8	8	14	50.7±2.3	49.1±0.3	0±0	0.04±0.03	26.7	3.8	2.7					
2659 Millis	-49	-49	6.12464	Hanuš et al. (2016b)	1.5	2	6	7	27.2±0.6	27.7±0.3	35±19	0.05±0.03	38.8	1.4	3.5	11.5	0.12		B	
	288	-48	6.12464	Hanuš et al. (2016b)	1.5	2	6	7	27.1±0.6	27.7±0.3	37±12	0.05±0.03	38.8	1.4	3.5					
3428 Roberts	78	56	3.27835	Hanuš et al. (2016b)	1		13	13	17.1±0.2	17.2±0.1	62±17	0.09±0.03	3.9	0.7	3.1	11.9	0.16			
	232	60	3.27835	Hanuš et al. (2016b)	1		13	13	17.3±0.6	17.2±0.1	70±10	0.09±0.03	12.6	0.9	3.1					
3544 Borodino	293	-59	5.43460	Hanuš et al. (2016b)	1		17	11	8.3±0.2	8.5±0.1	62±27	0.25±0.02	16.1	4.8	2.3	12.3	0.19			
	156	-57	5.43460	Hanuš et al. (2016b)	1		17	11	8.3±0.2	8.5±0.1	60±20	0.26±0.04	26.7	4.2	2.3					
3678 Mongmanwai	125	-65	4.18297	Hanuš et al. (2011)	1.5	8	8	8	8.5±0.3	8.0±0.1	72±17	0.18±0.07	16.1	1.2	2.9	12.6	0.18		S	
4077 Asuka	57	45	7.92310	Hanuš et al. (2018)	2		12	12	19.0±0.2	19.5±0.2	11±1	0.19±0.03	0.0	4.2	3.3	10.9	0.11			
	266	44	7.92310	Hanuš et al. (2018)	2		12	12	19.4±0.4	19.5±0.2	9±3	0.19±0.03	0.0	2.6	3.3					
4265 Kani	105	60	5.72755	Hanuš et al. (2016b)	1.5	7	6	6	14.3±0.3	14.2±0.2	6±6	0.05±0.02	38.8	1.6	2.9	12.9	0.21		C	
	310	54	5.72755	Hanuš et al. (2016b)	1.5	7	6	6	13.8±0.6	14.2±0.2	1±1	0.05±0.02	3.9	3.3	2.9					
4606 Saheki	40	68	4.97347	Revised	2		8	8	6.5±0.3	6.7±0.1	10±10	0.25±0.04	16.1	1.9	2.4	12.9	0.20			Nysa/Polan
	222	65	4.97347	Revised	2		8	8	7.1±0.3	6.7±0.1	8±8	0.21±0.04	12.6	1.4	2.4					
4800 Veveri	274	-40	6.21570	Hanuš et al. (2018)	1.5		8	7	13.2±0.4	14.1±0.1	37±27	0.17±0.03	12.0	2.4	2.7	11.7	0.12			
	94	-65	6.21570	Hanuš et al. (2018)	1.5		8	7	13.3±0.4	14.1±0.1	40±10	0.17±0.03	38.8	2.3	2.7					
5489 Oberkochen	195	-41	5.62439	Hanuš et al. (2016b)	1.5	3	12	12	14.8±0.4	13.1±0.1	18±12	0.17±0.02	12.0	1.3	2.9	11.6	0.24			
	13	-66	5.62440	Hanuš et al. (2016b)	1.5	3	12	12	14.1±0.2	13.1±0.1	17±17	0.19±0.03	3.9	0.8	2.9					
6136 Gryphon	310	62	16.4684	Hanuš et al. (2018)	2		10	8	15.4±0.2	15.6±0.3	37±12	0.16±0.02	26.7	1.0	3.0	11.6	0.20			
	87	52	16.4684	Hanuš et al. (2018)	2		10	8	15.3±0.5	15.6±0.3	40±15	0.16±0.02	16.1	0.9	3.0					
6635 Zuber	262	-77	5.53564	This work	2		12	12	3.6±0.1	3.9±0.1	85±15	0.28±0.05	55.4	1.0	2.1	14.0	0.21			
	286	-34	5.53564	This work	2		12	12	3.6±0.1	3.9±0.1	19±16	0.33±0.06	16.1	1.4	2.1					
8359 1989 WD	121	-68	2.89103	Hanuš et al. (2013b)	1.5	11	11	11	8.1±0.4	8.2±0.1	57±12	0.10±0.02	38.8	0.9	2.5	13.2	0.20			Vesta
	274	-68	2.89103	Hanuš et al. (2013b)	1.5	11	11	11	8.1±0.3	8.2±0.1	115±35	0.12±0.03	12.6	1.0	2.5					
19848 Yeungchuchiu	66	-70	3.45104	Hanuš et al. (2013b)	1		11	11	10.6±0.7	12.7±0.1	18±12	0.20±0.08	0.0	3.7	2.8	12.1	0.09			Eos
	190	-67	3.45104	Hanuš et al. (2013b)	1		11	11	11.4±0.9	12.7±0.1	18±17	0.17±0.08	12.0	1.4	2.8					

Table A.4: Lightcurve observations used for model revisions and new determinations. We provide the number of dense lightcurves N_{lc} and individual sparse-in-time measurements N_{sp} . The sparse data were obtained by two astrometric surveys – U.S. Naval observatory in Flagstaff (USNO, IAU code 689) and Catalina Sky Survey (CSS, IAU code 703, Larson et al. 2003) or comes from the Lowell database.

Asteroid	Date	N_{lc}	N_{sp}	Reference/Observatory
155 Scylla	1998 07 – 2009 01		110	USNO-Flagstaff
	1999 10 – 2010 05		108	CSS
	2008 11 – 2008 12	4		Owings (2009)
	2008 11 – 2008 12	7		Pilcher and Jardine (2009)
	2014 02 – 2014 02	2		Stephens (2014b)
430 Hybris	1998 11 – 2009 03		105	USNO-Flagstaff
	2005 06 – 2010 06		54	CSS
749 Malzovia	1998 08 – 2008 10		121	USNO-Flagstaff
	2005 10 – 2010 05		136	CSS
	2014 04 – 2014 06	5		Oey (2016)
789 Lena	1998 06 – 2007 07		135	USNO-Flagstaff
	1999 10 – 2010 06		96	CSS
802 Epyaxa	1998 09 – 2003 05		92	USNO-Flagstaff
	2003 03 – 2009 05		50	CSS
	2008 11 – 2009 02	21		Dykhuis et al. (2016)
	2009 01 – 2014 11	4		Warner (2009, 2012)
	2014 11 – 2014 11	2		Stephens (2014a)
998 Bodea	1998 03 – 2007 11		79	USNO-Flagstaff
	2003 05 – 2009 03		70	CSS
1013 Tombecka	1986 04 03	1		Weidenschilling et al. (1990)
	1998 12 – 2009 07		160	USNO-Flagstaff
	2006 10 – 2010 10		87	CSS
1017 Jacqueline	1998 09 – 2009 06		144	USNO-Flagstaff
	1999 11 – 2005 03		140	CSS
1127 Mimi	1998 06 – 2008 02		125	USNO-Flagstaff
	2000 02 – 2010 07		140	CSS
1276 Uccia	1998 07 – 2008 05		114	USNO-Flagstaff
	2006 01 – 2010 11		45	CSS
1545 Thernoë	1999 05 – 2008 05		70	USNO-Flagstaff
	2003 03 – 2010 11		50	CSS
1701 Okavango	1994 10 – 2012 02		380	LOWELL
	2004 07 22	1		Higgins (2005)
1738 Oosterhoff	1998 09 – 2004 06		109	USNO-Flagstaff
	1999 11 – 2010 05		105	CSS
1837 Osita	2006 01 – 2006 03	4		Hanuš et al. (2013b)
	1998 09 – 2012 03		337	Lowell
1987 Kaplan	1999 02 – 2012 01		283	Lowell
	2000 10 – 2000 10	8		Warner (2011, 2012)
4606 Saheki	2004 06 – 2009 06		123	CSS
	2009 01 – 2009 01	2		Hanuš et al. (2013a)
	2009 01 – 2009 03	4		Brinsfield (2009)
6635 Zuber	2005 10 – 2009 03		107	CSS
	2010 06 – 2015 05	13		Warner (2010, 2014, 2015)

Appendix B. Figures

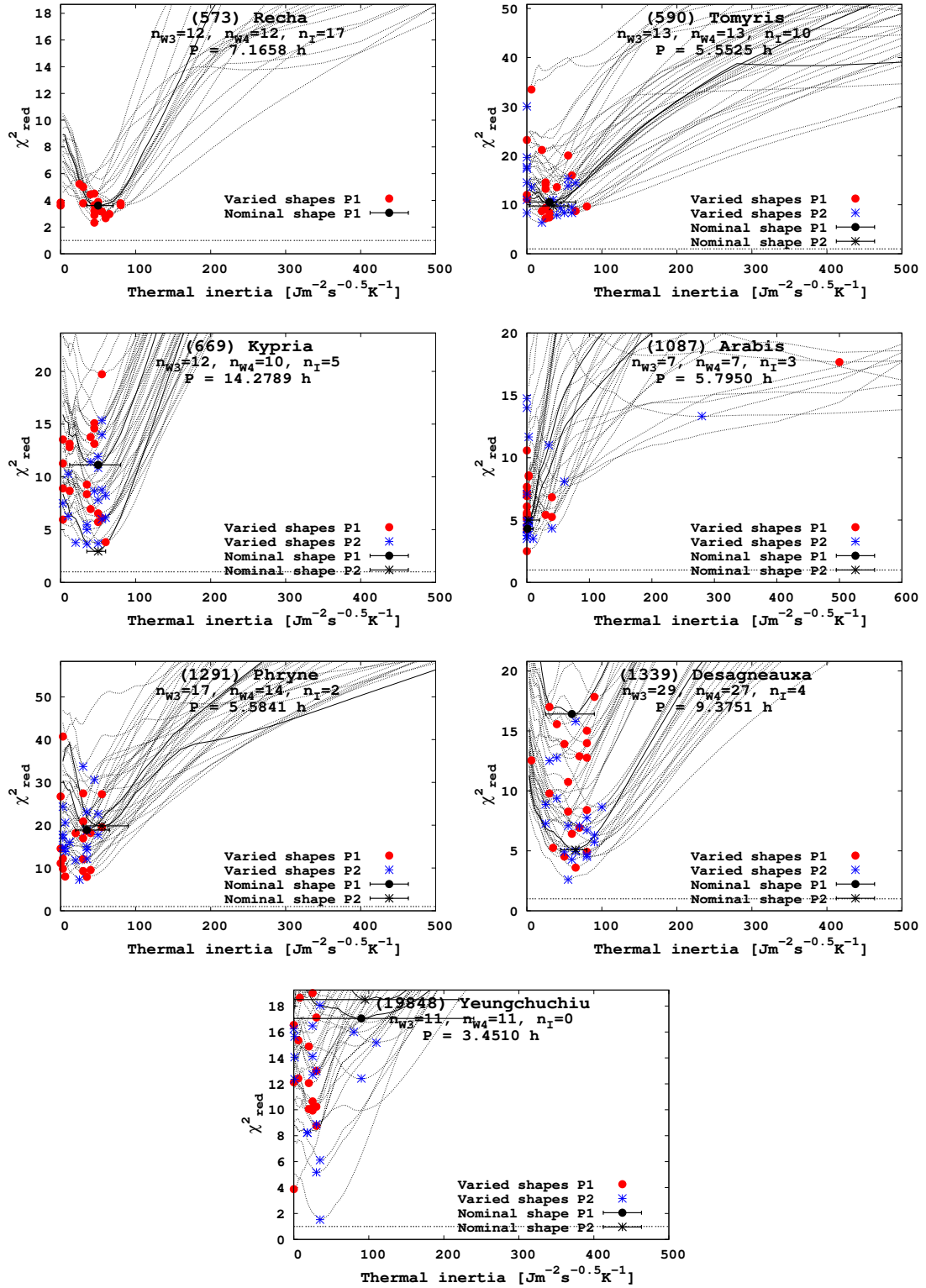


Figure B.9: VS-TPM fits in the thermal inertia parameter space for asteroids from Eos collisional family. Each plot also contains the number of thermal infrared measurements in WISE W3 and W4 filters and in all four IRAS filters, and the rotation period.

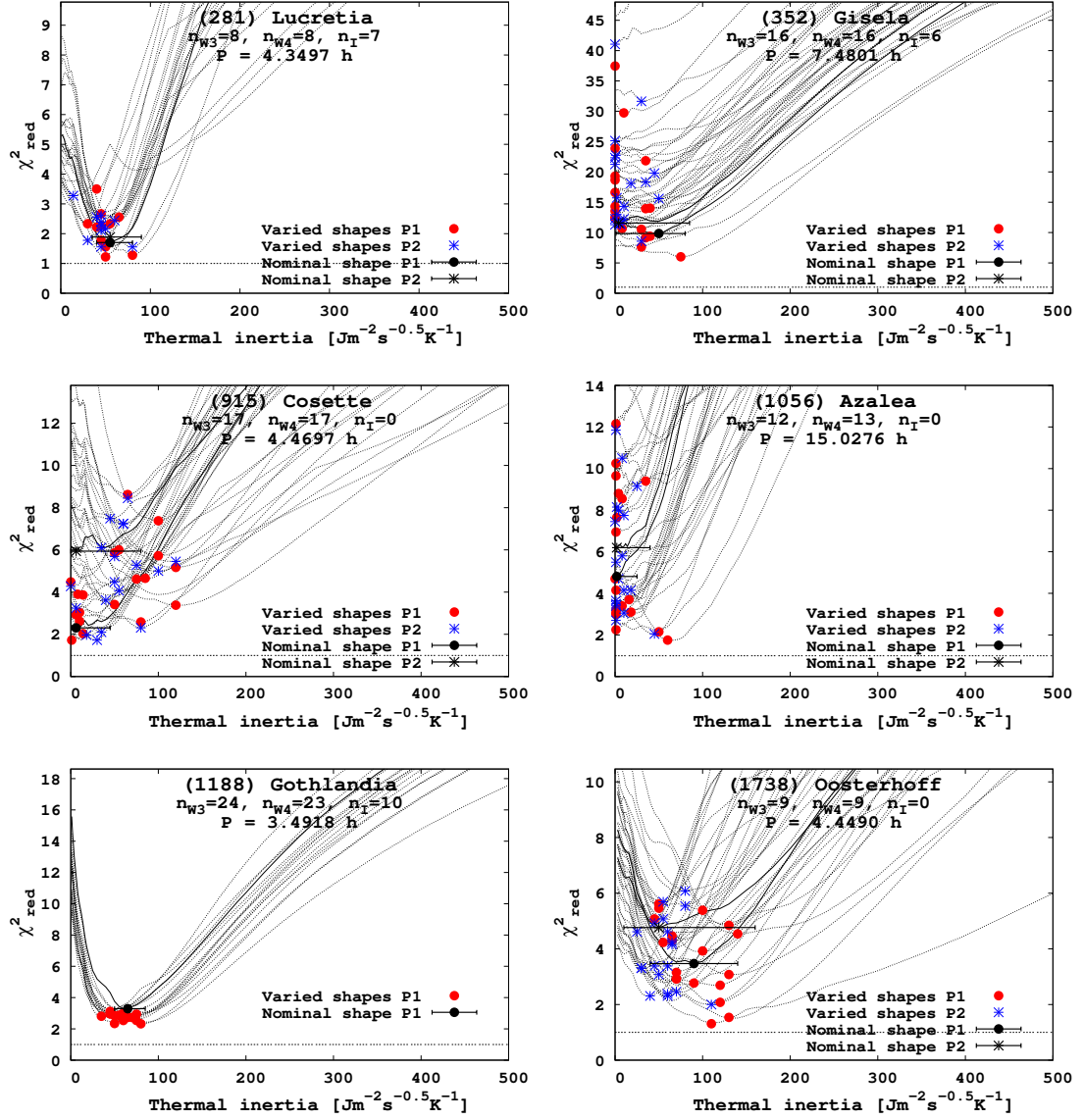


Figure B.10: VS-TPM fits in the thermal inertia parameter space for asteroids from Flora collisional family. Each plot also contains the number of thermal infrared measurements in WISE W3 and W4 filters and in all four IRAS filters, and the rotation period.

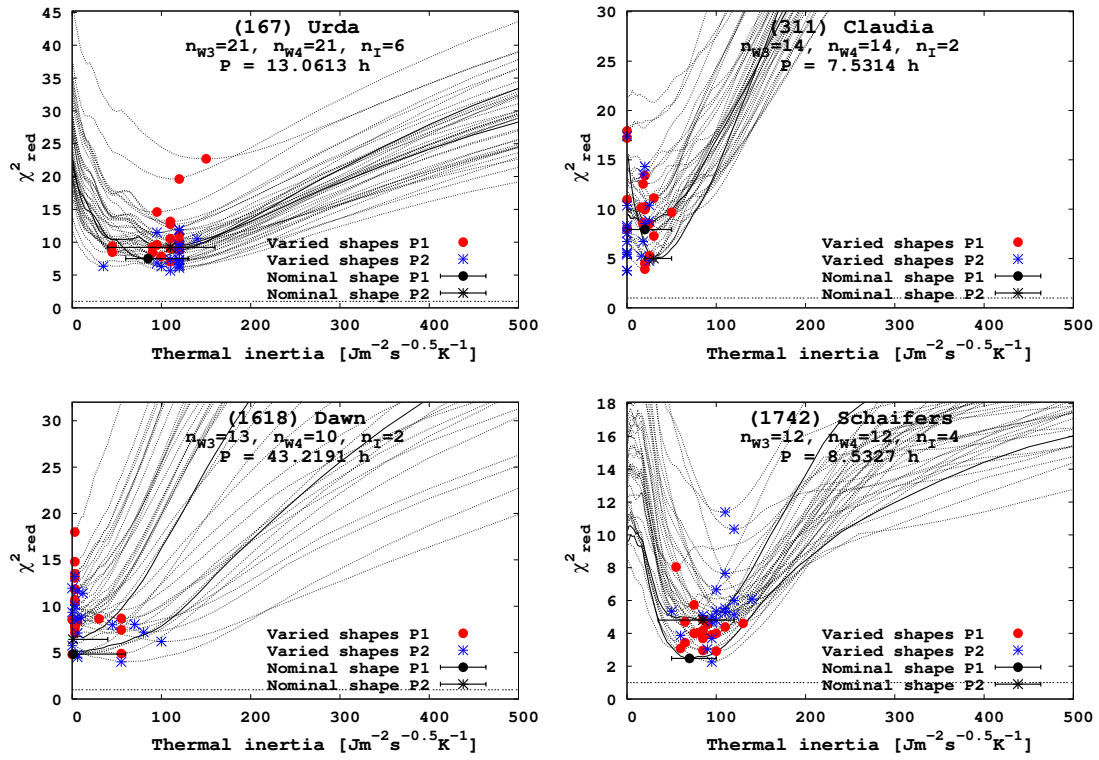


Figure B.11: VS-TPM fits in the thermal inertia parameter space for asteroids from Koronis collisional family. Each plot also contains the number of thermal infrared measurements in WISE W3 and W4 filters and in all four IRAS filters, and the rotation period.

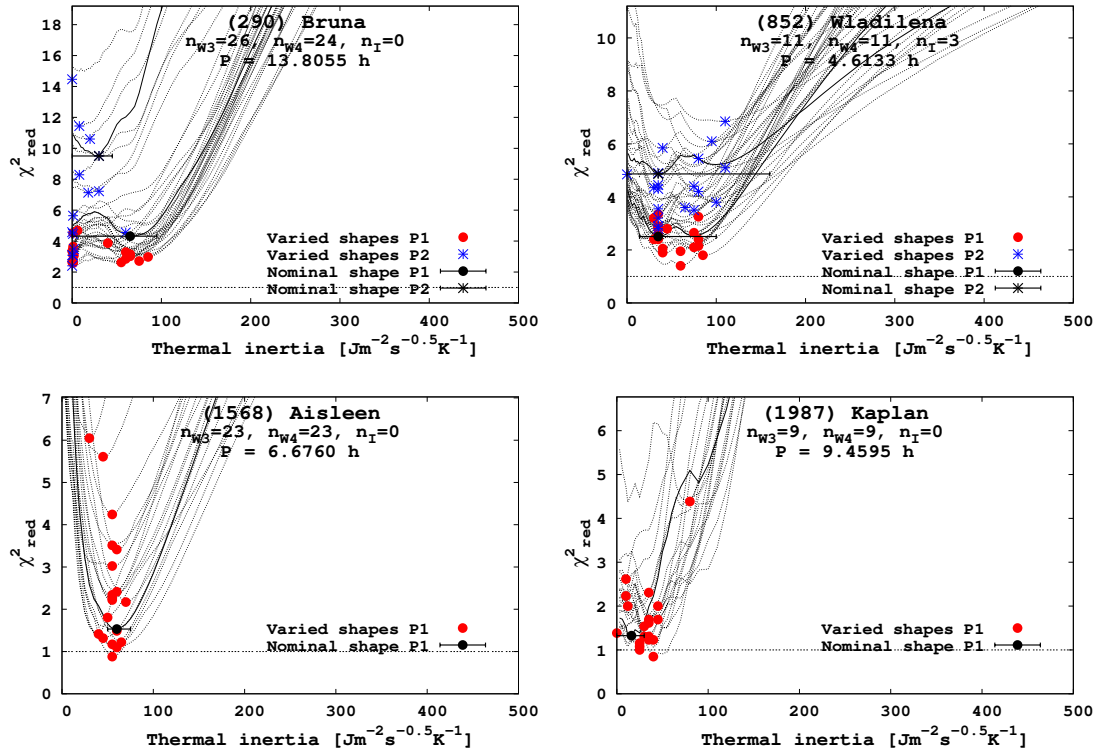


Figure B.12: VS-TPM fits in the thermal inertia parameter space for asteroids from Phocaea collisional family. Each plot also contains the number of thermal infrared measurements in WISE W3 and W4 filters and in all four IRAS filters, and the rotation period.

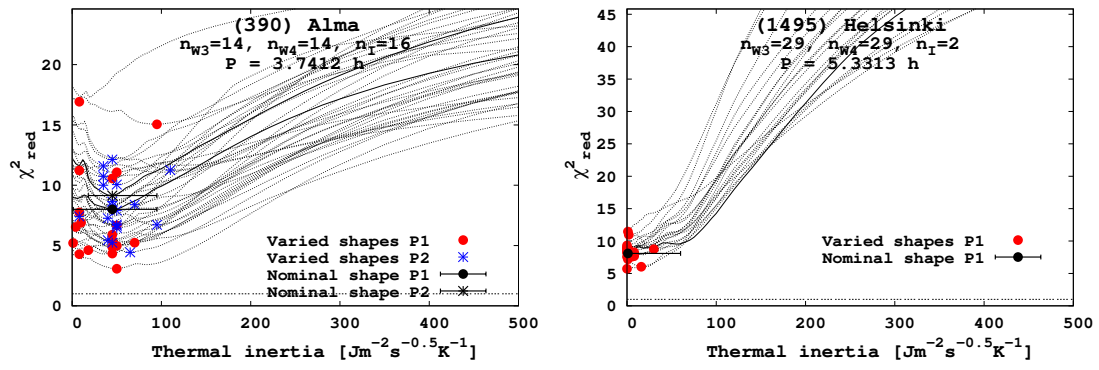


Figure B.13: VS-TPM fits in the thermal inertia parameter space for asteroids from Eunomia collisional family. Each plot also contains the number of thermal infrared measurements in WISE W3 and W4 filters and in all four IRAS filters, and the rotation period.

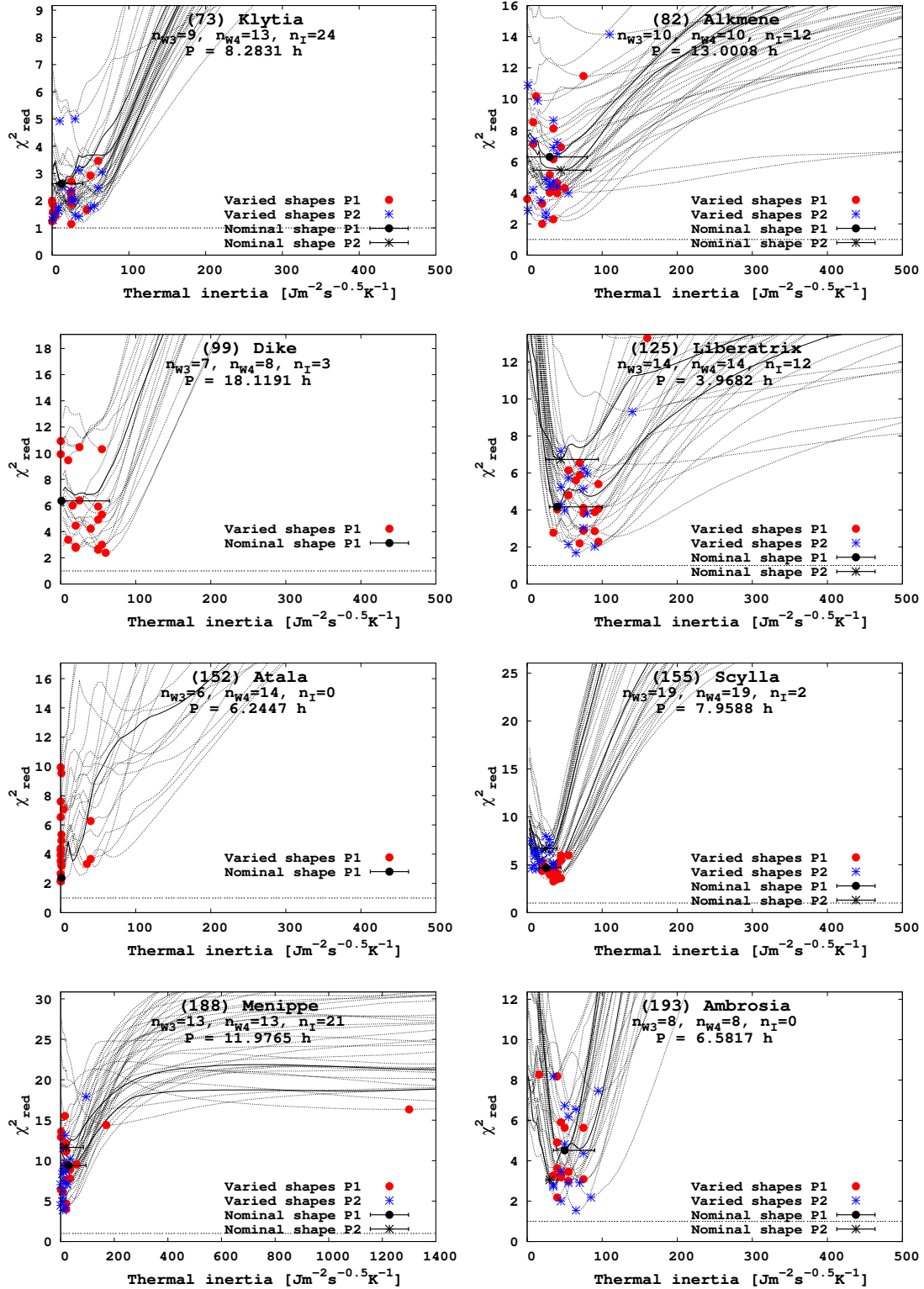


Figure B.14: VS-TPM fits in the thermal inertia parameter space for eight asteroids. Each plot also contains the number of thermal infrared measurements in WISE W3 and W4 filters and in all four IRAS filters, and the rotation period.

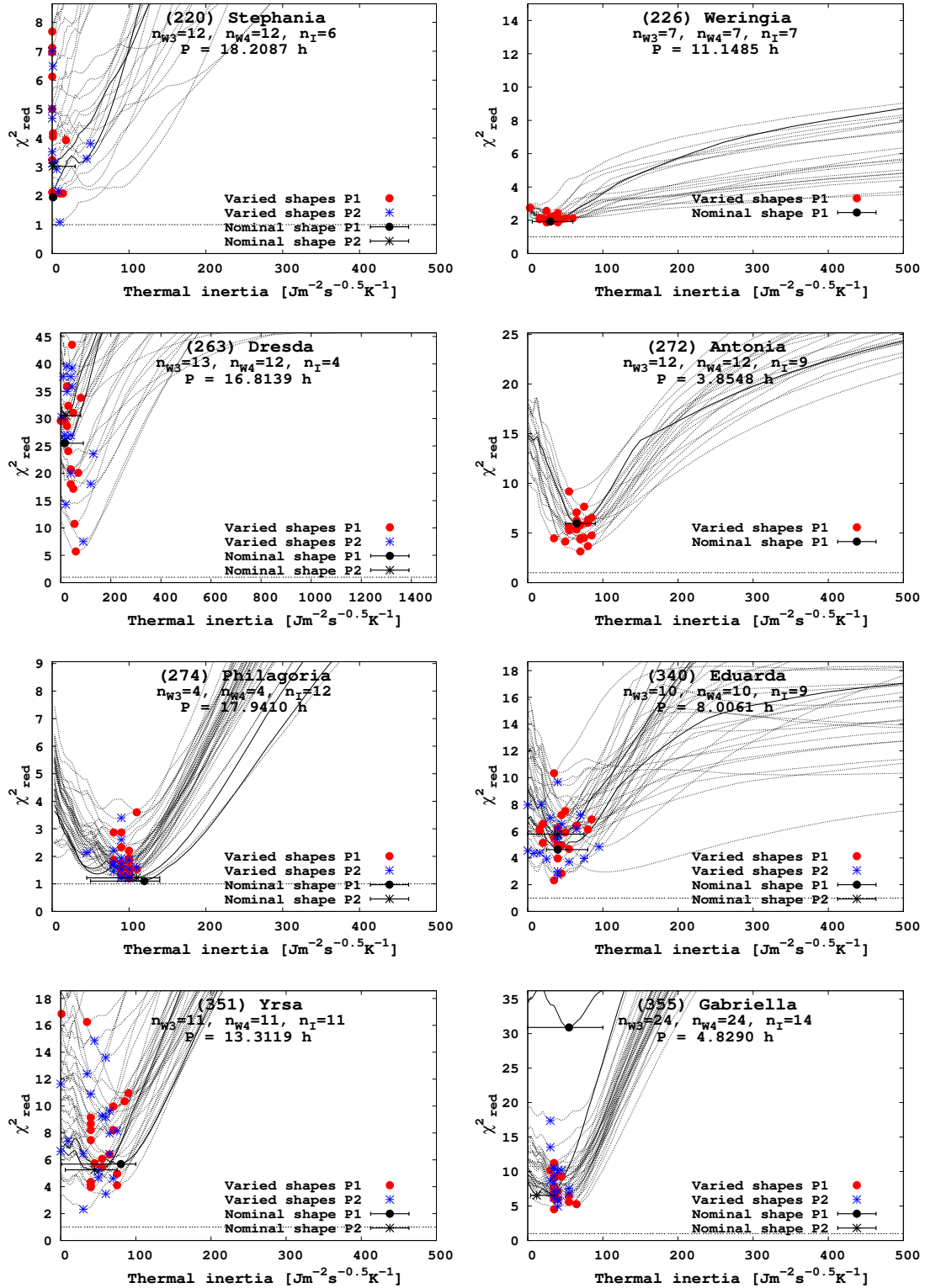


Figure B.15: VS-TPM fits in the thermal inertia parameter space for eight asteroids. Each plot also contains the number of thermal infrared measurements in WISE W3 and W4 filters and in all four IRAS filters, and the rotation period.

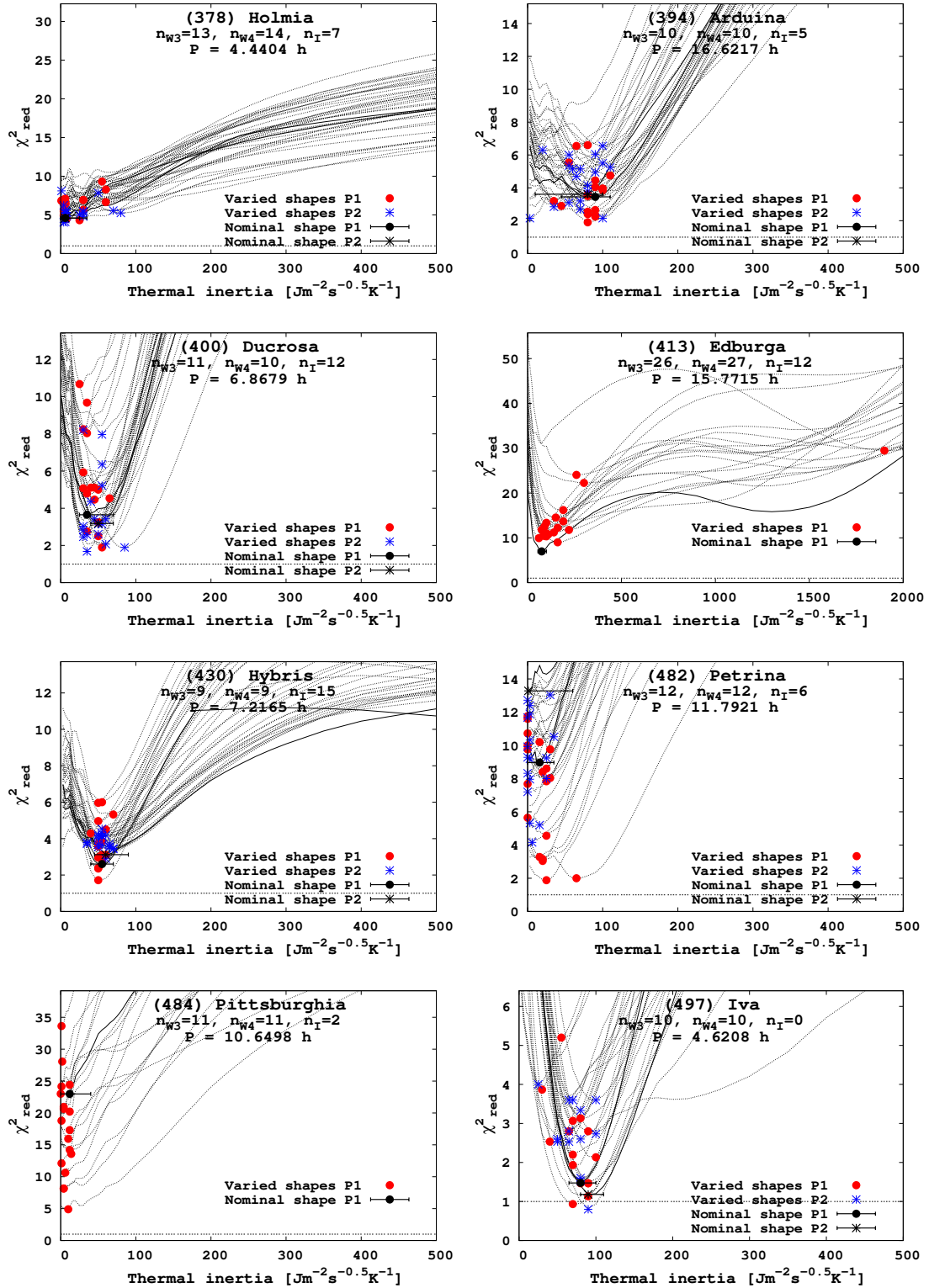


Figure B.16: VS-TPM fits in the thermal inertia parameter space for eight asteroids. Each plot also contains the number of thermal infrared measurements in WISE W3 and W4 filters and in all four IRAS filters, and the rotation period.

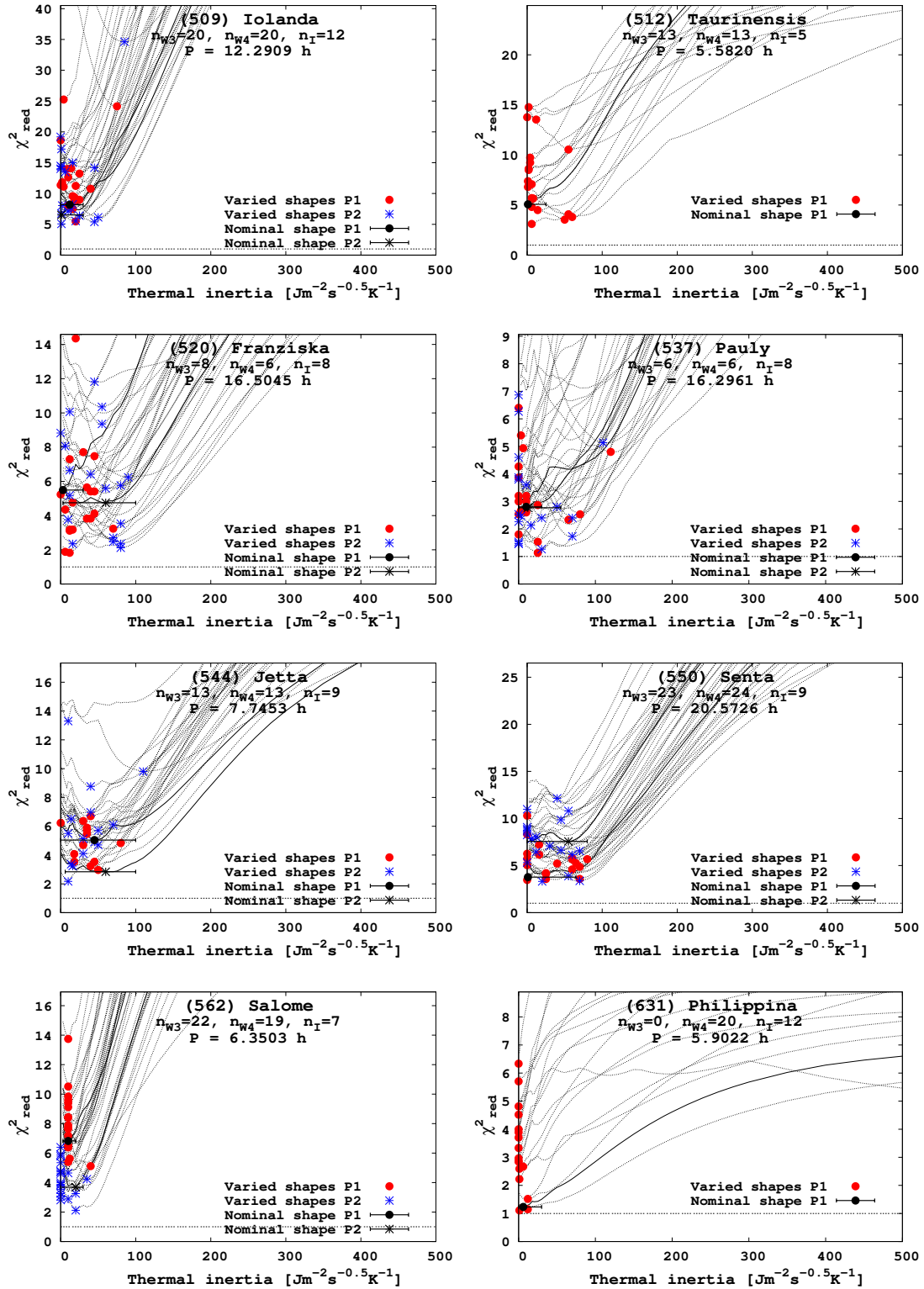


Figure B.17: VS-TPM fits in the thermal inertia parameter space for eight asteroids. Each plot also contains the number of thermal infrared measurements in WISE W3 and W4 filters and in all four IRAS filters, and the rotation period.

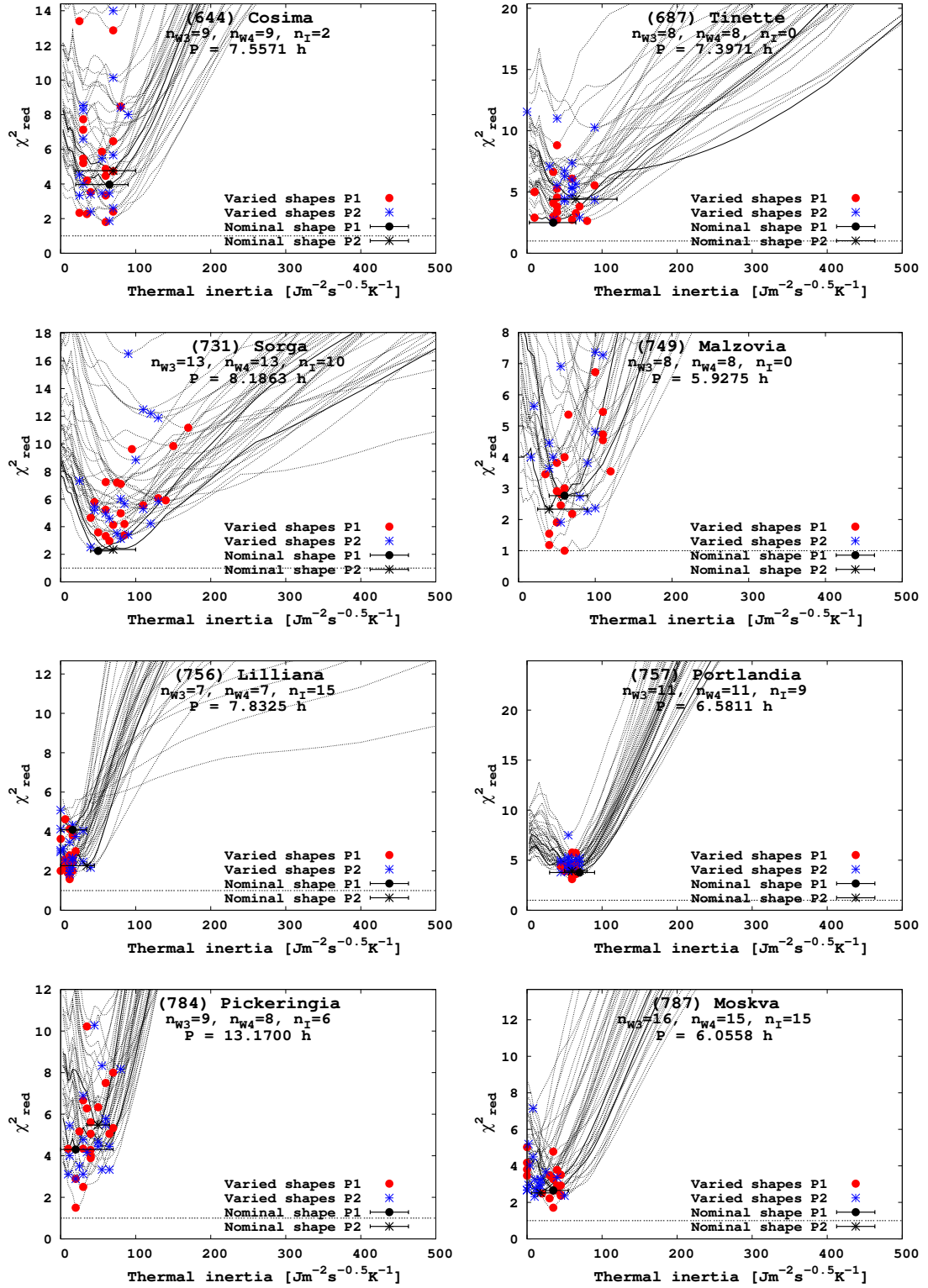


Figure B.18: VS-TPM fits in the thermal inertia parameter space for eight asteroids. Each plot also contains the number of thermal infrared measurements in WISE W3 and W4 filters and in all four IRAS filters, and the rotation period.

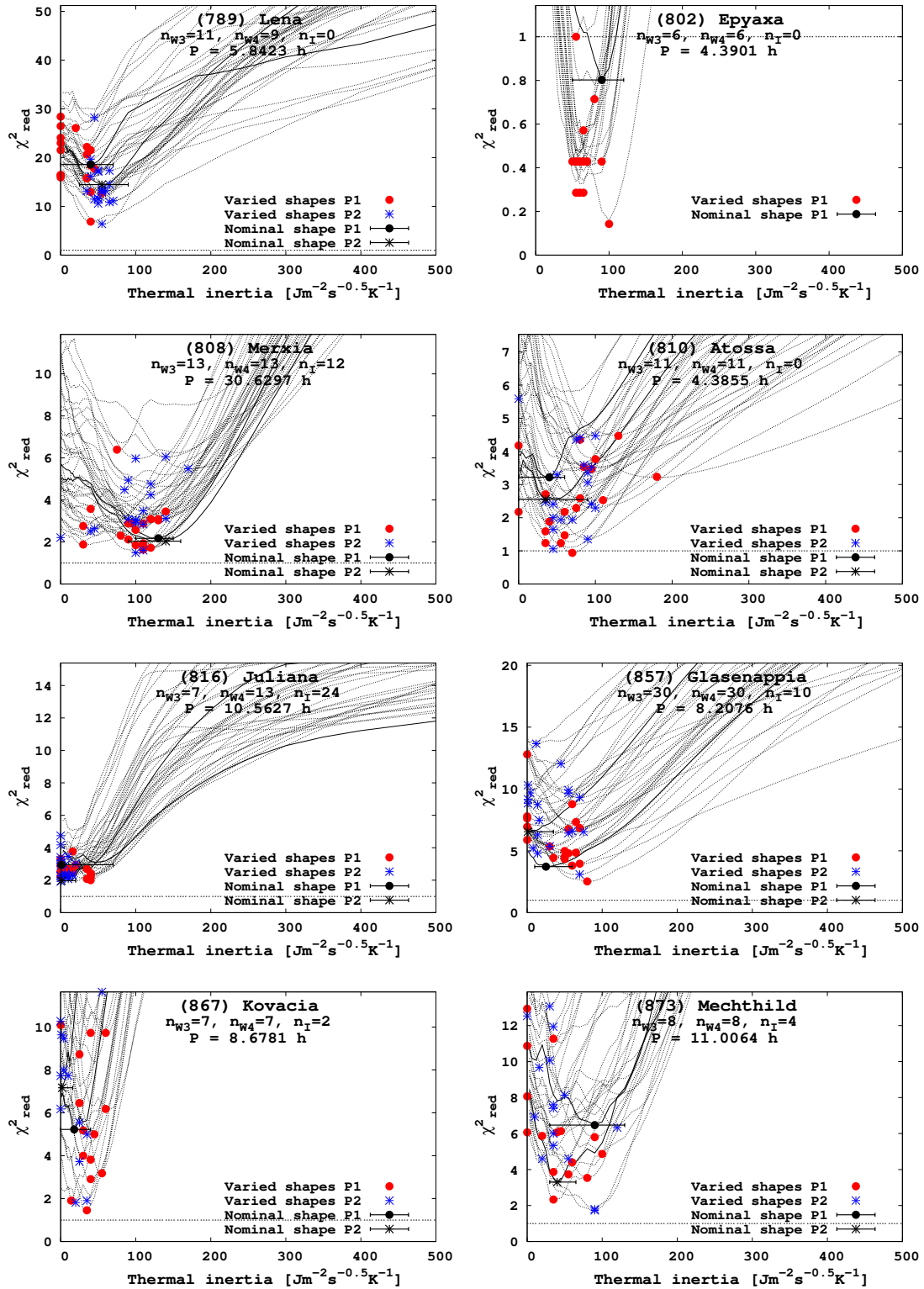


Figure B.19: VS-TPM fits in the thermal inertia parameter space for eight asteroids. Each plot also contains the number of thermal infrared measurements in WISE W3 and W4 filters and in all four IRAS filters, and the rotation period.

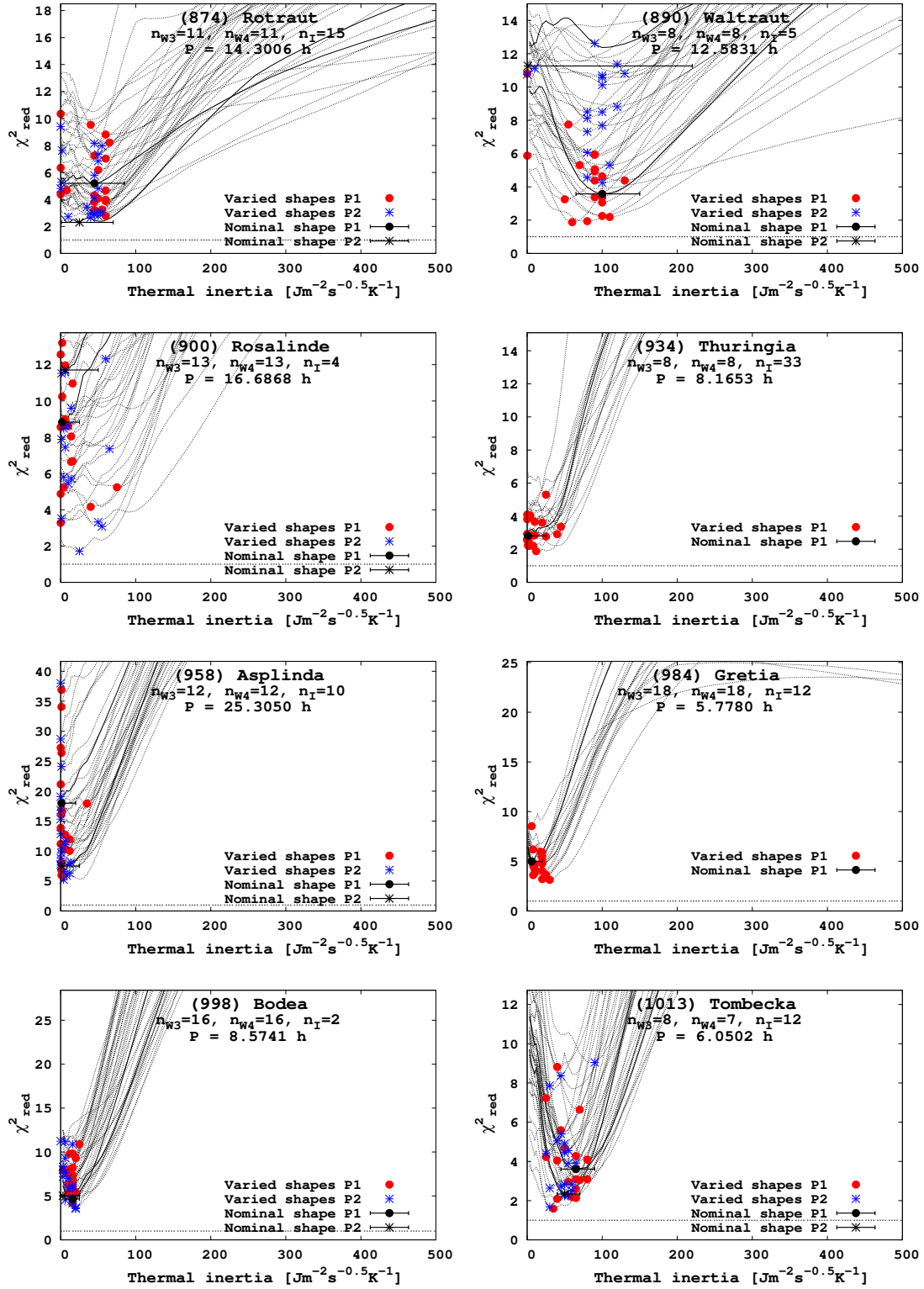


Figure B.20: VS-TPM fits in the thermal inertia parameter space for eight asteroids. Each plot also contains the number of thermal infrared measurements in WISE W3 and W4 filters and in all four IRAS filters, and the rotation period.

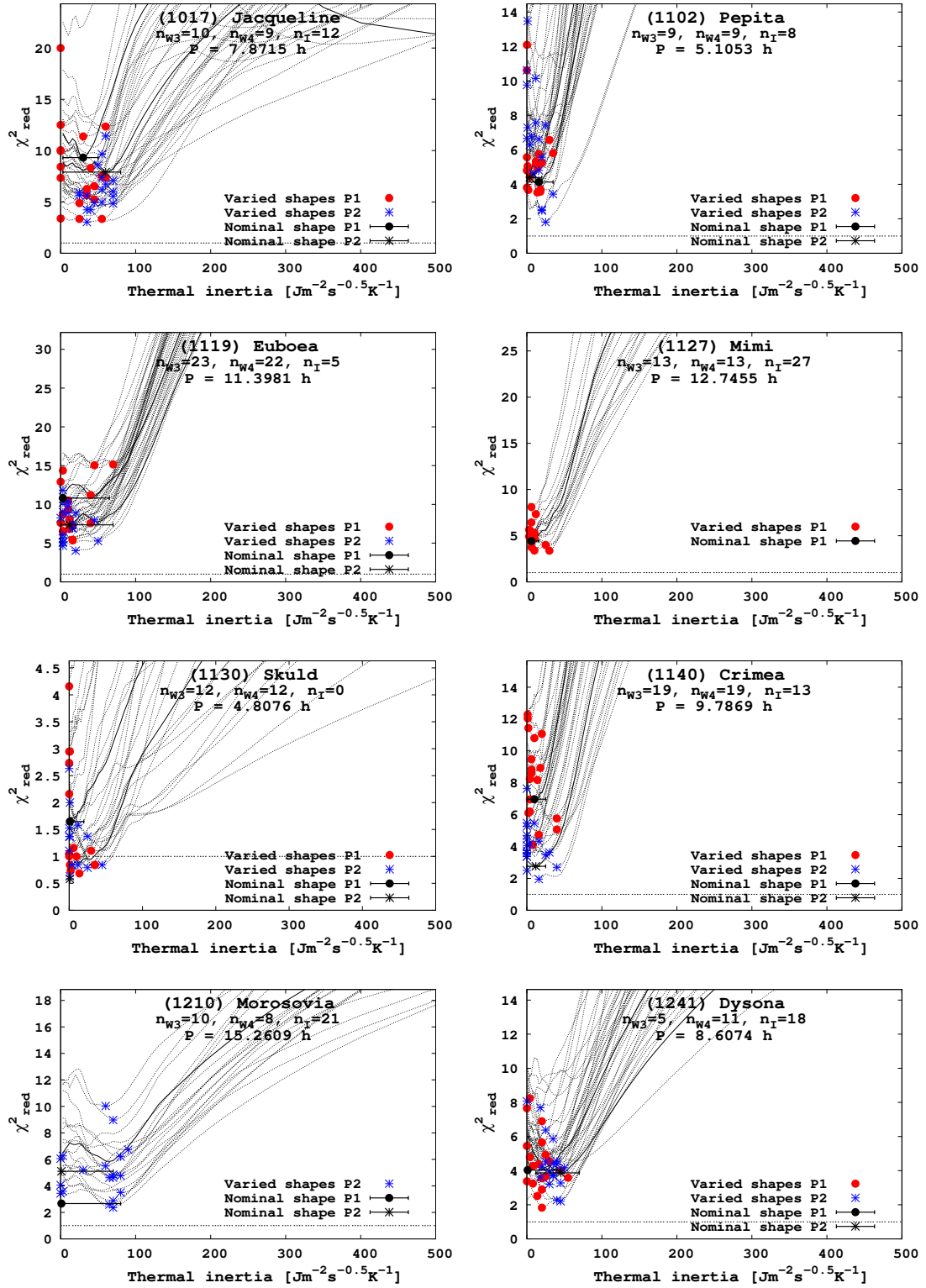


Figure B.21: VS-TPM fits in the thermal inertia parameter space for eight asteroids. Each plot also contains the number of thermal infrared measurements in WISE W3 and W4 filters and in all four IRAS filters, and the rotation period.

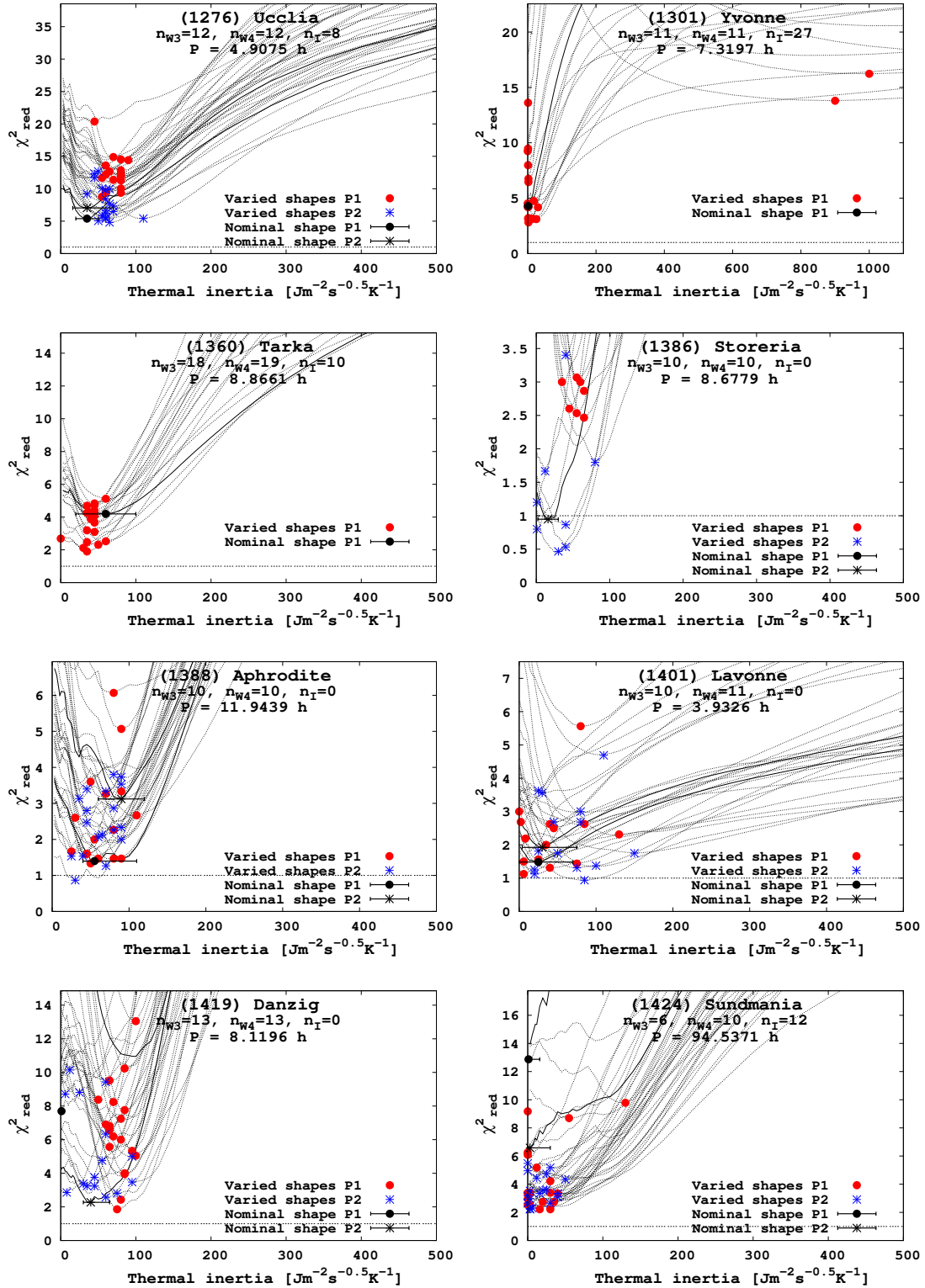


Figure B.22: VS-TPM fits in the thermal inertia parameter space for eight asteroids. Each plot also contains the number of thermal infrared measurements in WISE W3 and W4 filters and in all four IRAS filters, and the rotation period.

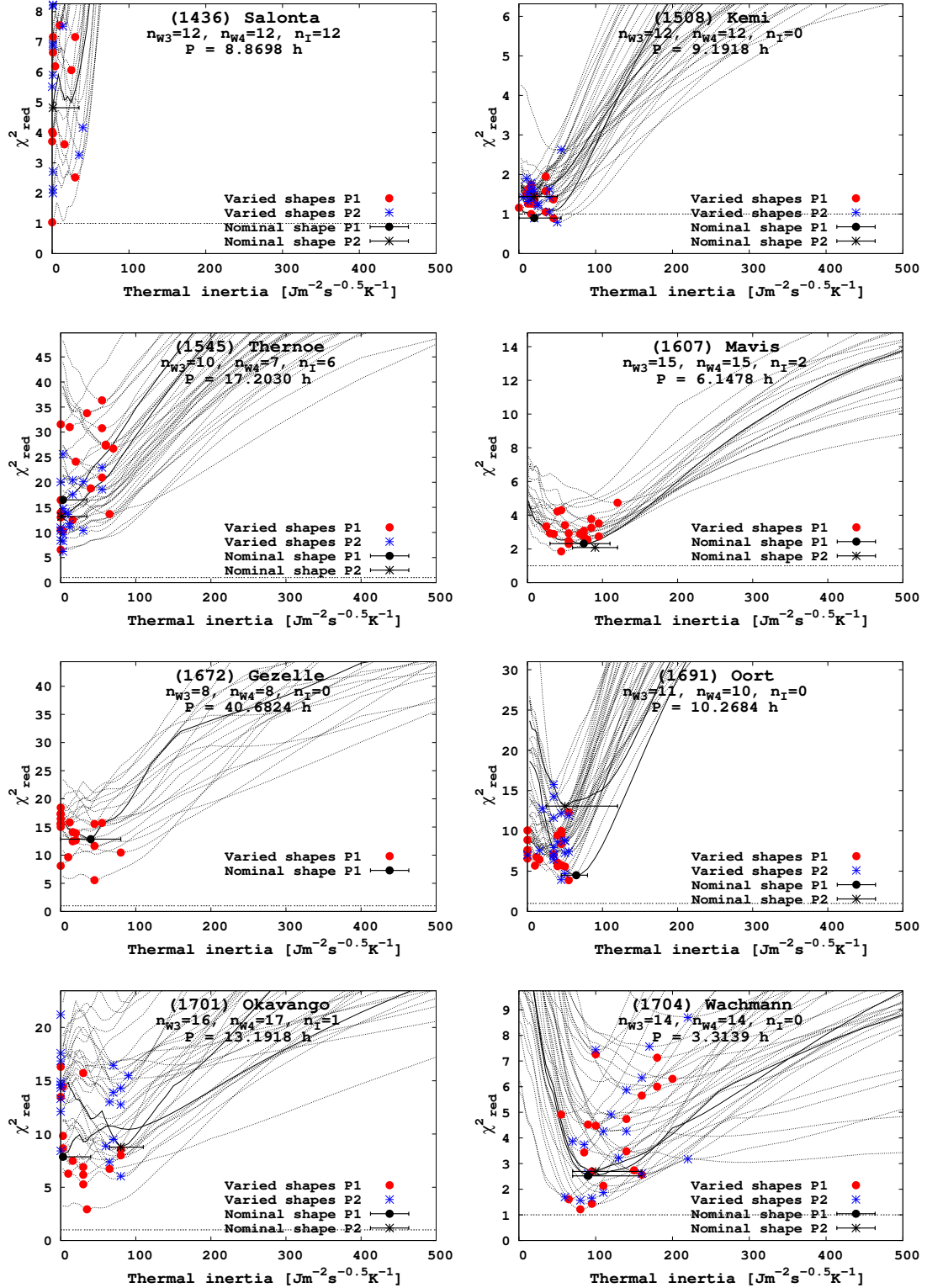


Figure B.23: VS-TPM fits in the thermal inertia parameter space for eight asteroids. Each plot also contains the number of thermal infrared measurements in WISE W3 and W4 filters and in all four IRAS filters, and the rotation period.

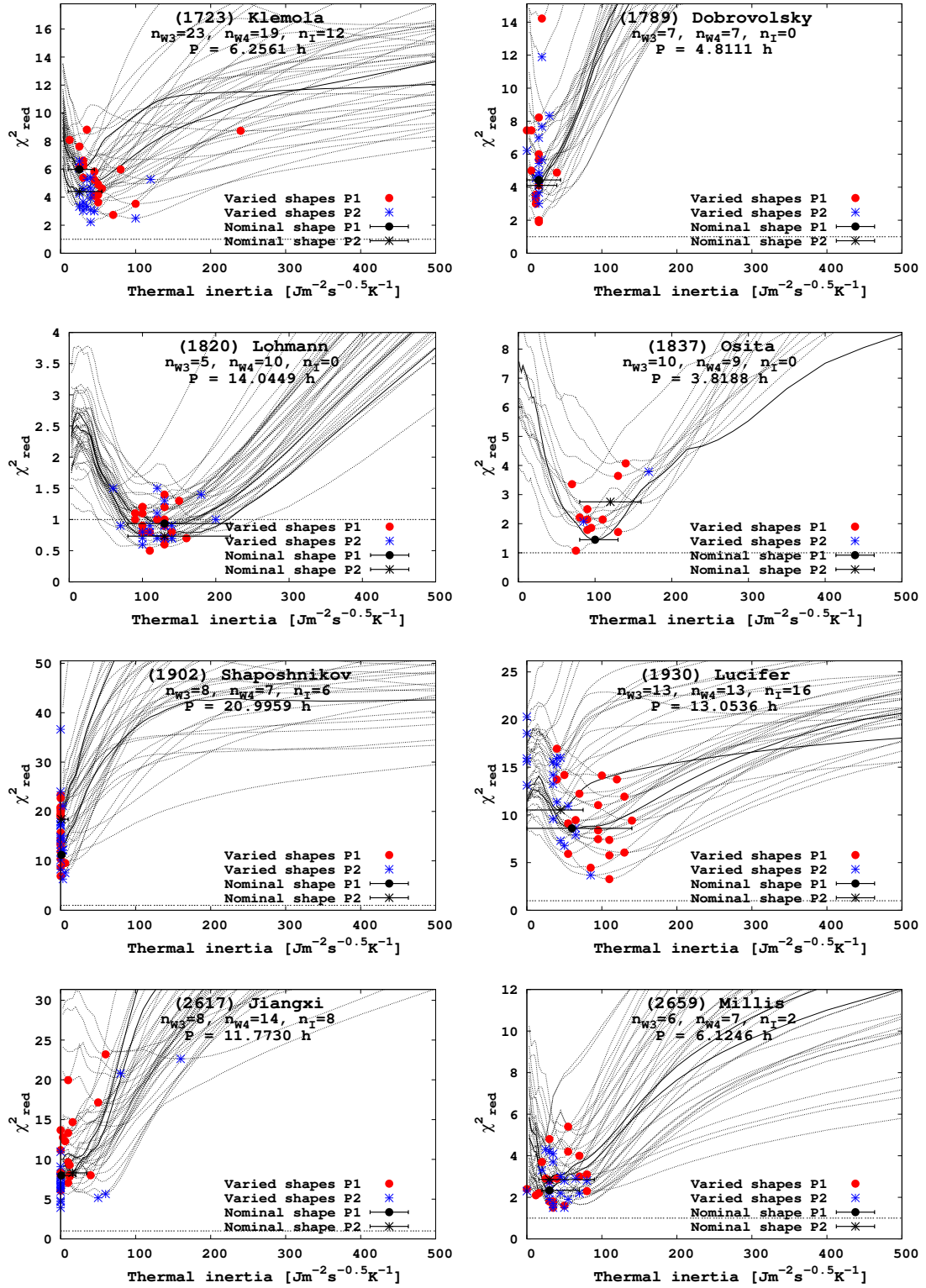


Figure B.24: VS-TPM fits in the thermal inertia parameter space for eight asteroids. Each plot also contains the number of thermal infrared measurements in WISE W3 and W4 filters and in all four IRAS filters, and the rotation period.

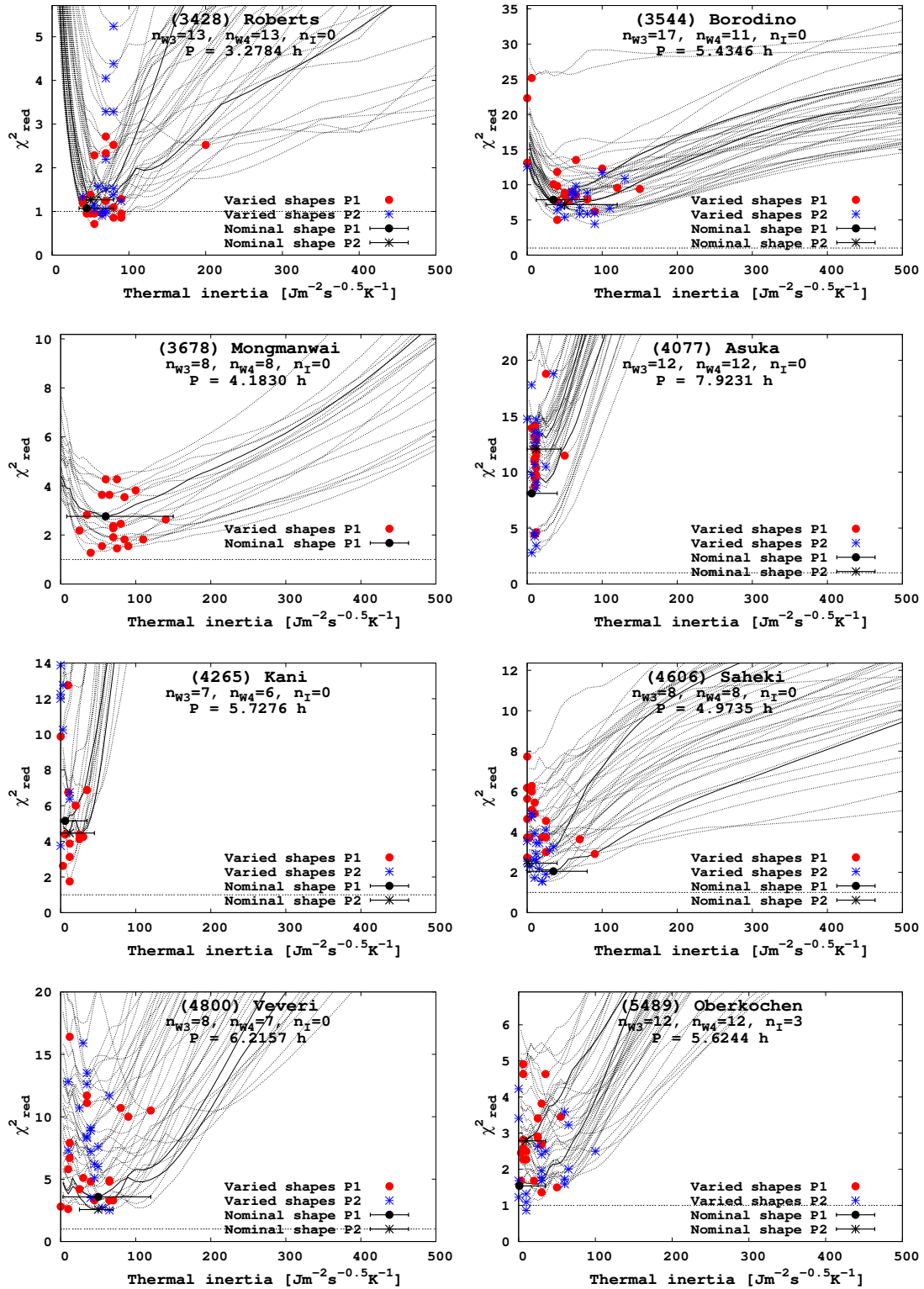


Figure B.25: VS-TPM fits in the thermal inertia parameter space for eight asteroids. Each plot also contains the number of thermal infrared measurements in WISE W3 and W4 filters and in all four IRAS filters, and the rotation period.

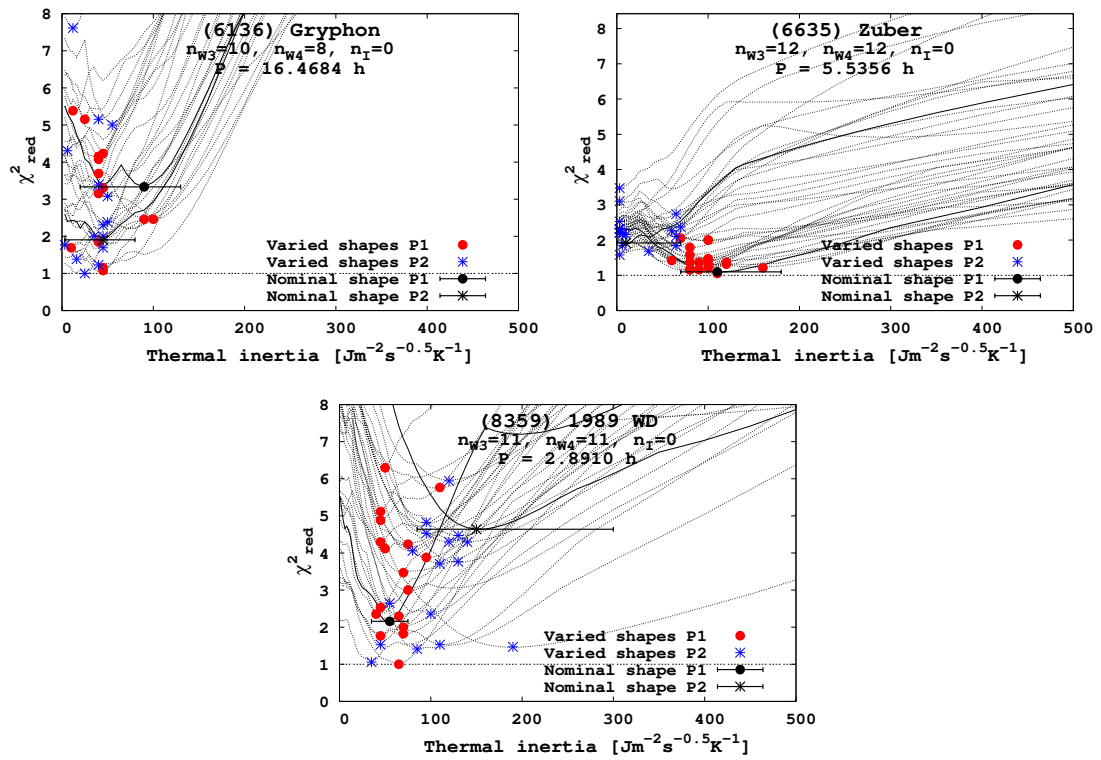


Figure B.26: VS-TPM fits in the thermal inertia parameter space for eight asteroids. Each plot also contains the number of thermal infrared measurements in WISE W3 and W4 filters and in all four IRAS filters, and the rotation period.